Title

Assumed Strain Finite Element Formulations and Stabilization Techniques

Author

Sivapuram, Raghavendra

Publication Date

2020

UNIVERSITY OF CALIFORNIA SAN DIEGO

Assumed Strain Finite Element Formulations and Stabilization Techniques

A dissertation submitted in partial satisfaction of the
requirements for the degree
Doctor of Philosophy

in

Structural Engineering (with a specialization in Computational Science)

by

Raghavendra Sivapuram

Committee in charge:

Professor Petr Krysl, Chair
Professor Jiun-Shyan Chen
Professor Veronica Eliasson
Professor Philip Gill
Professor Hyonny Kim

2020

The dissertation of Raghavendra Sivapuram is approved, and it is acceptable in quality and form for publication on microfilm and electronically:

Chair

University of California San Diego

2020

DEDICATION

I would like to dedicate this thesis to all my teachers without whose contributions I would not have been what I am today.

EPIGRAPH

If you only do what you can do,
you can never do what you can't do.
— Master Shifu, KP:1

We are star dust, and a cosmic fluke.
— Fact

Happiness is not a life goal,
but is a necessary state of mind.
— Learning

TABLE OF CONTENTS

LIST OF FIGURES

LIST OF TABLES

ACKNOWLEDGEMENTS

The 4.5 years of my Ph.D. life have been my formative years, both behaviorally and intellectually. There are a few people who greatly helped me thrive along the way. This section has been the toughest to write, since I am out of words to thank some wonderful people. I feel immensely fortunate for being continuously backed by parents, friends and mentors.

I would be forever indebted to Prof. Krysl without whom this thesis would not have been possible. I am extremely grateful to Prof. Krysl for letting me join his research group in March, 2017. Besides gaining a great deal of subject knowledge, I have learnt a lot of research ethics and the need for open-sourcing in research from Prof. Krysl. I also thank him for being flexible during my Ph.D. in allowing me to pursue internships, and the support during the toughest times. I have got several opportunities for journal manuscript reviewing during my Ph.D., and the values learnt from Prof. Krysl helped me in successful peer review. In short, he has been a great inspiration, and deserves significant credit in all my successes.

Thank you to the committee members for their very useful suggestions and comments on my work. I also thank my qualifying committee members, Prof. A. Kim, Prof. Bazilevs and Prof. Sarkar. I have been a teaching assistant for around 800-900 students during my graduate school. I thank the students for being nice to me, and I wish them every success in their lives. I thank Prof. Krysl, Prof. Asaro, Dr. Mirkhosravi and the Structural Engineering Department for offering me teaching assistantships. I thank Prof. A. Kim for offering me an admission to UC San Diego in 2015.

I faced the toughest problems in my life so far during this journey. I would not have made it through them without the help of my friends. In particular, I express my sincerest gratitude to Mukesh, Parth, Nadim and Harsha for helping me get through tough times. The hard times taught me a great deal about what matters the most. I thank Srivastav for his very helpful suggestions on Leetcoding and his motivation during job hunting. I will cherish the wonderful moments spent with my undergraduate and graduate friends. I thank all my officemates for the great discussions.

I would greatly thank my parents for their unconditional love and support, and the values they taught me. They have been my secret source of strength in the worst of times, and I am eternally grateful for them being what they are.

I thank the teachers of all my courses at UC San Diego. I have learnt so much through their course material and projects. I particularly thank Prof. Gill for the wonderful Numerical Optimization sequence which made me very comfortable with optimization-related topics. I also thank Prof. Gautam and Prof. Sharma, my mentors at IIT Guwahati, with who I did my first research in Optimization and Finite Element Analysis.

I thank my colleagues from Structural and Electrical departments for all the fun hangouts. I am very thankful for the help offered by the Structural Engineering staff during graduate school. I thank *Yogurt World* and *Blue Pepper* for keeping me satiated with their tasty food. I will miss the scenic beauty of the UC San Diego campus, especially Revelle and ERC colleges.

Chapter 2 and 3 have many details taken from the manuscript, “Sivapuram R, Krysl P. Improved Recovered Nodal Stress for Mean-Strain Finite Elements. *Finite Elements in Analysis and Design* 2018; **146**:70-83, doi:10.1016/j.finel.2018.04.005”, and the work is done in collaboration with Prof. Petr Krysl. The dissertation author is the primary investigator of the manuscript.

Chapter 4 and 5 have many details taken from the manuscript, “Sivapuram R, Krysl P. On the Energy-Sampling Stabilization of Nodally Integrated Continuum Elements for Dynamic Analyses. *Finite Elements in Analysis and Design* 2019; **167**:103322, doi:10.1016/j.finel.2019.103322.”, and the work is done in collaboration with Prof. Petr Krysl. The dissertation author is the primary investigator of the manuscript.

VITA

2011-15	Bachelor of Technology in Mechanical Engineering, Indian Institute of Technology (IIT) Guwahati, India
2015-16	Master of Science in Structural Engineering, University of California, San Diego
2015-20	Doctor of Philosophy in Structural Engineering with a Specialization in Computational Science, University of California, San Diego

PUBLICATIONS

1. Petr Krysl, Raghavendra Sivapuram, “Rapid Eigenvalue Estimation using Coherent Nodal Clusters”, *International Journal for Numerical Methods in Engineering*, 2019 [Under Review]

2. Raghavendra Sivapuram, Petr Krysl, “On the Energy Sampling Stabilization of Nodally Integrated Continuum Elements for Dynamic Analyses”, *Finite Elements in Analysis and Design*, Volume 167, 103322, December 2019.

3. Raghavendra Sivapuram, Petr Krysl, “Improved Recovered Nodal Stress for Mean-Strain Finite Elements”, *Finite Elements in Analysis and Design*, Volume 146, pg. 70–83, July 2018.

ABSTRACT OF THE DISSERTATION

Assumed Strain Finite Element Formulations and Stabilization Techniques

by

Raghavendra Sivapuram

Doctor of Philosophy in Structural Engineering (with a specialization in Computational Science)

University of California San Diego, 2020

Professor Petr Krysl, Chair

The design of any engineering component requires robust analysis using numerical methods like the Finite Element Method. Of paramount importance is to develop convergent formulations that can achieve accurate estimates for the solution at cheaper computational costs.

We investigate a method for improving the accuracy of the stress predicted from models using the mean-strain finite elements recently proposed by Krysl and collaborators [IJNME 2016, 2017]. In state-of-the-art finite element programs, the stress values at the integration points are commonly post-processed to obtain nodal stresses. The mean stresses are element-wise constant, and hence the nodal values obtained from the mean stresses tend to be less accurate. The proposed method post-processes the uniform stress in each element in combination with a linearly-varying stabilization stress field to compute more accurate nodal stresses. Selected examples are presented to demonstrate improvements achievable with the proposed methodology for hexahedral and quadratic tetrahedral mean-strain finite elements.

The nodally integrated formulations exhibit spuriousness in dynamic analyses (such as in modal analysis). Previously proposed methods involved a heuristic stabilization factor, which may not work for a large range of problems, and a uniform stabilization was used over all the finite elements in the mesh. The method proposed herein makes use of energy-sampling stabilization. The stabilization factor depends on the shape of the element and appears in the definition of the properties of a stabilization material. The stabilization factor is non-uniform over the mesh, and can be computed to alleviate shear locking, which directly depends on the aspect ratios of the finite elements. The nodal stabilization factor is then computed by volumetric averaging of the element-based stabilization factors. Energy-sampling stabilized nodally integrated elements (ESNICE) tetrahedral and hexahedral are proposed. We demonstrate on examples that the proposed procedure effectively removes spurious (unphysical) modes both at lower and at higher ends of the frequency spectrum. The examples shown demonstrate the reliability of energy-sampling in stabilizing the nodally integrated formulations in vibration problems, just sufficient to eliminate spuriousness while imparting minimal excessive stiffness to the structure. We also show by the numerical inf-sup test that the formulation is coercive and locking-free.

Chapter 1

Introduction

In the modern world, the design of any industrial component requires a simulation phase to check if the design sustains the expected conditions the component is going to be placed in, e.g. engine mounts of an automobile, gears in a manufacturing plant, etc. The simulations significantly decrease the design cost by obviating the need for manufacturing all the designs made during the design phase by checking a set of failure and performance criteria. Simulations also aid in rapid designing for the same reason. The design phase can also be automated using optimization algorithms using the aid of simulations.

Finite Element Method (FEM) is the most popular technique for simulating the performance of a structure under various loads. FEM is also used in fluids, electromagnetics and other physics-based applications governed by Partial Differential Equations (PDE). The structural design problems are usually Boundary-Value Problems (BVPs) and Initial Value Problems (IVPs) and governed by PDEs and kinematic relations. FEM involves approximating the domain in question (in this thesis, structural) using a set of known shapes, e.g. triangles, quadrilaterals, tetrahedra, hexahedra, etc. called finite elements, and a set of basis functions, e.g. polynomial, spline, spectral, etc., for local approximation of the degrees of freedom in question (displacement, stress, temperature, etc). The approximating shapes and their vertices together are called the finite element mesh. FEM works by using local approximation of degrees of freedom using the basis functions in each of the finite elements. The more the number of finite elements, the less is the approximation error, called “discretization error” of the boundary of the structure. Also, higher the order of basis functions, called “shape functions”, better is the approximation of the degrees of freedom.

Several meshing algorithms are available to discretize a 3D structure into tetrahedra, hexahedra and other polyhedra. Tetrahedral elements are preferred for discretizing a structure owing to the availability of robust meshing algorithms, and hexahedral elements are preferred for their bigger approximation space. The tetrahedral meshing algorithms are broadly classified into:

1. Advancing Front algorithms [2, 3, 4]
2. Octet Tree algorithms [5, 6, 7]
3. Delaunay-based algorithms [8]

Hexahedral mesh generation is tougher than tetrahedral mesh because hexahedral meshes cannot employ point-insertion method like Delaunay tessellation and also cannot use advancing fronts. The reader is referred to [9] for a list of quadrilateral/hexahedral meshing algorithms. A good survey of meshing algorithms can be found in [10] and in textbooks [11, 12, 13]. The finite element mesh consists of nodes (vertices of the polyhedra) and elements, and is described by the nodal coordinates and the element connectivity.

The degrees of freedom in a structure are approximated locally in each finite element, using the nodal degrees of freedom and their interpolation using the shape functions. Most applications use polynomial shape functions with local support, i.e., they are nonzero in a small region around each node. Many finite element discretizations use an isoparametric interpolation, which means the set of shape functions used to interpolate the nodal degrees of freedom and the nodal coordinates is the same. Higher order elements like quadratic and cubic have nodes on the edges of elements and/or inside the elements.

This thesis deals with structural mechanics problems, linear statics and dynamics. A brief introduction to these problems is given below. The boundary value problem governing linear elastostatics is given by

$$\begin{aligned} \nabla \cdot \boldsymbol{\sigma} + \boldsymbol{b} &= \mathbf{0} \quad \forall\, \boldsymbol{x} \in \Omega \\ \boldsymbol{u} &= \boldsymbol{g} \quad \forall\, \boldsymbol{x} \in \Gamma_g \\ \boldsymbol{\sigma} \cdot \boldsymbol{n} &= \boldsymbol{h} \quad \forall\, \boldsymbol{x} \in \Gamma_{\boldsymbol{h}} \end{aligned} \tag{1.1}$$

where $\boldsymbol{u}$ is the displacement vector at any point in the structure Ω, $\boldsymbol{g}$ is the prescribed displacements on a part of the boundary Γ_g, called the Dirichlet/essential boundary conditions, $\boldsymbol{\sigma}$ is the stress vector, and $\boldsymbol{h}$ is the traction/boundary loads applied normal (along $\boldsymbol{n}$) to $\Gamma_{\boldsymbol{h}}$, called the Neumann/natural boundary conditions, and $\boldsymbol{b}$ is the volumetric load. The stress vector is given by the constitutive relationship,

$$\boldsymbol{\sigma} = \boldsymbol{D} \cdot \boldsymbol{\varepsilon} \tag{1.2}$$

where $\boldsymbol{D}$ is the material properties tensor given by Hooke's law, and ε is the strain vector. We represent the material properties tensor in Voigt notation in this work, i.e. as a square matrix of size 3 × 3 in 2D and 6 × 6 in 3D problems. The strain vector is given by the kinematic constraints,

$$\boldsymbol{\varepsilon} = \nabla_s\, \boldsymbol{u} \tag{1.3}$$

where ∇_s is the symmetric gradient operator. The PDE in Equation 1.1 is second order in space and is valid at each point in the interior of the structure. The BVP in Equation 1.1 is called the *strong form* of the problem. The strong form of the problem is converted to a *weak form* by projecting the residual of the PDE over the entire structure into a function space and equating the projected residual to zero. This leads to what is called the Principle of Virtual Displacements. More details on the weak form derivation can be found in [14]. In this work, we use an alternate to arrive at the weak form using the potential energy functional. The Potential Energy functional for the BVP in Equation 1.1 is given by

$$\begin{aligned} \underset{\boldsymbol{u}}{\text{Minimize}}\ \psi(\boldsymbol{u}) &= \frac{1}{2}\int_{\Omega} \boldsymbol{\varepsilon}^T \boldsymbol{\sigma}\, d\Omega - \int_{\Omega} \boldsymbol{u}^T \boldsymbol{b}\, d\Omega - \int_{\Gamma_{\boldsymbol{h}}} \boldsymbol{u}^T \boldsymbol{h}\, d\Gamma \\ \boldsymbol{u} = \boldsymbol{g} \quad &\forall\, \boldsymbol{x} \in \Gamma_g \end{aligned} \tag{1.4}$$

where ψ is the potential energy functional. The displacements $\boldsymbol{u}$ belong to a function space, e.g. H^1. More information about the function spaces used in FEM can be found in [14]. The potential energy functional can be minimized using the Karush-Kuhn-Tucker (KKT) conditions,

$$\begin{gathered} \frac{1}{2}\int_{\Omega} \delta\boldsymbol{\varepsilon}^T \boldsymbol{D}\boldsymbol{\varepsilon}\, d\Omega - \int_{\Omega} \delta\boldsymbol{u}^T \boldsymbol{b}\, d\Omega - \int_{\Gamma_{\boldsymbol{h}}} \delta\boldsymbol{u}^T \boldsymbol{h}\, d\Gamma = 0 \\ \boldsymbol{u} = \boldsymbol{g},\ \delta\boldsymbol{u} = \boldsymbol{0} \quad \forall\, \boldsymbol{x} \in \Gamma_g \end{gathered} \tag{1.5}$$

where $\delta\boldsymbol{u}$ is the virtual displacements, also called the variation of displacements, and can be chosen from an appropriate function space. Using finite element interpolation and the kinematic constraints, one can obtain a system of equations,

$$\boldsymbol{K}\boldsymbol{u} = \boldsymbol{F} \tag{1.6}$$

where $\boldsymbol{u}$ is the nodal displacement vector, $\boldsymbol{K}$ is the stiffness matrix, and $\boldsymbol{F}$ is the load vector. The stiffness matrix and load vector are computed as

$$\begin{aligned} \boldsymbol{K} &= \sum_{e=1}^{N_{el}} \int_{\Omega_e} \boldsymbol{B}^T \boldsymbol{D}\boldsymbol{B}\, d\Omega \\ \boldsymbol{F} &= \sum_{e=1}^{N_{el}} \int_{\Omega_e} \boldsymbol{N}^T \boldsymbol{b}\, d\Omega + \sum_{i=1}^{N_h} \int_{\Gamma_{\boldsymbol{h}e}} \boldsymbol{N}^T \boldsymbol{h}\, d\Gamma \end{aligned} \tag{1.7}$$

where N_{el} is the number of finite elements, N_h is the number of boundary elements discretizing $\Gamma_{\boldsymbol{h}}$, $\boldsymbol{N}$ is a matrix with shape functions, and $\boldsymbol{B}$ is a matrix containing the shape function gradients, called the strain-displacement matrix. The stiffness matrix is banded and positive definite, with the bandwidth depending on the order of interpolation. The system of equations can be pretty huge in many applications, e.g. civil, automobile, aerospace, etc., and in general, more the degrees of freedom used to approximate the problem, better is the accuracy. Robust and fast solvers are to be used to solve these problems, and this solving of equations is computationally very expensive.

The discretizations using coarse meshes and/or lower order shape functions are relatively faster in computation, but lack the accuracy. One of the objectives of developing new finite element formulations is to achieve coarse mesh accuracy when lower order shape functions are used. In some problems, the discretizations involving coarse meshes and/or lower order shape functions (e.g. linear, quadratic) yield numerical artifacts in displacements, stresses, etc. One way to avoid these artifacts is to use a very fine mesh, which increases the number of unknowns thereby greatly increasing the computational cost. One other way is to use higher order shape functions, which increases the unknowns and also the bandwidth of the stiffness matrix contributing the increase in computational cost. Research in developing novel finite element formulations is thus pivotal in creating artifact-ridden formulations which can give accurate solutions with lesser number of unknowns.

For more details of function spaces, weak forms, shape functions, and finite element discretization errors, the reader is directed to the textbooks [14, 15, 16, 17].

1.1 Locking in Structures with Incompressible and Nearly-Incompressible materials

Numerical problems arise in problems with Poisson's ratio close to 0.5. Consider the 3D materials properties tensor considering isotropy,

$$\boldsymbol{D} = \frac{E}{(1+\nu)(1-2\nu)} \begin{bmatrix} 1-\nu & \nu & \nu & 0 & 0 & 0 \\ \nu & 1-\nu & \nu & 0 & 0 & 0 \\ \nu & \nu & 1-\nu & 0 & 0 & 0 \\ 0 & 0 & 0 & \frac{1-2\nu}{2} & 0 & 0 \\ 0 & 0 & 0 & 0 & \frac{1-2\nu}{2} & 0 \\ 0 & 0 & 0 & 0 & 0 & \frac{1-2\nu}{2} \end{bmatrix}$$

$$= \begin{bmatrix} \lambda+2\mu & \lambda & \lambda & 0 & 0 & 0 \\ \lambda & \lambda+2\mu & \lambda & 0 & 0 & 0 \\ \lambda & \lambda & \lambda+2\mu & 0 & 0 & 0 \\ 0 & 0 & 0 & \mu & 0 & 0 \\ 0 & 0 & 0 & 0 & \mu & 0 \\ 0 & 0 & 0 & 0 & 0 & \mu \end{bmatrix} \tag{1.8}$$

where E and ν are the Young's modulus and Poisson's ratio of the material respectively, λ and μ are called the Lamé's constants, given by

$$\begin{aligned} \lambda &= \frac{E\nu}{(1+\nu)(1-2\nu)} \\ \mu &= \frac{E}{2(1+\nu)} \end{aligned} \tag{1.9}$$

The materials with $\nu = 0.5$ are called incompressible, and ν close to 0.5 are called nearly-incompressible. This thesis only deals with nearly-incompressible problems. We can see from

Equation 1.9 that as $\nu \rightarrow 0.5$, $\lambda \rightarrow \infty$. An incompressible material imposes an additional constraint on the structural problem,

$$\nabla \cdot \boldsymbol{u} = 0 \quad \forall\, \boldsymbol{x} \in \Omega \tag{1.10}$$

at each point in the structure. This constraint is very similar to the continuity constraint in fluid mechanics for incompressible flows. This additional constraint severely restricts the displacements for coarse meshes and lower order shape functions. This locking of displacements is called *volumetric locking*. One way to avoid this is to use a Lagrange-multiplier based formulation [14]. This, however to extra degrees of freedom (pressure) in the formulation. The extent of locking in the formulation can be explained using *constraint counts*.

Constraint count is given by the ratio of displacement degrees of freedom in the problem to the number of constraints applied. The incompressibility constraint is applied, one at each of the integration points. The optimal ratio of degrees of freedom and incompressibility constraints for different finite elements (continuum/plate) is given in Table 1.1. For example, consider a cube discretized using continuum hexahedral finite elements, n elements on each side. These elements use trilinear shape functions and use $2 \times 2 \times 2$ Gaussian quadrature for full (exact) integration of the stiffness matrix. In total, $8n^3$ integration points i.e., $8n^3$ incompressibility constraints are applied because of full integration. The total degrees of freedom is $3(n+1)^3$. Upon refinement, he constraint count gives the ratio

Table 1.1: Optimal Constraint Counts for different formulations

Formulation	Optimal Ratio
3D continuum	3
2D continuum (Plane Strain)	2

$$r = \lim_{n \to \infty} \frac{3(n+1)^3}{8n^3} = \frac{3}{8} \tag{1.11}$$

This implies, the formulation has 8 constraints on an average, for every 3 degrees of freedom, which is overconstrained and results in severe locking. One way to avoid this locking is to use Reduced Integration (RI) which uses $1 \times 1 \times 1$ Gauss quadrature for integration. We can see that it leads to the optimal constraint count ratio (3). Using reduced integration for the entire stiffness matrix is called Uniform Reduced Integration (URI), and leads to singularities in the element stiffness matrices. The singularities lead to spurious zero-energy modes called hourglass modes in the formulation. Since these spurious modes result in zero potential energy, they appear in the displacement solution. Figure 1.1 shows an example of hourglass modes in a 2D continuum problem discretized using quadrilateral mesh and integrated using reduced quadrature. The hourglass modes can be used using many techniques like Selective Reduced Integration (SRI) [14, 18], B-bar methods [14], hourglass stabilization, etc. This thesis uses an assumed strain approach coupled with an "energy-sampling" stabilization procedure to eliminate the spurious modes. A reduced integration rule does not exist for tetrahedral elements since full integration uses just one integration point. This thesis also discusses a nodally integrated assumed-strain formulation (with necessary stabilization) to eliminate locking in triangles/tetrahedra. More formulations which are devoid of volumetric locking can be found in [14, 18].

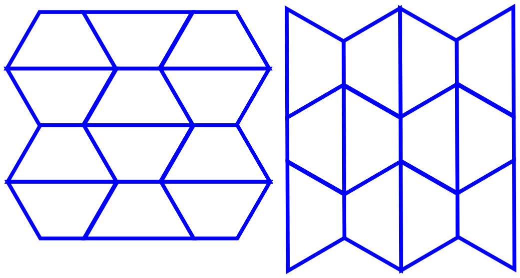

Figure 1.1: Hour glass modes in a 2D Quadrilateral mesh

1.2 Misapproximation of Pure Bending in Linear Elements

Consider the pure bending mode of finite elements. The linear finite elements cannot exactly represent the pure bending mode because pure bending is quadratic. This results in a finite element subjected to pure bending to undergo some shear deformation. This phenomenon leads to overestimation of potential energy, which leads to reduced displacements. This locking behavior is called *shear locking*. A pure bending mode is shown in Figure 1.2 which clearly shows why a linear element cannot reproduce such mode.

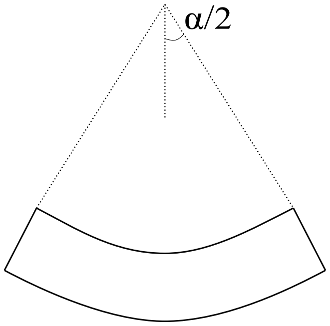

Figure 1.2: Pure bending mode

Using higher order elements can remove shear locking since quadratic shape functions are a part of such elements. The deformation energy due to shear locking decreases with mesh refinement quadratically (by a power of 2 of the element size). A very fine mesh can have negligible shear locking, but is expensive computationally because of the increased number of degrees of freedom. Some other remedies to avoid shear locking uses incompatible modes [14].

Structural elements like plates and shells also have the problem of shear locking, because of the difference in orders of interpolations of the rotations and transverse displacements. Constraint counts can be used to get an estimate of the extent of shear locking. In plates, the optimal constraint count ratio is 1.5.

In this work, we use an aspect-ratio based stabilization to remove the shear stiffness from the added stabilization terms. For a hexahedral beam, the extent of shear locking depends on the aspect ratio of the finite element. The potential energy estimated by a linear quadrilateral element subjected to a pure bending mode [19] is given by

$$\psi = B\left(1+\frac{\mu A L^2}{E h^3}\right) = B\left(1+\frac{L^2}{2(1+\nu)h^2}\right) \tag{1.12}$$

where h is the height of the element, L is the length (span) of the element, A is the area of cross-section, and B is the exact energy of the pure bending mode.

The rest of the thesis is organized as follows. Chapter 2 derives and discusses in detail the mean-strain formulation, and the corresponding stabilization for quadratic tetrahedral and hexahedral elements. Chapter 3 develops an improved stress field consistent with the stabilized mean-strain formulation, and a trend-based extrapolation to obtain a nodal stress field. Several examples are shown to demonstrate an improvement in stress estimation using the trend-based extrapolation as compared to the mean stresses. The new stress field is optimally convergent (unlike the mean stress field), and is noise-free in nearly-incompressible problems (unlike the stress fields generated using fully integrated elements). Chapter 4 presents a detailed derivation of the Nodally Integrated Continuum Elements. All the characteristics of the formulation are presented and the dynamic instability of the formulation is discussed. Chapter 5 discusses the Energy-Sampling stabilization of the nodally integrated formulation for linear tetrahedral and hexahedral elements. Examples show how spuriousness is eliminated from the nodally integrated formulation, and theoretical bounds to guarantee physical free vibration modes are derived. Chapter 6 summarizes and presents the key conclusions of the work. Chapter 8 discusses the possible extensions and potential future work related to this thesis.

Chapter 2

Stabilized Mean-Strain Finite Elements

In Finite Element Analysis (FEA) of complex structures, tetrahedral and hexahedral meshes are preferably used. The tetrahedral meshes are preferred because of the many robust tetrahedral meshing algorithms available, and the hexahedral meshes are preferred for their better interpolative capacity over tetrahedral meshes. The linear elements, both tetrahedral and hexahedral, suffer from volumetric locking when dealing with near-incompressible materials. They also suffer from shear locking because of their inability in representing the bending modes exactly. One can use higher order interpolations to eliminate such defects in the formulations, however, at the expense of huge computational cost. An alternative is to use assumed-strain finite element formulations. As the name suggests, a consistent formulation can be developed for creating an assumed strain field, which would "smoothen" the formulation, i.e., alleviate the locking. Some methods use Selective Reduced Integration of the stiffness matrices and B-bar techniques to avoid volumetric locking ([14, 18]).

The assumed-strain formulations involve reducing the number of sampling points for integration element-wise. The linear tetrahedral elements have only one integration point for full integration, and so, such element-wise assumed strains cannot be computed. The assumed-strains possible for linear tetrahedra will be discussed in the forthcoming chapters. This chapter uses quadratic tetrahedral and hexahedral elements for deriving the assumed strains. The quadratic tetrahedral (T10) elements are devoid of volumetric locking, but suffer from shear locking. The main issues we aim to address are : 1. to eliminate volumetric locking 2. to achieve coarse mesh accuracy 3. stability 4. to avoid shear locking. Reduce Integration can be used to eliminate locking, but it renders the formulation singular, creating hourglass modes. They can be stabilized using additional terms in the stiffness matrix. The stabilization should be designed in such a way that it does not deteriorate the response of the element, but it should provide stability to the element by penalizing the unphysical deformation modes.

In this chapter, we discuss a stabilization technique which uses two quadrature rules : 1. mean-strain quadrature which removes the locking from the formulation, but is singular, and 2. full quadrature which removes singularity from the formulation. To prevent the full quadrature-based term to add locking to the formulation, a different material tensor is used for the stabilization terms. The next section discusses in detail, the formulation, and the design of stabilization material. The formulation is developed such that no user interference is required in choosing any parameters for stabilization. The formulation so developed is locking-free and coarse-mesh accurate as demonstrated in [20, 21].

2.1 Assumed–Strain Formulation

In this section, a brief review of mean-strain finite element formulation for linear elasticity from [22, 23, 24] is presented. We confine our presentation to the parts that are essential for developing the proposed stress field. In this work, we consider both the mean strain hexahedral elements [23] (H8MSGSO) and quadratic tetrahedral elements [24] (QT10MS) for investigating the proposed stress computation procedure. In what follows, we shall use the Voigt vector notation for stresses and strains.

Consider the de Veubeke-Hu-Washizu strain-displacement functional [25],

$$\Pi(\bar{\boldsymbol{\varepsilon}}, \bar{\boldsymbol{\sigma}}, \boldsymbol{u}) = \int_{\Omega} \mathcal{U}(\bar{\boldsymbol{\varepsilon}})\, d\Omega + \int_{\Omega} \bar{\boldsymbol{\sigma}} \cdot (\boldsymbol{\varepsilon} - \bar{\boldsymbol{\varepsilon}})\, d\Omega - \mathcal{W} \tag{2.1}$$

The first term in Equation 2.1 signifies the strain energy in terms of assumed strains. The second term adds a kinematic constraint which penalizes the difference between the strains and the assumed strains, with $\bar{\boldsymbol{\sigma}}$ being the Lagrangian multipliers. Further, Ω signifies the domain, $\mathcal{W}$ is the work done by the external forces, u is the displacement field, $\boldsymbol{\varepsilon}$ and $\bar{\boldsymbol{\varepsilon}}$ are the strains and assumed strains respectively. The strains are obtained from the displacements using

$$\boldsymbol{\varepsilon} = \boldsymbol{B}\boldsymbol{u} \tag{2.2}$$

where $\boldsymbol{B}$ is the strain-displacement operator. The strain-displacement functional can be rewritten by substituting Equation 2.2 in Equation 2.1 as

$$\Pi(\bar{\boldsymbol{\varepsilon}}, \bar{\boldsymbol{\sigma}}, \boldsymbol{u}) = \int_{\Omega} \mathcal{U}(\bar{\boldsymbol{\varepsilon}})\, d\Omega + \int_{\Omega} \bar{\boldsymbol{\sigma}} \cdot (\boldsymbol{B}\boldsymbol{u} - \bar{\boldsymbol{\varepsilon}})\, d\Omega - \mathcal{W} \tag{2.3}$$

We introduce the symmetric positive definite material elasticity tensor D, and the assumed-strain energy density can then be defined as

$$\mathcal{U}(\bar{\boldsymbol{\varepsilon}}) = \frac{1}{2} \bar{\boldsymbol{\varepsilon}}^T \boldsymbol{D} \bar{\boldsymbol{\varepsilon}} \tag{2.4}$$

In what follows, we assume the material properties $\boldsymbol{D}$ to be uniform across each finite element. The weak forms of equilibrium equations are obtained by minimizing the functional Equation 2.1. The strain-displacement functional is minimized when the first variations of Equation 2.1 vanish as

$$\delta\Pi_{\boldsymbol{u}}(\bar{\boldsymbol{\varepsilon}}, \bar{\boldsymbol{\sigma}}, \boldsymbol{u}) = \int_{\Omega} \bar{\boldsymbol{\sigma}}^T \boldsymbol{B} \delta\boldsymbol{u}\, d\Omega - \delta\mathcal{W} = 0 \tag{2.5}$$

$$\delta\Pi_{\bar{\boldsymbol{\varepsilon}}}(\bar{\boldsymbol{\varepsilon}},\bar{\boldsymbol{\sigma}},\boldsymbol{u}) = \int_{\Omega}\Big(\frac{\partial\mathcal{U}(\bar{\boldsymbol{\varepsilon}})}{\partial\bar{\boldsymbol{\varepsilon}}} - \bar{\boldsymbol{\sigma}}\Big)\delta\bar{\boldsymbol{\varepsilon}}\, d\Omega = 0 \tag{2.6}$$

$$\delta\Pi_{\bar{\boldsymbol{\sigma}}}(\bar{\boldsymbol{\varepsilon}},\bar{\boldsymbol{\sigma}},\boldsymbol{u}) = \int_{\Omega}(\boldsymbol{Bu} - \bar{\boldsymbol{\varepsilon}})^T\delta\bar{\boldsymbol{\sigma}}\, d\Omega = 0 \tag{2.7}$$

At this point, we can start constructing the finite element model. We shall assume that Equation 2.6 and Equation 2.7 are satisfied on each finite element e separately, meaning that

$$\delta\Pi_{\bar{\boldsymbol{\sigma}}}(\bar{\boldsymbol{\varepsilon}},\bar{\boldsymbol{\sigma}},\boldsymbol{u}) = \int_{\Omega}(\boldsymbol{Bu} - \bar{\boldsymbol{\varepsilon}})^T\delta\bar{\boldsymbol{\sigma}}\, d\Omega = \sum_{e}\int_{\Omega_e}(\boldsymbol{Bu} - \bar{\boldsymbol{\varepsilon}})^T\delta\bar{\boldsymbol{\sigma}}\, d\Omega = 0 \tag{2.8}$$

is satisfied by setting each term in the summation to zero,

$$\int_{\Omega_e}(\boldsymbol{Bu} - \bar{\boldsymbol{\varepsilon}})^T\delta\bar{\boldsymbol{\sigma}}\, d\Omega = 0 \quad \forall e \in [1, N_{el}] \tag{2.9}$$

where Ω_e is the domain of finite element e (N_{el} is the number of finite elements), and from Equation 2.6, we analogously derive

$$\int_{\Omega_e}\Big(\frac{\partial\mathcal{U}(\bar{\boldsymbol{\varepsilon}})}{\partial\bar{\boldsymbol{\varepsilon}}} - \bar{\boldsymbol{\sigma}}\Big)^T\delta\bar{\boldsymbol{\varepsilon}}\, d\Omega = 0 \quad \forall e \in [1, N_{el}] \tag{2.10}$$

We assume that the strains $\bar{\boldsymbol{\varepsilon}}$ are uniform within each element. Equation 2.10 will then be identically satisfied on each finite element e by taking the uniform element-wise stress as

$$\bar{\boldsymbol{\sigma}} = \frac{\partial\mathcal{U}(\bar{\boldsymbol{\varepsilon}})}{\partial\bar{\boldsymbol{\varepsilon}}} = \boldsymbol{D}\bar{\boldsymbol{\varepsilon}} \tag{2.11}$$

where the second expression results from Equation 2.4. Substituting Equation 2.11 into Equation 2.9 makes it possible to solve for the element-wise assumed strains as

$$\bar{\boldsymbol{\varepsilon}} = V_e^{-1}\int_{\Omega_e}\boldsymbol{\varepsilon}\, d\Omega = V_e^{-1}\int_{\Omega_e}\boldsymbol{Bu}\, d\Omega \tag{2.12}$$

where the volume of finite element e is defined by

$$V_e = \int_{\Omega_e} d\Omega \tag{2.13}$$

Equation 2.12 justifies the "mean-strain" label for the presented finite element approach. Equation 2.12 can be rewritten using Equation 2.2 as

$$\bar{\boldsymbol{\varepsilon}} = V_e^{-1} \int_{\Omega_e} \boldsymbol{\varepsilon} d\Omega = V_e^{-1} \int_{\Omega_e} \boldsymbol{B}\boldsymbol{u}\, d\Omega = \left(V_e^{-1} \int_{\Omega_e} \boldsymbol{B}\, d\Omega \right) \boldsymbol{u} = \bar{\boldsymbol{B}}\boldsymbol{u} \tag{2.14}$$

where we obtain the operator to produce assumed strains from displacements as

$$\bar{\boldsymbol{u}} = V_e^{-1} \int_{\Omega_e} \boldsymbol{B}\, d\Omega \tag{2.15}$$

This strain-displacement operator is distantly related to the $\bar{\boldsymbol{B}}$–method used to avoid locking in nearly incompressible materials [14]. Finally, Equation 2.5 can be written as sum of integrals over finite element domains as

$$\delta\Pi_u(\bar{\boldsymbol{\varepsilon}}, \bar{\boldsymbol{\sigma}}, \boldsymbol{u}) = \sum_e \int_{\Omega_e} \bar{\boldsymbol{\sigma}}^T \boldsymbol{B} \delta\boldsymbol{u}\, d\Omega - \delta\mathcal{W} = 0 \tag{2.16}$$

Substituting Equation 2.15 in Equation 2.16 together with the uniformity of $\bar{\boldsymbol{\sigma}}$ within each element gives

$$\delta\Pi_{\boldsymbol{u}}(\bar{\boldsymbol{\varepsilon}}, \bar{\boldsymbol{\sigma}}, \boldsymbol{u}) = \sum_e V_e \bar{\boldsymbol{\sigma}}^T \bar{\boldsymbol{B}} \delta\boldsymbol{u} - \delta\mathcal{W} = 0 \tag{2.17}$$

We substitute Equation 2.11 and Equation 2.14 in Equation 2.17 to obtain the displacement variational equation

$$\delta\Pi_{\boldsymbol{u}}(\bar{\boldsymbol{\varepsilon}}, \bar{\boldsymbol{\sigma}}, \boldsymbol{u}) = \sum_e V_e \boldsymbol{u}^T \bar{\boldsymbol{B}}^T \boldsymbol{D} \bar{\boldsymbol{B}} \delta\boldsymbol{u} - \delta\mathcal{W} = 0 \tag{2.18}$$

where we recognize the element-wise stiffness matrix as

$$\mathbf{K}_{e,ms} = V_e \bar{\boldsymbol{B}}^T \boldsymbol{D} \bar{\boldsymbol{B}} \tag{2.19}$$

The stiffness matrix in Equation 2.19 is generated only by the constant-strain modes. Using this stiffness matrix alone leads to the formation of hourglass modes, and stabilization is required to avoid these spurious modes [26, 27, 18].

2.2 Stabilization

This section deals with the stabilization material and the corresponding strain energy defined to suppress the rigid body modes. Here "stabilization" is to be understood in a sense distinct from the use of the word in the design of stable mixed methods [28]. A quasi-optimal energy sampling technique was used to define the stabilization material in [23, 24]. The strain energy in (2.4) is supplemented by simultaneous addition and subtraction of the so-called stabilization energy based on (a) the displacement based strains and (b) the mean-strains, so that we can write for element e,

$$\Psi_e = \int_{\Omega_e} \mathcal{U}(\bar{\boldsymbol{\varepsilon}}) d\Omega + \int_{\Omega_e} \hat{\mathcal{U}}(\boldsymbol{\varepsilon}) d\Omega - \int_{\Omega_e} \hat{\mathcal{U}}(\bar{\boldsymbol{\varepsilon}}) d\Omega \tag{2.20}$$

where the stabilization energy is generated either by the displacement-based strains $\boldsymbol{\varepsilon}$ or the mean-strains $\bar{\boldsymbol{\varepsilon}}$. The stabilization energy densities are given by

$$\hat{\mathcal{U}}(\boldsymbol{\varepsilon}) = \frac{1}{2} \boldsymbol{\varepsilon}^T \hat{\boldsymbol{D}} \boldsymbol{\varepsilon} \qquad \text{and} \qquad \hat{\mathcal{U}}(\bar{\boldsymbol{\varepsilon}}) = \frac{1}{2} \bar{\boldsymbol{\varepsilon}}^T \hat{\boldsymbol{D}} \bar{\boldsymbol{\varepsilon}} \tag{2.21}$$

The stabilization material elasticity tensor $\hat{\boldsymbol{D}}$ is discussed below. Recalling that the mean strains are uniform element-wise, we write

$$\Psi_e = V_e\ \mathcal{U}(\bar{\boldsymbol{\varepsilon}}) + \int_{\Omega_e} \hat{\mathcal{U}}(\boldsymbol{\varepsilon})\ d\Omega - V_e\ \hat{\mathcal{U}}(\bar{\boldsymbol{\varepsilon}}) \tag{2.22}$$

The second term in (2.22) is computed using full quadrature to avoid spurious modes of deformation. An explicit expression for the strain energy of a finite element e can be written as

$$\Psi_e = \frac{1}{2}V_e \boldsymbol{u}^T \bar{\boldsymbol{B}}^T \boldsymbol{D}\bar{\boldsymbol{B}}\boldsymbol{u} + \frac{1}{2}\int_{\Omega_e} \boldsymbol{\varepsilon}^T \hat{\boldsymbol{D}}\boldsymbol{\varepsilon}\ d\Omega - \frac{1}{2}V_e \boldsymbol{u}^T \bar{\boldsymbol{B}}^T \hat{\boldsymbol{D}}\bar{\boldsymbol{B}}\boldsymbol{u} \tag{2.23}$$

The stiffness matrix associated with the stabilization energy can then be put as

$$\mathbf{K}_{e,stab} = \int_{\Omega_e} \boldsymbol{B}^T \hat{\boldsymbol{D}}\boldsymbol{B}\ d\Omega - V_e \bar{\boldsymbol{B}}^T \hat{\boldsymbol{D}}\bar{\boldsymbol{B}} \tag{2.24}$$

The non-zero eigenvalues of the stiffness matrix $\mathbf{K}_{e,ms}$ in (2.19) correspond to the constant-strain modes. The stabilization stiffness matrix $\mathbf{K}_{e,stab}$ is added to $\mathbf{K}_{e,ms}$ to boost the rank of the overall stiffness matrix to 18 for a hexahedral element and to 24 for a quadratic tetrahedral element [23, 24]. Thus the stability of the method is guaranteed as long as the elasticity tensors corresponding to the real and stabilization materials are positive-definite.

The stabilization material is constructed such that the elasticity tensor corresponding to the material is positive-definite, and does not have one or more relatively very large eigenvalues (such as in the case of a nearly incompressible material) [23]. For simplicity, the stabilization material is usually taken as isotropic and hence it is defined as a function of a modified Young's Modulus $\hat{E}$, and modified Poisson's ratio $\hat{\nu}$. The Poisson's ratio $\hat{\nu}$ is chosen such that the stabilization material is compressible as

$$\hat{\nu} = \begin{cases} \nu & : \quad \nu \leq 0.3 \\ \dfrac{\nu + 0.3}{2} & : \quad \nu \geq 0.3 \end{cases} \tag{2.25}$$

where ν is the Poisson's ratio of an isotropic real material. If the real material is orthotropic, the minimum of the Poisson's ratios $(\nu_{12}, \nu_{13}, \nu_{23})$ of the material ν_{min} is used in (2.25) instead of ν.

The Young's Modulus $\hat{E}$ is modified so as to make it possible for the element to represent the bending deformation energy accurately even when highly distorted. As demonstrated for instance in [19] on Timoshenko beam elements, shear locking occurs due to a spurious constraint being imposed when exact integration is used to evaluate the strain energy. The flexural rigidity of the beam artificially increases due to this spurious constraint. In [19], reduced integration is used on the bending part of strain energy to eliminate locking. This has the same effect as that of multiplying the Young's Modulus E of the real material by a form factor which is a function of the shape of the element.

As discussed in detail in [23], this argument can also be made for hexahedral finite elements. The Young's modulus of the stabilization material is obtained by multiplying a form factor which incorporates the aspect ratio of the element as

$$\hat{E} = E\frac{\Phi}{1+\Phi} \tag{2.26}$$

For orthotropic real materials, we use the minimum of Young's moduli (E_1, E_2, E_3) of the material E_{min} in place of E in (2.26).

The Φ in the form factor depends on the stabilization material properties and the geometry of the element. For H8MSGSO elements, Φ is given by

$$\Phi = 2(1+\hat{\nu})\frac{\mathtt{min}[h_x^2, h_y^2, h_z^2]}{\mathtt{max}[h_x^2, h_y^2, h_z^2]} \tag{2.27}$$

where h_x, h_y, h_z are the characteristic heights of a hexahedral element [23].

A slight modification is adopted for quadratic mean-strain tetrahedral elements [24]. The factor Φ is assumed to be inversely proportional to some positive power of condition number of the Jacobian of the mapping from the parametric space to the physical space. The condition number of a matrix is the ratio of the magnitudes of the maximum and minimum singular values of the matrix. Thus, condition number of the Jacobian gives a measure of the aspect ratio of the element. Therefore, the form factor Φ takes into account the shape of the element, and makes it possible for the element to improve the coarse-mesh response in configurations in which the element is very distorted, such as thin plates or shells. The form factor for a quadratic tetrahedral element was adopted in [24] as

$$\Phi = 10^4 \left(\frac{1}{\mathtt{cond}(\boldsymbol{J})} \right)^{2.6} \tag{2.28}$$

where $\mathtt{cond}(\boldsymbol{J})$ is the condition number of the Jacobian $\boldsymbol{J}$ of the quadratic tetrahedral element [24]. For both H8MSGSO and QT10MS, the maximum of the form factors computed at the integration points of an element is chosen as the form factor for that element.

Therefore, the elasticity tensor of the stabilization material can be computed from the Young's Modulus and Poisson's ratio of the real material, and importantly, the geometry of the finite element. This formulation helps in softening the bending response by adjusting the compressible stabilization material in accordance with the finite element geometry along with the material properties.

The stabilized mean-strain elements are demonstrated to be coarse-mesh accurate and devoid of locking in [20, 21] for linear elastic applications and in [29] for nonlinear applications. These works also show that the pressure oscillations originally seen in T10 elements perish when using the QT10MS elements in the presence of near-incompressibility. However, these works use the mean stress as the candidate stress field, which is devoid of oscillations, but is only first-order convergent for quadratic tetrahedral elements which is suboptimal (second order convergence is expected of quadratic elements).

The next chapter aims at developing a novel and consistent stress field for the stabilized mean-strain finite elements, which demonstrate an optimal order convergence for the stresses. Several examples are shown in the next chapter to demonstrate the optimality of convergence, whilst avoiding stress oscillations, inherent in T10 elements in the presence of near-incompressibility.

Chapter 2 has many details taken from the manuscript, “Sivapuram R, Krysl P. Improved Recovered Nodal Stress for Mean-Strain Finite Elements. *Finite Elements in Analysis and Design* 2018; **146**:70-83, doi:10.1016/j.finel.2018.04.005”, and the work is done in collaboration with Prof. Petr Krysl. The dissertation author is the primary investigator of the manuscript.

Chapter 3

Improved Stress Recovery for Mean-Strain Finite Elements

A few recent publications described high-performance mean-strain finite elements based upon the idea that the rank-deficient mean-strain element can be stabilized (in the sense of correcting the rank deficiency) by setting up two forms of stabilization energy that is sampled with the full quadrature rule or with the mean-strain quadrature [22, 31, 23, 32, 33, 24]. These elements achieve insensitivity to material constraints (for instance isochoric), and they are applicable to the modeling of thin structures. The mean-strain approach however makes the stress post-processing more challenging. While the stresses are uniform element-wise, the mean-strain elements achieve high accuracy in displacements. Consequently it is reasonable to expect that using the accuracy inherent in the displacement solution, there might be some way of boosting the accuracy of the stresses as well. This is the motivation for the present work.

The stress values in Finite Element Analysis (FEA) are connected to the integration points. A common post-processing operation for stresses in FEA is to recover continuous stress fields from the quadrature-point stresses. In order to visualize the stress distribution, the stress is extrapolated from the quadrature points to the nodes of each element. Then the stress field can be visualized element-wise using filled-contour plots, isosurfaces, etc., but it is (typically) discontinuous at the inter-element boundaries. Alternatively, the nodal stresses can be made unique at each node shared by several finite elements by some form of “averaging” of the element-wise stress predictions at the node. In order for this averaging to work well, the stress predictions at the nodes of each element must be of good quality. This condition is not satisfied when using the mean-strain elements, such as the elements proposed in [22, 31, 23, 32, 33, 24], or the hexahedral elements implemented in the Abaqus solvers [34]. In this work, we attempt to improve accuracy of the integration-point stresses extrapolated to the nodes of an element.

First, let us mention some procedures from literature for extracting nodal quantities from an element. One popular technique for improved stress approximation is the ‘superconvergent patch recovery’ (SPR) method developed by [35]. It is developed based on the presence of superconvergent points in a finite element, where the stresses have an order of accuracy higher than rest of the finite element region. The stresses are fitted using a polynomial of one order higher than that of the strains, in a least squares sense. However, the presence of superconvergent points is not always guaranteed, for example, in curved elements. Also, in some element configurations, for instance, elements located at corners or at edges of three-dimensional geometries may not provide enough superconvergent points around a given node to enable the requisite least-squares solution. In this case the SPR, extrapolation fails and needs to be replaced with a simpler, less accurate, procedure.

The nodal point forces in a finite element were used by [36, 37] to compute interpolated stresses which are shown to be enhanced in quality as compared to the directly-computed stresses in triangle, quadrilateral and tetrahedral elements. The stresses at a node are computed using an average over a patch of elements containing the node. Since the stresses computed are based on the real material, achieving improved stress approximation in nearly incompressible materials is difficult. An enhanced stress approximation was proposed in [38] by assuming a richer interpolation space for the stresses and by improving the fulfillment of equilibrium by weakening the equilibrium in a small patch of elements.

3.1 Improved Recovered Nodal Stress

The stress values in FEA are connected to the integration points. With the exception of interfaces between materials with different properties and of surfaces with discontinuous externally applied loading, stress fields are generally continuous in the spatial coordinates. In order to present the stresses computed from FEA, one generally uses a post-processing operation to recover continuous stress fields from the quadrature-point stresses. One possibility is to compute unique stresses at the nodes by (possibly weighted) averaging of the stress values at each of the nodes computed using all the finite elements sharing the node in the mesh. In turn, the stress components at the nodes in each element need to be computed from the stresses at the integration points.

In the mean-strain elements the stress is uniform across each element. We can think of this situation as each element using just one integration point. As a consequence, using just the information from a single integration point, the best we can do to predict the stress values at the nodes of the element is to assume that it is the mean-strain generated uniform stress. Evidently, this is not very accurate. In effect, the convergence of stress quantities is then of first order at most. (This issue is common to mean-strain elements, c.f. [22, 31, 23, 32, 33, 24] or [34]).

In contrast, the standards displacement-based isoparametric tetrahedral element with a constant Jacobian matrix can represent linearly-varying stress fields. The stresses at nodes can then be obtained by linear extrapolation from the quadrature-point data, from the commonly used four-point rule. For a quadrature rule with more points, a least squares fitting procedure may be applied. Consequently, the continuous nodal stress field may then result in a quadratic convergence. Note well that this analysis ignores the well-known failings of the isoparametric tetrahedron - wild oscillations in stresses for constrained materials, and shear locking in distorted configurations. Under conditions where theses flaws can be expected, the convergence of stresses is obviously much worse than what is theoretically predicted.

The question is whether we can improve the mean-strain element behavior to increase the accuracy of the predicted continuous stress fields. Since the displacement field itself is quite accurate, and in fact converges at the correct rate, it seems reasonable to expect the existence of some mechanism to increase the accuracy of stress predictions from the displacement field information.

The strain energy in a finite element from Equation 2.20 can be written with the substitution of quadratic forms for the individual deformation energy contributions as

$$\Psi_e = \frac{1}{2}\int_{\Omega_e} \bar{\boldsymbol{\varepsilon}}^T \boldsymbol{D} \bar{\boldsymbol{\varepsilon}} \, d\Omega + \frac{1}{2}\int_{\Omega_e} \boldsymbol{\varepsilon}^T \hat{\boldsymbol{D}} \boldsymbol{\varepsilon} \, d\Omega - \frac{1}{2}\int_{\Omega_e} \bar{\boldsymbol{\varepsilon}}^T \hat{\boldsymbol{D}} \bar{\boldsymbol{\varepsilon}} \, d\Omega \tag{3.1}$$

Recalling that the strain energies due to the mean-strains are element-wise constant, the strain energy in Equation 3.1 can be rearranged to obtain

$$\Psi_e = \frac{1}{2} V_e \bar{\boldsymbol{\varepsilon}}^T (\boldsymbol{D} - \hat{\boldsymbol{D}}) \bar{\boldsymbol{\varepsilon}} + \frac{1}{2}\int_{\Omega_e} \boldsymbol{\varepsilon}^T \hat{\boldsymbol{D}} \boldsymbol{\varepsilon} \, d\Omega \tag{3.2}$$

Introducing Equation 2.12 into Equation 3.2 leads to the expression

$$\Psi_e = \frac{1}{2}\int_{\Omega_e} \boldsymbol{\varepsilon}^T \left((\boldsymbol{D} - \hat{\boldsymbol{D}}) \bar{\boldsymbol{\varepsilon}} + \hat{\boldsymbol{D}} \boldsymbol{\varepsilon} \right) d\Omega = \frac{1}{2}\int_{\Omega_e} \boldsymbol{\varepsilon}^T \left(\boldsymbol{D} \bar{\boldsymbol{\varepsilon}} - \hat{\boldsymbol{D}} \bar{\boldsymbol{\varepsilon}} + \hat{\boldsymbol{D}} \boldsymbol{\varepsilon} \right) d\Omega \tag{3.3}$$

Using the notation $\bar{\boldsymbol{\sigma}} = \boldsymbol{D}\bar{\boldsymbol{\varepsilon}}$, $\hat{\boldsymbol{\sigma}} = \hat{\boldsymbol{D}}\boldsymbol{\varepsilon}$, and $\hat{\bar{\boldsymbol{\sigma}}} = \hat{\boldsymbol{D}}\bar{\boldsymbol{\varepsilon}}$, Equation 3.3 gives the neat expression

$$\Psi_e = \frac{1}{2}\int_{\Omega_e} \boldsymbol{\varepsilon}^T (\bar{\boldsymbol{\sigma}} - \hat{\bar{\boldsymbol{\sigma}}} + \hat{\boldsymbol{\sigma}}) \, d\Omega \tag{3.4}$$

The difference between $\hat{\bar{\boldsymbol{\sigma}}}$ and $\hat{\boldsymbol{\sigma}}$ tends to zero with the element size, but the trend of $(-\hat{\bar{\boldsymbol{\sigma}}} + \hat{\boldsymbol{\sigma}})$ inside each finite element remains non-trivial and is worth capturing. Therefore, we construct a linear extrapolation of $(-\hat{\hat{\boldsymbol{\sigma}}}+\hat{\boldsymbol{\sigma}})$ over the entire finite element, using the integration points as the sampling points, thus replacing $(-\hat{\hat{\boldsymbol{\sigma}}}+\hat{\boldsymbol{\sigma}})$ by $(-\hat{\hat{\boldsymbol{\sigma}}}+\hat{\boldsymbol{\sigma}}_{ex})$, where $\hat{\boldsymbol{\sigma}}_{ex}$ is the linearly extrapolated stabilization stress field. Using $\tilde{\boldsymbol{\sigma}} = \bar{\boldsymbol{\sigma}} - \hat{\hat{\boldsymbol{\sigma}}} + \hat{\boldsymbol{\sigma}}_{ex},$ we obtain

$$\Psi_e = \frac{1}{2}\int_{\Omega_e} \boldsymbol{\varepsilon}^T \tilde{\boldsymbol{\sigma}}\, d\Omega \tag{3.5}$$

Note that the stress field $\tilde{\boldsymbol{\sigma}}$ varies across the element. The stress fields $\bar{\boldsymbol{\sigma}}, \hat{\hat{\boldsymbol{\sigma}}}$ are uniform within an element, but $\hat{\boldsymbol{\sigma}}_{ex}$ varies linearly across the element. Also, note that the stress field $\bar{\boldsymbol{\sigma}}$ is consistent with the displacement field (which, as pointed out above, is of the correct accuracy). Therefore equation Equation 3.5 appears to be a recipe for extrapolating from the quadrature points to the nodes and achieving the full accuracy of the nodal stress field: instead of the stress field $\bar{\boldsymbol{\sigma}}$ (the stress in the real material), we extrapolate $\tilde{\boldsymbol{\sigma}}$ (the stress in real material, with a portion of the stress in the stabilization material) to the nodes of an element.

The replacement of $\hat{\boldsymbol{\sigma}}$ with $\hat{\boldsymbol{\sigma}}_{ex}$ is justified as follows: For constant-Jacobian elements the displacement field is quadratic inside a mean-strain quadratic tetrahedral QT10MS element, and trilinear inside a mean-strain hexahedral H8MSGSO element, and therefore the strains (and the stresses) can be well behaved (fully or partially linear). For elements with non-constant Jacobian (elements with curved or distorted faces), the stresses within an element vary not as simple polynomials but rather as rational expressions, which tend to misbehave for distorted elements. Therefore, we propose not to compute the stress field $\hat{\boldsymbol{\sigma}}$ directly from the displacement field, but rather to take a linear least-squares fit to $\hat{\boldsymbol{\sigma}}$, to which we add the uniform $\bar{\boldsymbol{\sigma}} - \hat{\hat{\boldsymbol{\sigma}}}$.

The linear least-squares fit to $\hat{\boldsymbol{\sigma}}$ is obtained from the stabilization stresses at the integration points of the finite element. A linear fitting model has 4 coefficients, a constant and one coefficient for each of the spatial dimensions. The QT10MS element has 4 integration points giving a determined system of equations, whilst the H8MSGSO element has 8 integration points, giving an over-determined system of equations.

The aforementioned stress computation procedures are applicable to the mean-strain finite elements as well. In comparison, the present approach has perhaps the advantage of simplicity, which may translate to a higher computational efficiency.

3.2 Examples

In this section, we present results for stresses represented by nodal values. We compute the values of the stress component(s) at the nodes of an element by extrapolating (extending) the stress within an element: either from the mean stress $\bar{\boldsymbol{\sigma}}$, referred to below as mean-stress-only extrapolation (abbreviation MSOE), or using the improved recovery procedure with least square fitted $\tilde{\boldsymbol{\sigma}}$, referred to as trend-based extrapolation (abbreviation TBE).

The unique stress values at a particular node are then computed as simple averages of stress values from each element that shares this node. Some comparisons in what follows are done with elements implemented in the Abaqus software, which also use this averaging procedure to produce smoothed stress results [34].

The elements included in the tests were:

QT10MS The quadratic tetrahedral mean-strain element of [24].

H8MSGSO The hexahedral mean-strain element of [23].

T10 The standard isoparametric (purely displacement-based) 10-node tetrahedron with four-point quadrature.

H8 The standard isoparametric (purely displacement-based) eight-node hexahedron with Gaussian eight-point quadrature.

C3D10HS Tetrahedral Abaqus element designed for improved surface stress visualization, hybrid version with ten nodes [34].

C3D8HS Hexahedral Abaqus element designed for improved surface stress visualization, hybrid version with eight nodes [34].

C3D8S Hexahedral Abaqus element designed for improved surface stress visualization, non-hybrid version with eight nodes [34].

C3D8I Hexahedral Abaqus eight-node element with incompatible modes [34].

C3D8R Hexahedral Abaqus eight-node element with uniformly reduced integration and enhanced hourglass stabilization [34].

3.2.1 Elliptic Membrane

This elliptic membrane example is a benchmark problem (LE1) of NAFEMS, originally tested using plane-stress elements [39, 40]. Figure 3.1 shows the elliptic membrane (of thickness 0.1 m) with the boundary conditions and a uniform outward pressure ($P = 10$ MPa) applied on the surface *BC*. The Young's modulus of the membrane is 210 GPa, and the Poisson's ratio is 0.3. Only one eighth of the membrane is modeled owing to symmetry in the thickness direction. The model is discretized using QT10MS and H8MSGSO elements. The original benchmark document specified the target solution for normal stress σ_{yy} at Point *D* as 92.7 MPa [39].

Figures 3.2 and 3.3 show the errors of the normal stress σ_{yy} at Point *D* with mesh refinement using quadratic tetrahedral and hexahedral elements respectively. The true errors in the stress obtained by MSOE and TBE are compared with the errors of stress obtained using Abaqus elements designed for improved surface stress visualization (C3D10HS and C3D8HS). The results demonstrate a significant improvement in the accuracy of stress predictions using the TBE as compared to the MSOE for the QT10MS element, and marginal improvement for the H8MSGSO element. This is expected, because the TBE stresses use multiple stress sampling points in a finite element unlike the element-wise constant mean stresses. Comparing with the improved-stress-response Abaqus elements also confirm that the current procedure delivers

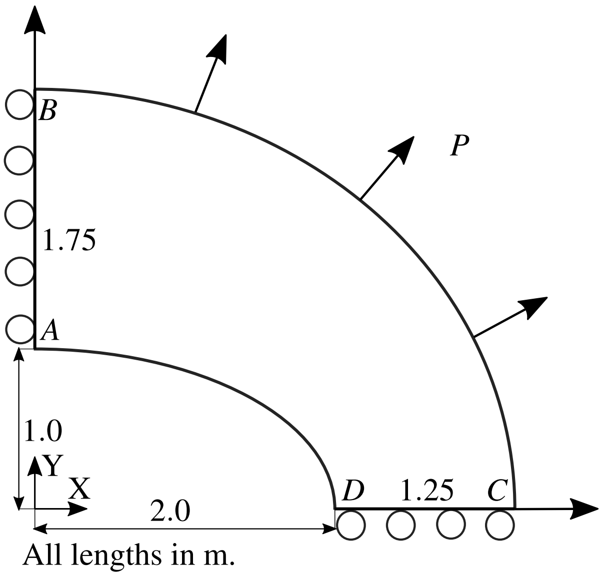

Figure 3.1: Elliptic membrane

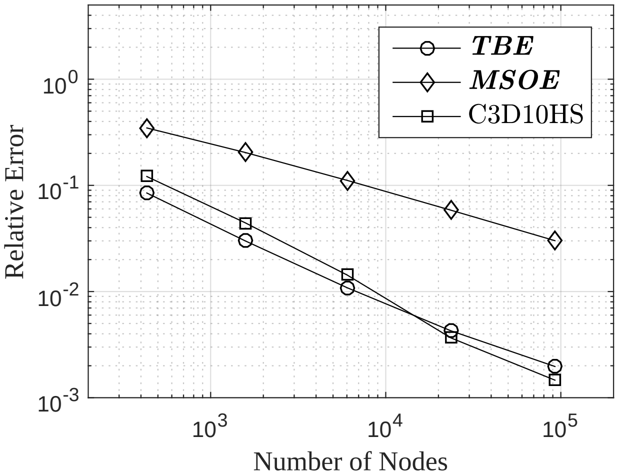

Figure 3.2: LE1 benchmark. Errors in σ_{yy} at Point D with mesh refinement (Quadratic Tetrahedral elements)

equivalent accuracy for the tetrahedron, whereas the improved-stress Abaqus hexahedron is in absolute terms more accurate than either of the extrapolation procedures for the H8MSGSO element.

It is worthwhile to stress that the convergence rate for the hexahedral elements remains linear, as expected: the stabilization stresses themselves are first order in the hexahedral elements,

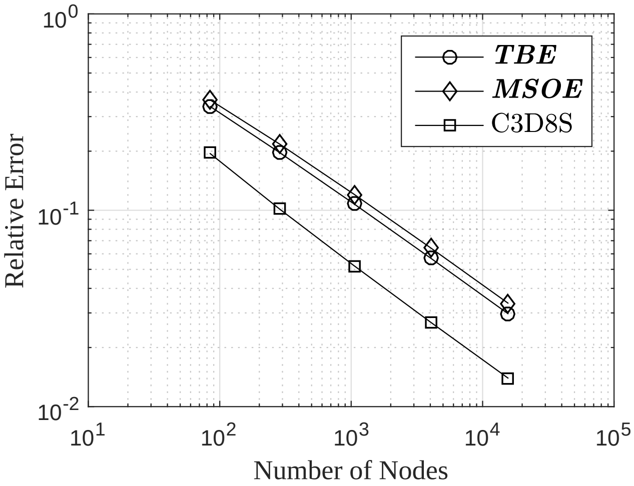

Figure 3.3: LE1 benchmark. Errors in σ_{yy} at Point D with mesh refinement (Hexahedral elements)

and hence the extrapolation from the stabilization stresses cannot produce more than first-order convergence rate. On the other hand, it is clear from Figure 3.2 that for the mean-strain tetrahedral elements the convergence rate of the TBE stresses attains the theoretical second-order accuracy, while the MSOE stresses remain first order. Evidently, the improved extrapolation procedure is of considerable value in the quadratic tetrahedral case.

Further we consider the convergence of the stress $\boldsymbol{\sigma}$ in the global RMS (L^2) norm in quadratic tetrahedral and hexahedral elements. Consider a convergence study over meshes $M_1, M_2, ..., M_n$ in increasing order of mesh fineness. Then the normalized approximate error in quantity q measured on mesh M_i is given by

$$E_i(q) = \frac{||q_i - q_{i-1}||_{M_i}}{||q_n||_{M_n}} \tag{3.6}$$

where the norm $||\cdot||_{M_i}$ is defined for a quantity q by

$$||q||^2_{M_i} = \int_{M_i} |q|^2 d\mathbf{x} \tag{3.7}$$

This means that the quantity q_{i-1} needs to be transferred by interpolation from the coarse mesh

M_{i-1} to the fine mesh M_i.

We compare the performance of TBE and MSOE for quadratic tetahedral elements using this error measure. The performance of the T10 stresses (T10E) is compared after extrapolating the stresses from integration points to the nodes and subsequently averaging at the nodes. Figure 3.4a shows the coarsest mesh used for the convergence study and the other refinements are obtained by refining this mesh in the XY-plane. Figure 3.5 shows the convergence of the normalized approximate error in stresses with mesh refinement. We observed orders of convergence of 1.93 for both TBE and T10E, while the MSOE converged only with an order of 1.28. The TBE and T10E have similar convergence because the material is compressible, and they have a close to second order convergence which is expected of quadratic elements. Consequently we consider this evidence that the proposed TBE procedure increases the convergence rate of the stresses to the theoretical second-order accuracy.

Next the normalized approximate RMS error in $\boldsymbol{\sigma}$ is compared for TBE and MSOE for hexahedral elements. The stresses from H8 elements (H8E) are used for comparison, after extrapolating the stresses from integration points to the nodes and then averaging at the nodes. Figure 3.4b shows the coarsest mesh used for the convergence study. The mesh refinements are performed to this mesh in the XY-plane. Figure 3.6 shows the convergence of stresses, and once again, TBE displays lower errors in stresses than MSOE. The orders of convergence observed for TBE, MSOE and H8E are 1.447, 1.441 and 1.446 respectively. The orders of convergence are similar, but the plot demonstrates that TBE stresses have a slightly lower error than the MSOE stresses.

3.2.2 Thick Plate Under Pressure

A 0.6 m thick plate under pressure is considered in this example (LE 10 benchmark of NAFEMS [40, 39]). The Young's modulus is 210 GPa and the Poisson's ratio is 0.3. The loading is a uniform normal pressure load of 1 MPa on the top face of the plate *ABCD*, as shown in Figure

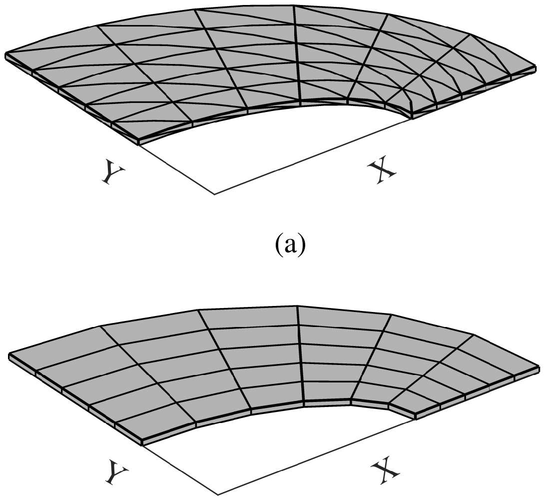

(a)

(b)

Figure 3.4: LE1 Benchmark, Coarsest meshes used for mesh refinement study (a) Quadratic Tetrahedral elements (b) Hexahedral elements

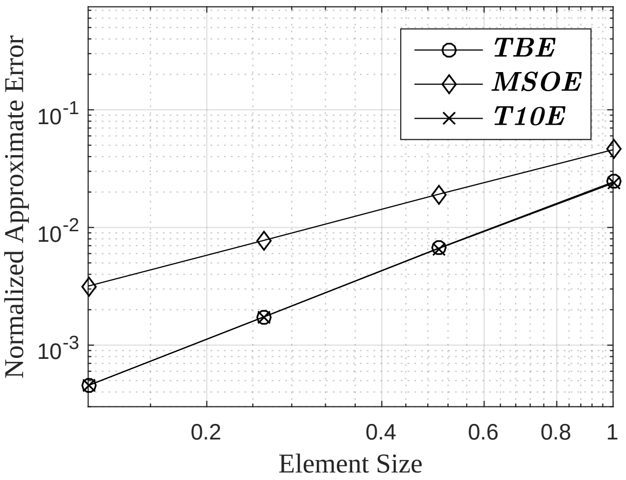

Figure 3.5: LE1 benchmark. Convergence of normalized approximate error in stress (Quadratic tetrahedral elements)

3.7. The faces $DCC'D'$ and $BAA'B'$ are fixed in their normal directions (Y and X respectively), and the curved edge EE' is fixed in the direction (Z) of loading. The displacements parallel to the plane $ABCD$, i.e., X and Y displacements are constrained on the face $CBB'C'$. The specified target solution for normal stress in the benchmark document is $\sigma_{yy} = -5.38$ MPa at point D [39].

Figure 3.8 shows the relative errors in σ_{yy} at Point D as mesh is refined, computed with

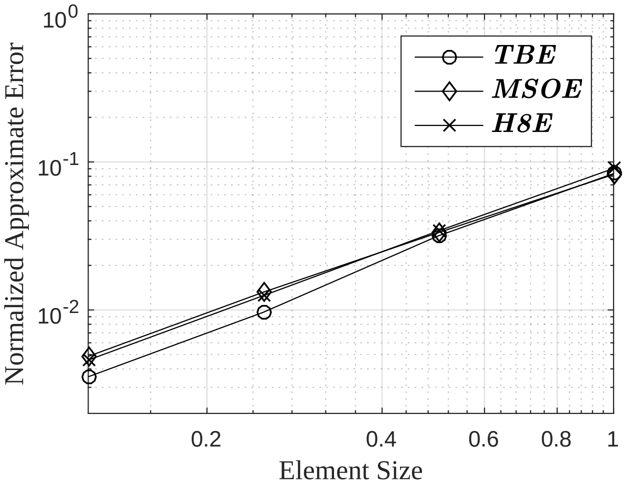

Figure 3.6: LE1 benchmark. Convergence of normalized approximate error in stress (Hexahedral elements)

mean-strain quadratic tetrahedral elements QT10MS using the TBE, MSOE and with Abaqus improved-stress (C3D10HS) elements. The improved stress approximation obtained using TBE can be clearly observed.

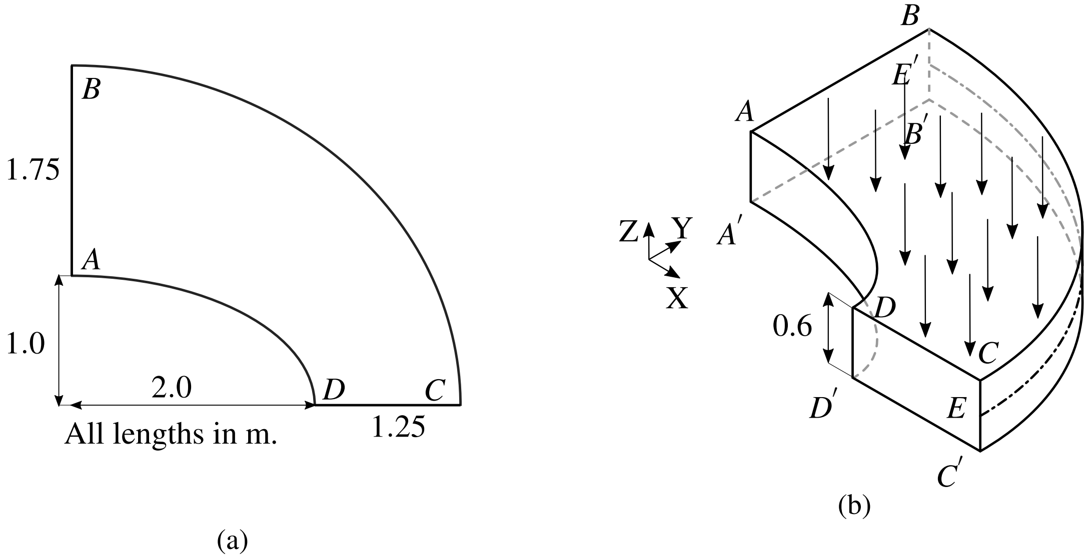

Figure 3.7: Benchmark LE10, Thick Plate Under Pressure. (a) Cross-sectional view (b) 3-D view

Figure 3.9 shows the relative errors in σ_{yy} at Point D as the hexahedral mesh is refined

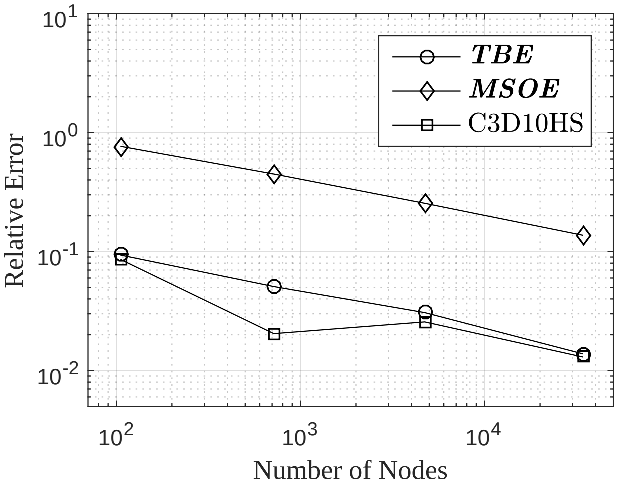

Figure 3.8: LE10 benchmark, Quadratic Tetrahedral elements. Normalized errors in σ_{yy} at Point *D*.

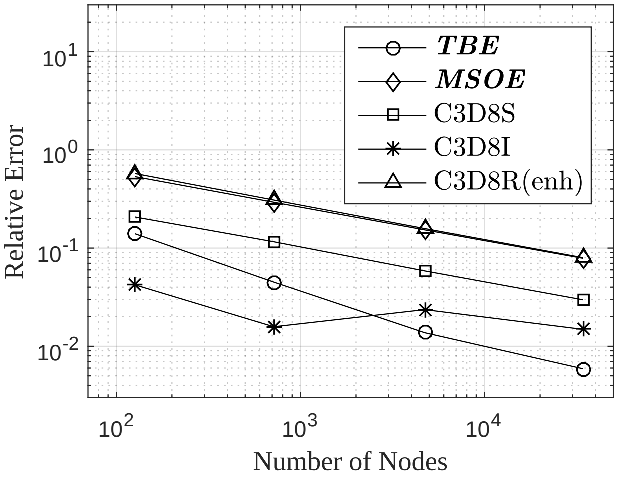

Figure 3.9: LE10 benchmark, Hexahedral elements. Normalized errors in σ_{yy} at Point *D*.

using TBE, MSOE, Abaqus improved-stress C3D8S, Abaqus incompatible-mode hexahedron C3D8I and Abaqus C3D8R (elements with reduced integration and enhanced hourglass stabilization). The results show that the incompatible-mode hexahedron C3D8I delivers superior accuracy in this case for coarser meshes, but fails to maintain the convergence rate. The element with reduced integration and enhanced hourglass stabilization C3D8R from Abaqus, which is one of the best elements available in their finite element library, apparently also uses extrapolation from the mean stresses: its accuracy is equivalent to our MSOE stresses. The TBE stresses are better than stresses obtained using the improved-stress hexahedron C3D8S for this example.

3.2.3 Slab with a circular hole under far-field tension loading

A slab 0.1 m thick with stress-free circular hole of radius $R_1 = 0.1$ m, under far-field unidirectional tensile loading $P = 0.1$ MPa, is considered [41]. The Young's Modulus is $E = 2.4$ MPa and Poisson's ratio is $\nu = 0.49995$ (nearly incompressible). Plane-strain conditions are simulated by fixing the faces parallel to the plane of page in Figure 3.10 in the direction normal to them. Owing to the two-plane symmetry of the model, only a quarter of the model is considered for analysis.

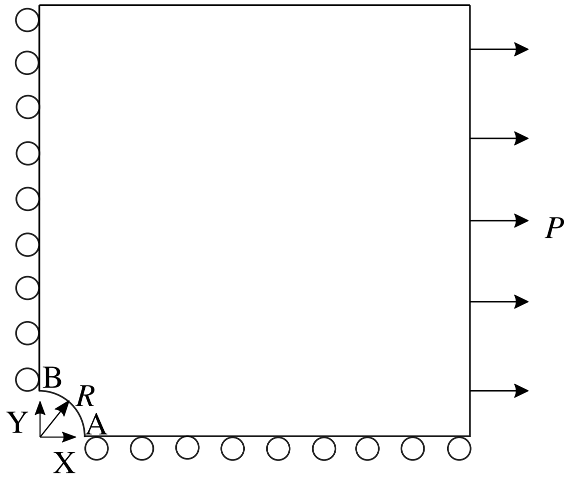

Figure 3.10: Quarter model of stress-free hole in a slab.

The direct stresses σ_{xx} and σ_{yy} follow from the radial and angular stress solutions given in [41] as

$$\begin{aligned}
\sigma_{xx} &= \frac{P}{2r^4}(3R^4\cos(4\theta) + 2r^4 - 3R^2r^2\cos(2\theta) - 2R^2r^2\cos(4\theta)) \\
\sigma_{yy} &= -\frac{PR^2}{2r^4}(3R^2\cos(4\theta) + r^2\cos(2\theta) - 2r^2\cos(4\theta)) \\
\sigma_{xy} &= -\frac{PR^2}{2r^4}(r^2\sin(2\theta) - 3R^2\sin(4\theta) + 2r^2\sin(4\theta)
\end{aligned} \tag{3.8}$$

where r is the distance from the center of the stress-free hole and θ is the anti-clockwise angle with respect to the horizontal X-axis.

First we consider quadratic tetrahedral elements. Figure 3.11 shows the element-wise distribution of σ_{xx} using the T10E stresses for the quadratic isoparametric tetrahedron (i.e. strain and stress are computed at the integration points and extrapolated to the nodes); the MSOE and the TBE for the mean-strain tetrahedral elements [24]; and the Abaqus C3D10HS improved-stress tetrahedral elements. For the T10E stresses we can predictably observe a noisy stress field since the material is nearly incompressible. The C3D10HS elements of Abaqus are designed to improve the bending representation of elements, dealing with near incompressibility, and for improving the surface stress visualization [42]. We can observe in Figure 3.11 that the MSOE and the TBE stresses are smoothly distributed, as are the C3D10HS stresses.

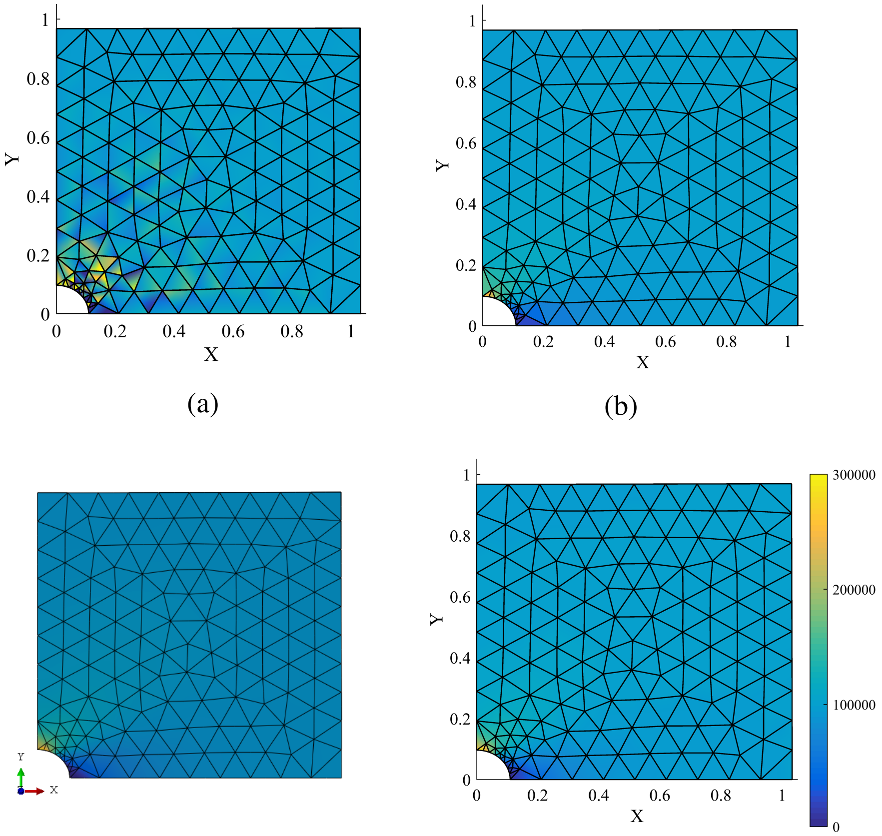

(a) (b)

(c) (d)

Figure 3.11: Hole in a slab (nearly incompressible material: $\nu = 0.49995$). Element-wise distribution of σ_{xx} in quadratic tetrahedral elements. (a) Directly-Computed stresses (T10E), (b) QT10MS MSOE stresses, (c) Abaqus C3D10HS Improved stresses, (d) QT10MS TBE stresses.

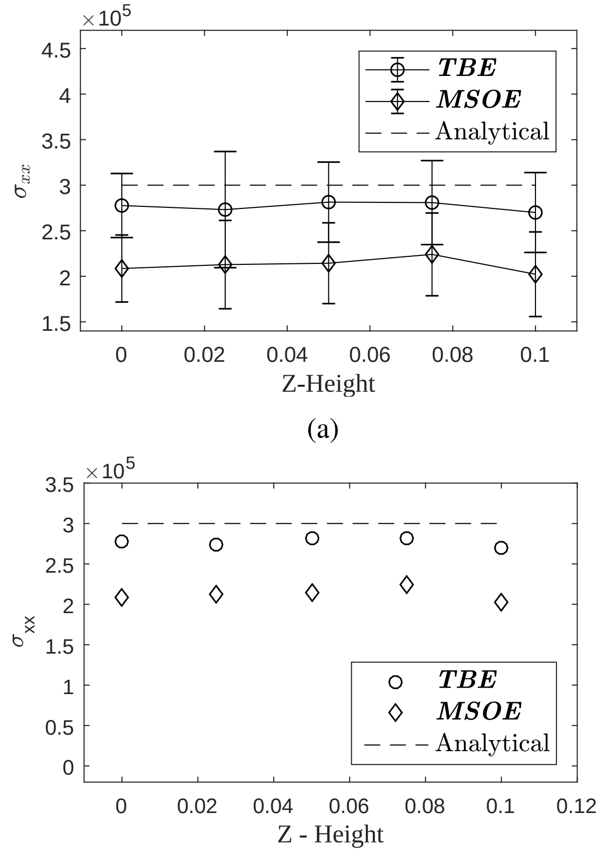

(a)

(b)

Figure 3.12: Hole in a slab (nearly incompressible material: $\nu = 0.49995$), quadratic tetrahedral mesh. Stress σ_{xx} along the edge containing Point *B*. (a) Elemental contributions of stresses, (b) Averaged stresses at the nodes.

For the same mesh that is shown in Figure 3.11, the stresses σ_{xx} on the edge containing Point *B* and parallel to the *Z*-axis are compared in Figure 3.12. Figure 3.12(a) shows the element-wise contributions (in the form of means and standard deviations; the two curves are distinguished by the length of the cross bars) of stresses at the nodes along that edge from all the elements connecting these nodes. The TBE stresses are observed to be superior to the MSOE stresses in terms of accuracy. Figure 3.12(b) shows the nodal stresses obtained by averaging the element-wise stresses at the nodes. The TBE stresses show an error of 7.9%, whilst the MSOE stresses have an error of 29.3%, clearly indicating the improvement in the performance of the TBE stresses over the MSOE stresses.

Next we consider hexahedral elements. Figure 3.13 shows the mesh used, with the distributions of MSOE stresses, Abaqus C3D8HS improved stresses and the TBE stresses. All stress distributions are observed to be smooth. For the same mesh, the stress σ_{yy} is visualized along the edge containing Point A parallel to the Z-axis in Figure 3.14. The elemental contributions of stresses at the nodes along the edge are the same as the average stresses at the nodes since the mesh is symmetric in the thickness direction. The proposed TBE method yields an RMS error of 17.1% in the stresses which implies a better quality when compared to the error of 51.2% of the MSOE stresses.

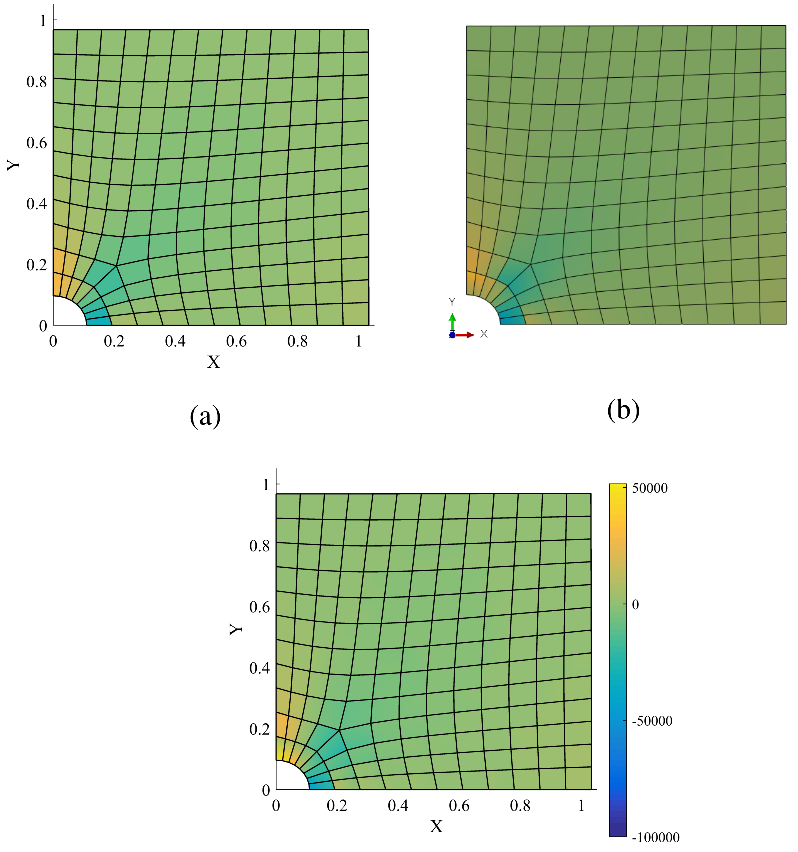

(a)

(b)

(c)

Figure 3.13: Hole in a slab (nearly incompressible material: $\nu = 0.49995$). Element-wise distribution of σ_{yy} in hexahedral elements. (a) H8MSGSO MSOE stresses, (b) Abaqus C3D8HS Improved-stress element, (c) H8MSGSO TBE stresses.

We switch to a different domain for the same problem: Figure 3.15 shows that we focus

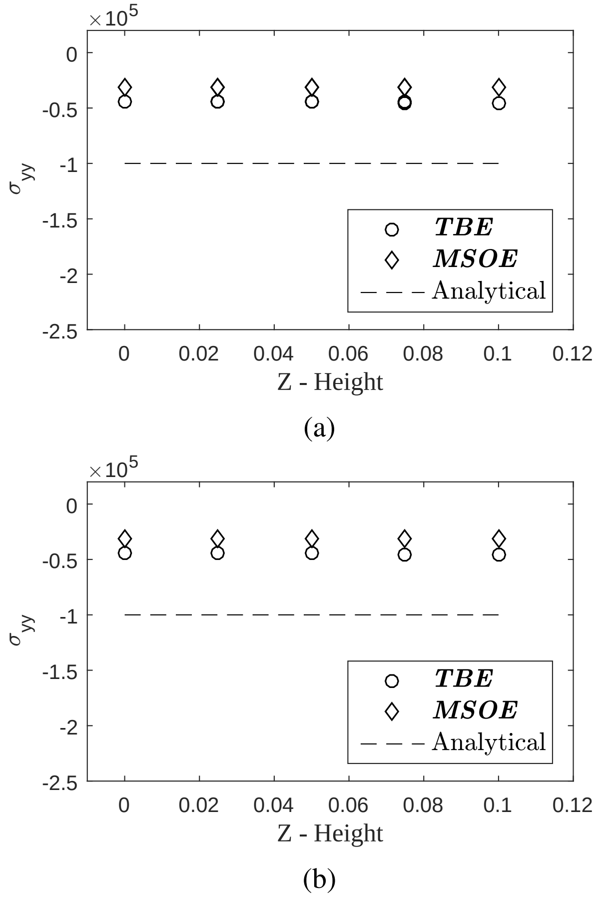

Figure 3.14: Hole in a slab (nearly incompressible material: $\nu = 0.49995$), hexahedral mesh. Stress σ_{yy} along the edge containing Point *A*. (a) Elemental contributions of stresses (b) Averaged stresses at the nodes.

on a region of radius $R_2 = 0.4$ m around the stress-free hole where the stresses are of interest. The tractions $(h_x, h_y, 0)$ are applied on the face *CD* as the natural boundary conditions,

$$\begin{aligned} h_x &= \sigma_{xx} n_x + \sigma_{xy} n_y \\ h_y &= \sigma_{xy} n_x + \sigma_{yy} n_y \end{aligned} \tag{3.9}$$

where $(n_x, n_y, 0)$ is the normal vector of the face *CD*.

The normal stress σ_{xx} is sampled at Point *B* of the model. We know that the stress concentration factor at Point *B* for this model is 3.0. A mesh refinement study of relative error in the average value of σ_{xx} computed along the edge containing Point *B* parallel to the *Z*-axis is

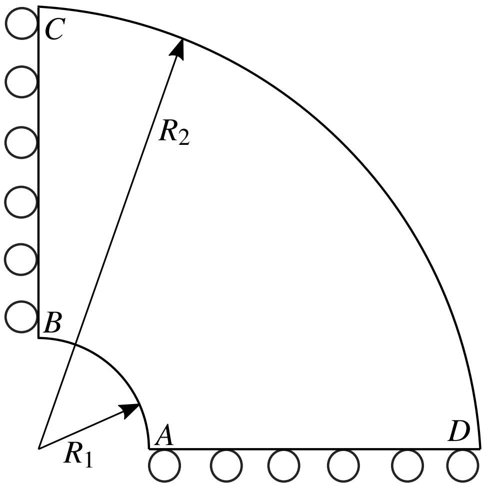

All lengths in m.

Figure 3.15: Quarter model of stress-free hole in a slab (focused around the stress-free hole).

conducted using the TBE, the MSOE and the Abaqus C3D10HS stresses for quadratic tetrahedral elements, as shown in Figure 3.17. The coarsest quadratic tetrahedral mesh used for the refinement study is shown in Figure 3.16a. The errors in stresses obtained using Abaqus C3D10HS elements can serve as a reference to the errors of TBE and MSOE stresses as the mesh is refined. Figure 3.18 shows errors in normal stress σ_{yy}, computed at Point A of the model.

The TBE stresses in 3.18 display an irregular reduction in error in the third mesh refinement because the stress σ_{yy} computed using TBE originally converged from below the analytical stress value and in the third refinement switched to converging from above. This fortuitous reduction in error in one refinement spoils the appearance of the expected “linear” convergence behavior. (As pointed out by one of the referees, this phenomenon could perhaps be also explained by the meshes not being nested.) Nevertheless, the improvement of TBE stresses over MSOE stresses is clearly visible. We also observe that the TBE stresses in the tetrahedral element case are of equivalent accuracy to that of the Abaqus improved-stresses (C3D10HS element stresses), and in the hexahedral element case, the TBE stresses are improved over the Abaqus C3D8HS element improved-stresses.

The coarsest hexahedral mesh used for the refinement study is shown in Figure 3.16b.

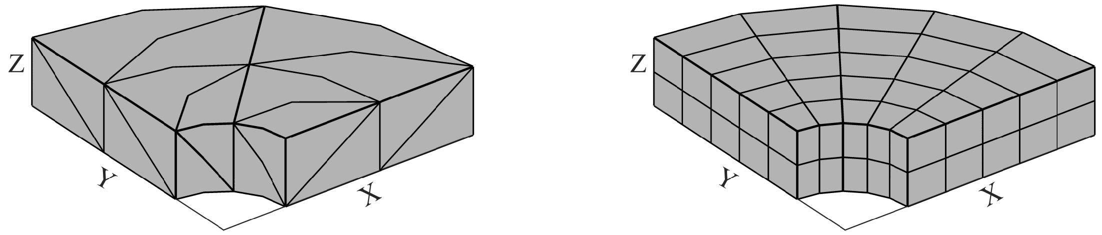

(a) (b)

Figure 3.16: Hole in a slab, Coarsest meshes used for mesh refinement study (a) Quadratic Tetrahedral elements (b) Hexahedral elements

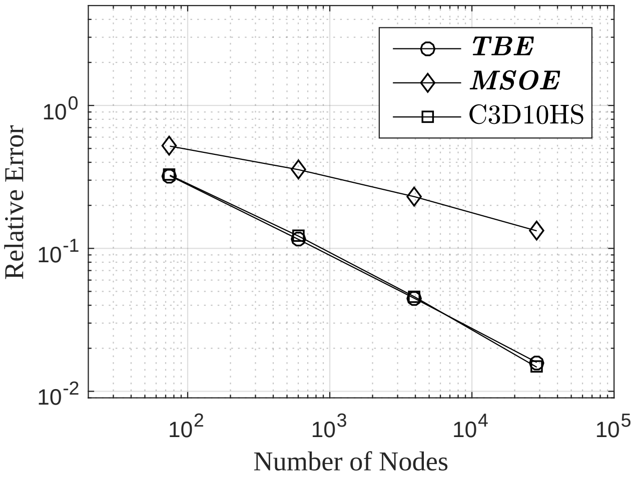

Figure 3.17: Hole in a slab, quadratic tetrahedral elements. Error of σ_{xx} at Point B.

The mesh refinement study of relative errors performed using hexahedral elements is shown in Figure 3.19 for σ_{xx} at Point B. The stress value at Point B is obtained by averaging along the edge containing Point B parallel to Z-axis. The TBE, MSOE and the stresses obtained using Abaqus C3D8HS elements are considered for the study. For hexahedral elements, Abaqus C3D8HS elements have similar features as those of Abaqus C3D10HS quadratic tetrahedral elements. Figure 3.20 shows errors in the average of normal stress σ_{yy}, computed along the edge containing Point A. At the moment we do not have an explanation for the impressive convergence rate of the mean-strain hexahedron H8MSGSO with the TBE procedure.

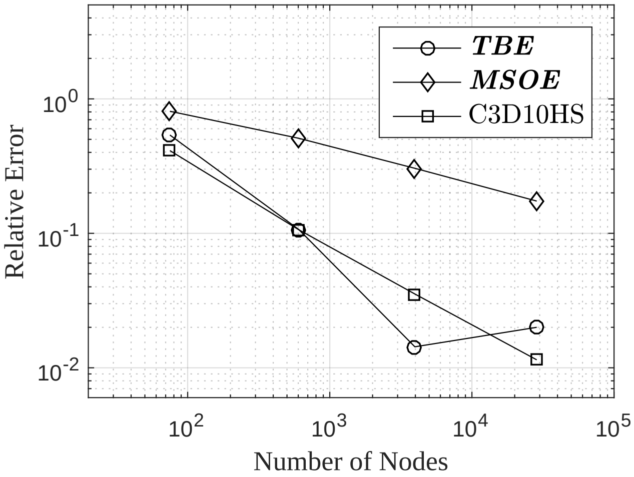

Figure 3.18: Hole in a slab, quadratic tetrahedral elements. Error of σ_{yy} at Point A.

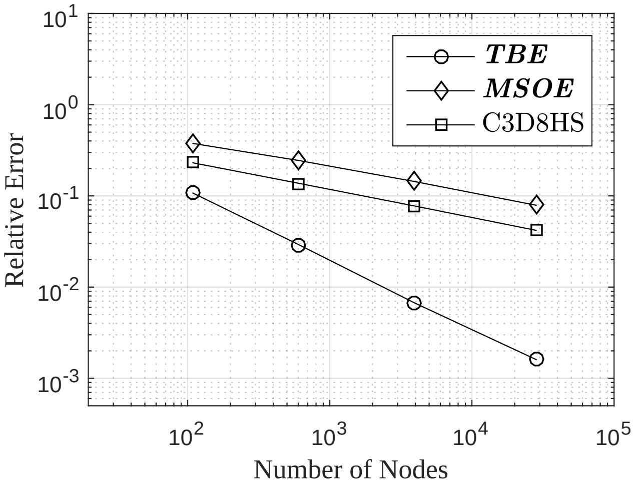

Figure 3.19: Hole in a slab ($\nu = 0.49995$), hexahedral elements. Error of σ_{xx} at Point B.

3.2.4 Thin Cantilever Beam

This example considers a thin beam (25m×0.5m×0.5m) fixed at one end, and shear loaded by $P = 100$ Pa at the other end in the downward direction (Figure 3.21). The Young's modulus is 100 Pa, and the Poisson's ratios 0.3. The mesh is built by dividing the beam into $100 \times 2 \times 2$ hexahedra to create a hexahedral mesh, and each hexahedron is subdivided into tetrahedra to create a quadratic tetrahedral mesh. The normal stresses σ_{xx} are investigated on a vertical fiber located at 8.25m along the length of front face of the beam. The elemental

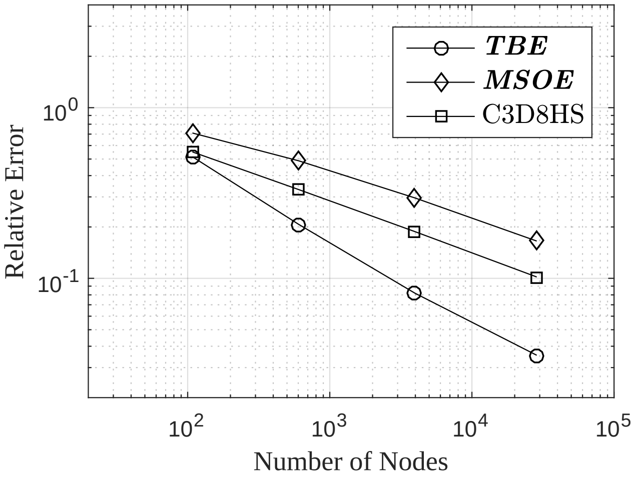

Figure 3.20: Hole in a slab ($\nu = 0.49995$), hexahedral elements. Error of σ_{yy} at Point *A*.

contributions of the TBE stresses to the nodes on the fiber and the nodal stresses computed by simple averaging are considered.

Figure 3.21: Cantilever Beam - Loads and Boundary Conditions

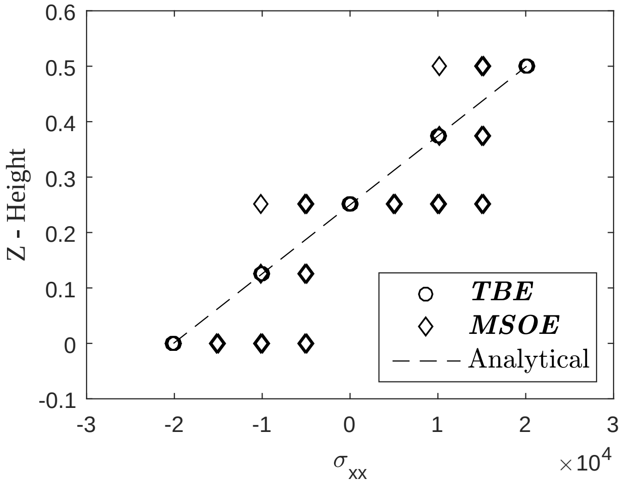

Figure 3.22: Thin Cantilever Beam, compressible material ($\nu = 0.3$). Quadratic tetrahedral elements. Element Contributions of σ_{xx} to the nodes on a vertical fiber at $x = 8.25$m of the beam.

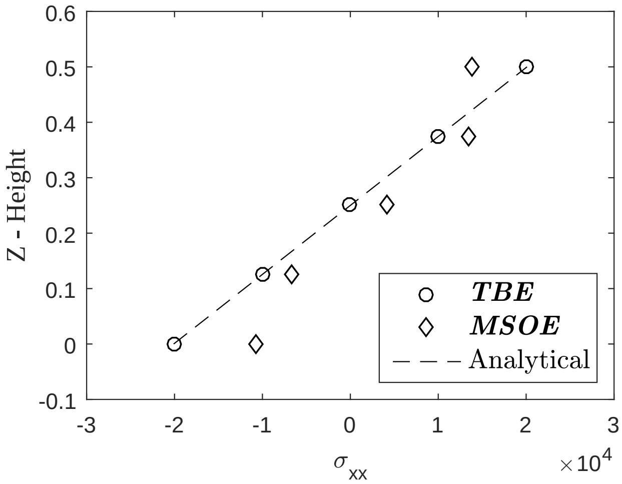

Figure 3.23: Thin Cantilever Beam, compressible material ($\nu = 0.3$). Quadratic tetrahedral elements. Stress σ_{xx} at the nodes obtained by averaging, on a vertical fiber at $x = 8.25$m of the beam.

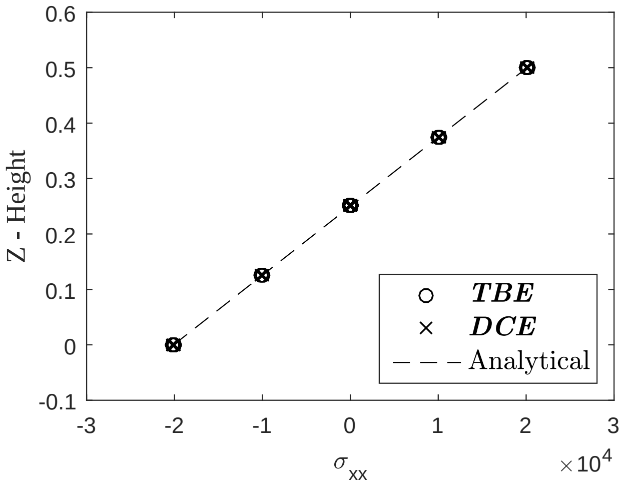

Figure 3.24: Thin Cantilever Beam, compressible material ($\nu = 0.3$). Quadratic tetrahedral elements. Element Contributions of σ_{xx} to the nodes on a vertical fiber at $x = 8.25$m of the beam.

Figure 3.22 shows the elemental contributions of σ_{xx} to the nodes on the fiber of interest and Figure 3.23 shows the stress distribution after averaging the elemental contributions of stresses at nodes in a quadratic tetrahedral mesh. We can observe that the TBE stresses result in improved stress prediction as compared to the MSOE stresses. The TBE stresses agree very well with the analytical solution unlike the element-wise constant MSOE stresses both before and

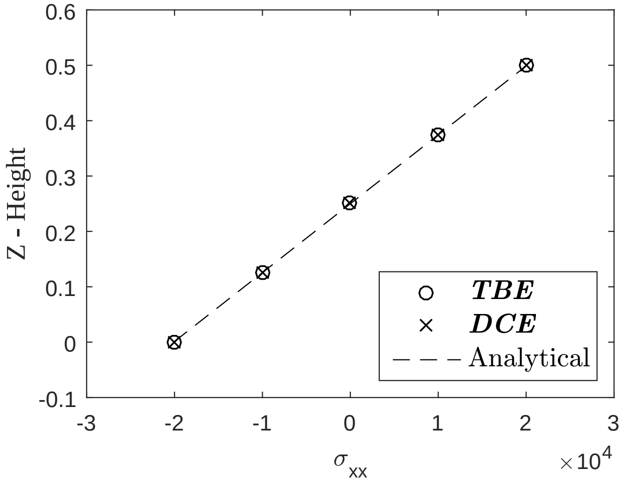

Figure 3.25: Thin Cantilever Beam, compressible material ($\nu = 0.3$). Quadratic tetrahedral elements. Stress σ_{xx} at the nodes obtained by averaging, on a vertical fiber at $x = 8.25$m of the beam.

after averaging of the elemental contributions of stresses at the nodes. The directly-computed stresses (DCE) are expected to exhibit similar behavior as that of the TBE stresses, since the elements have good aspect ratios and the material is compressible. Figures 3.24 and 3.25 show the distribution of TBE and DCE stresses in comparison with the analytical solution, before and after averaging the elemental contributions of stresses at the nodes respectively. As expected, the stress distributions match very well and also match exactly with the analytical solution. This example clearly demonstrates the improvement of TBE stresses over the MSOE stresses in quadratic tetrahedral elements for compressible materials.

Figures 3.26 and 3.27 show the distribution of TBE and MSOE stresses in comparison with the analytical solution, before and after averaging the elemental contributions of stresses at the nodes respectively for a hexahedral mesh in compressible material case. The plots clearly indicate improvement in stress quality using the TBE stresses over the MSOE stresses. Figures 3.28 and 3.29 show the distribution of TBE and DCE stresses before and after averaging the elemental contributions of σ_{xx} at the nodes respectively. The errors in stress distributions of DCE and TBE stresses are observed to be approximately the same.

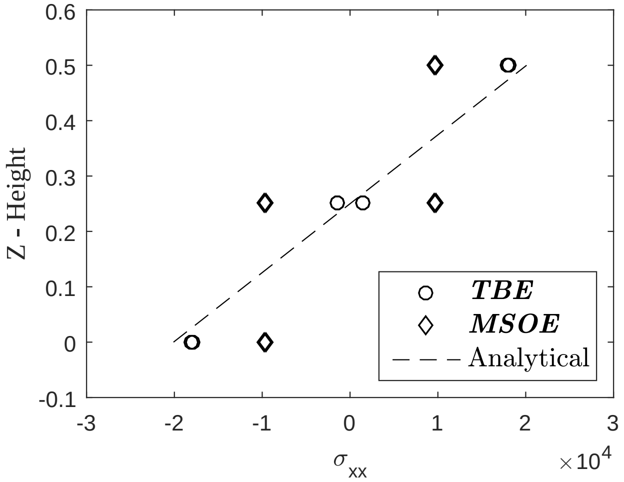

Figure 3.26: Thin Cantilever Beam, compressible material ($\nu = 0.3$). Hexahedral elements. Element contributions of σ_{xx} to the nodes on a vertical fiber at $x = 8.25$m of the beam.

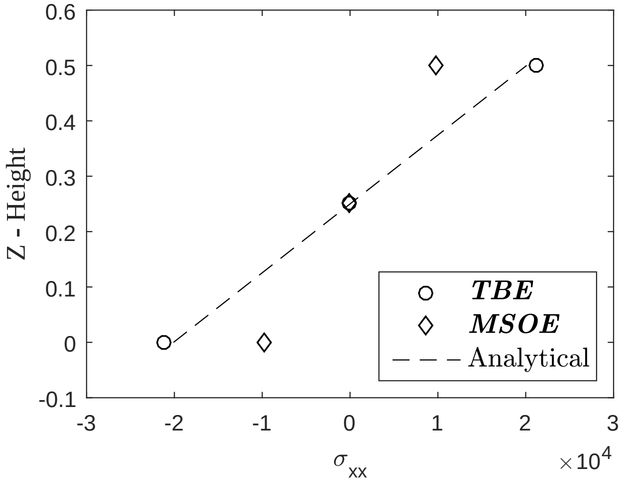

Figure 3.27: Thin Cantilever Beam, compressible material ($\nu = 0.3$). Hexahedral elements. Stress σ_{xx} at the nodes obtained by averaging, on a vertical fiber at $x = 8.25$m of the beam.

Now, consider the stresses in the beam when the material is nearly-incompressible ($\nu = 0.4999$). The hexahedral elements cannot produce a locking-free displacement, so the stresses are obviously erroneous (Figures 3.36 and 3.37). For T10 elements, the displacements are of good quality owing to the use of quadratic shape functions. However, the stresses are noisy as shown in Figures 3.32 and 3.33.

Figure 3.30 shows the elemental contributions of σ_{xx} to the nodes on the fiber of interest

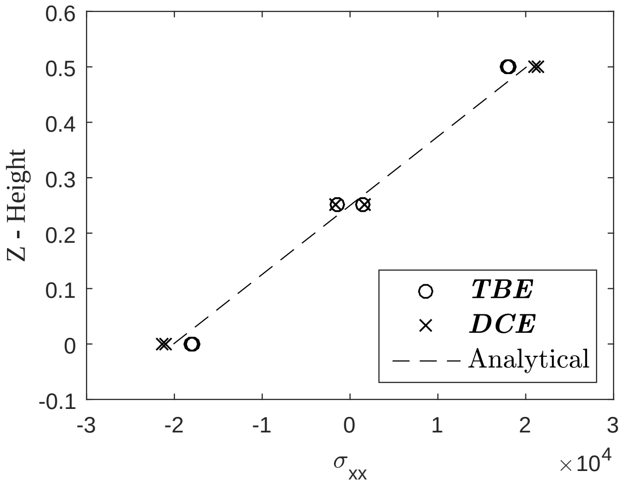

Figure 3.28: Thin Cantilever Beam, compressible material ($\nu = 0.3$). Hexahedral elements. Element Contributions of σ_{xx} to the nodes on a vertical fiber at $x = 8.25$m of the beam.

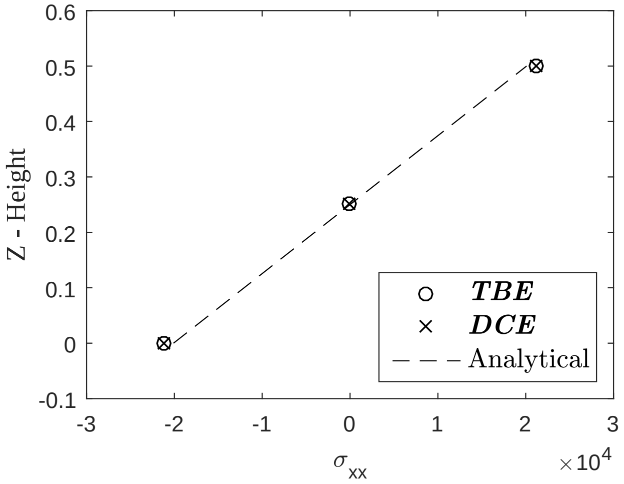

Figure 3.29: Thin Cantilever Beam, compressible material ($\nu = 0.3$). Hexahedral elements. Stress σ_{xx} at the nodes obtained by averaging, on a vertical fiber at $x = 8.25$m of the beam.

and Figure 3.31 shows the stress distribution after averaging the elemental contributions of stresses at nodes in a quadratic tetrahedral mesh. We can observe that the TBE stresses result in greatly improved stress prediction as compared to the MSOE stresses. The TBE stresses agree very well with the analytical solution unlike the element-wise constant MSOE stresses both before and after averaging of the elemental contributions of stresses at the nodes. The directly-computed stresses (DCE) are very much erroneous because of noisy stresses by T10 elements in near-incompressible

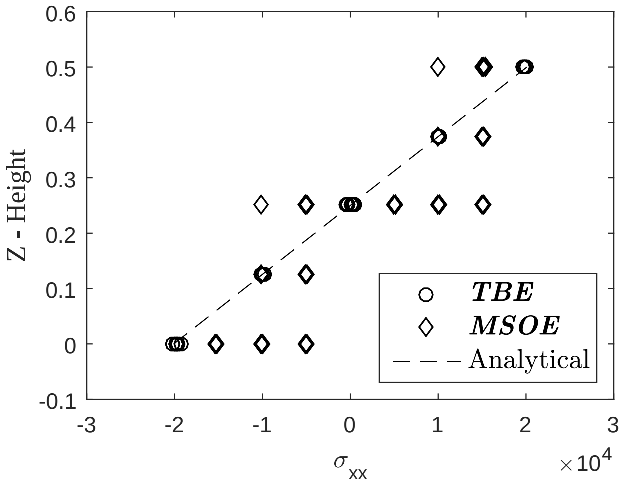

Figure 3.30: Thin Cantilever Beam, near-compressible material ($\nu = 0.4999$). Quadratic tetrahedral elements. Element Contributions of σ_{xx} to the nodes on a vertical fiber at $x = 8.25$m of the beam.

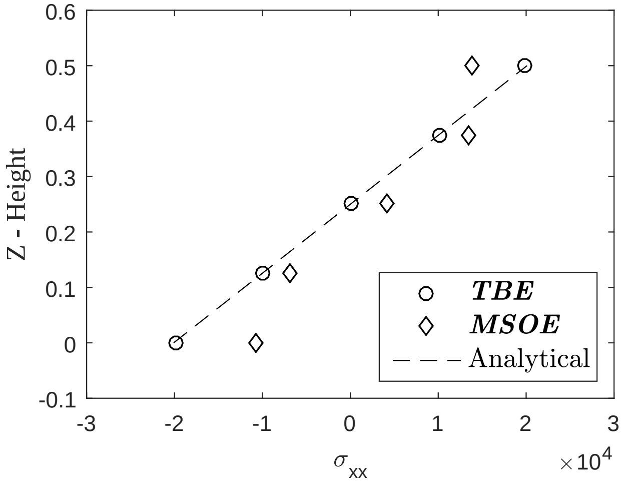

Figure 3.31: Thin Cantilever Beam, near-compressible material ($\nu = 0.4999$). Quadratic tetrahedral elements. Stress σ_{xx} at the nodes obtained by averaging, on a vertical fiber at $x = 8.25$m of the beam.

applications. Figures 3.32 and 3.33 show the distribution of TBE and DCE stresses in comparison with the analytical solution, before and after averaging the elemental contributions of stresses at the nodes respectively. As expected, the TBE stresses match well with the analytical solution. This example clearly demonstrates the improvement of TBE stresses over the MSOE stresses in quadratic tetrahedral elements for near-compressible materials.

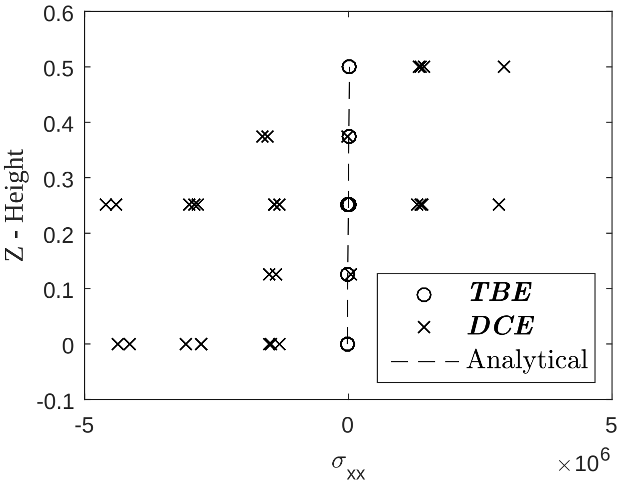

Figure 3.32: Thin Cantilever Beam, near-compressible material ($\nu = 0.4999$). Quadratic tetrahedral elements. Element Contributions of σ_{xx} to the nodes on a vertical fiber at $x = 8.25$m of the beam.

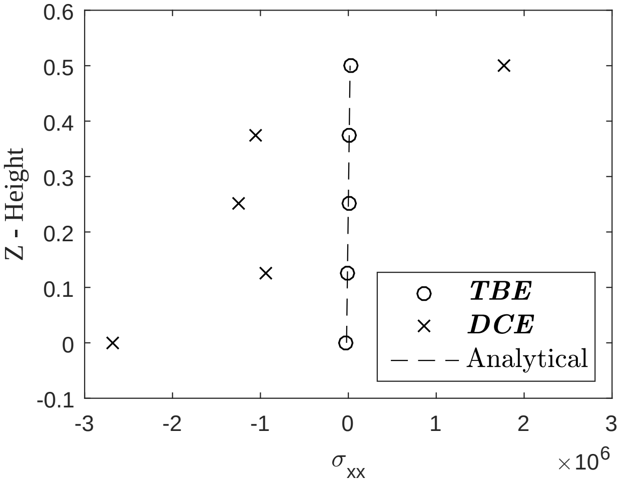

Figure 3.33: Thin Cantilever Beam, near-compressible material ($\nu = 0.4999$). Quadratic tetrahedral elements. Stress σ_{xx} at the nodes obtained by averaging, on a vertical fiber at $x = 8.25$m of the beam.

Figures 3.34 and 3.35 show the distribution of TBE and MSOE stresses in comparison with the analytical solution, before and after averaging the elemental contributions of stresses at the nodes respectively for a hexahedral mesh in compressible material case. The plots clearly indicate improvement in stress quality using the TBE stresses over the MSOE stresses. Figures 3.36 and 3.37 show the distribution of TBE and DCE stresses before and after averaging the

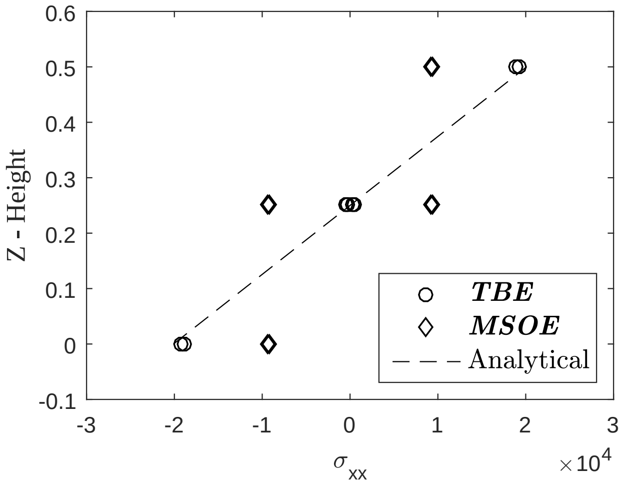

Figure 3.34: Thin Cantilever Beam, near-compressible material ($\nu = 0.4999$). Hexahedral elements. Element contributions of σ_{xx} to the nodes on a vertical fiber at $x = 8.25$m of the beam.

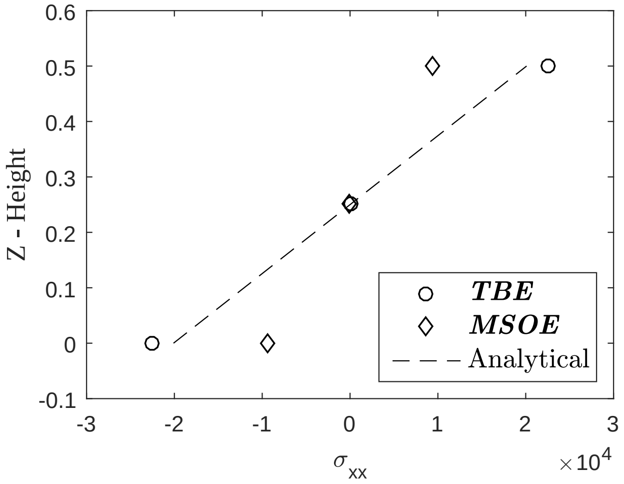

Figure 3.35: Thin Cantilever Beam, near-compressible material ($\nu = 0.4999$). Hexahedral elements. Stress σ_{xx} at the nodes obtained by averaging, on a vertical fiber at $x = 8.25$m of the beam.

elemental contributions of σ_{xx} at the nodes respectively. The DCE stresses are completely off, as expected, while the TBE stresses match well with the analytical solution.

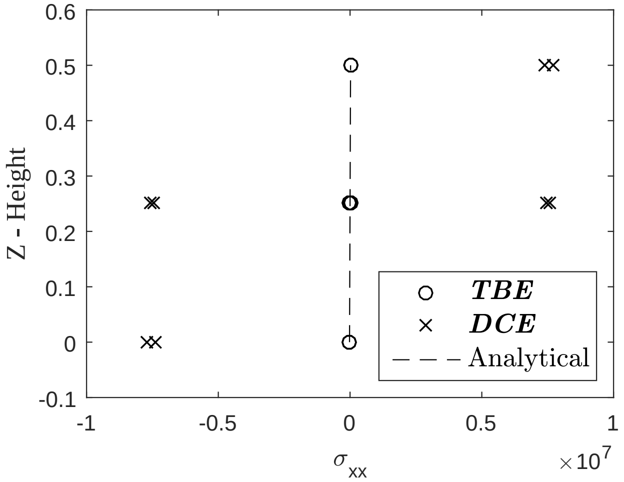

Figure 3.36: Thin Cantilever Beam, near-compressible material ($\nu = 0.4999$). Hexahedral elements. Element Contributions of σ_{xx} to the nodes on a vertical fiber at $x = 8.25$m of the beam.

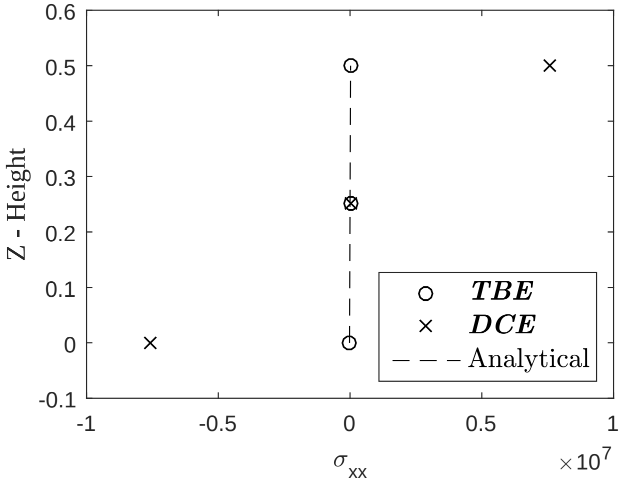

Figure 3.37: Thin Cantilever Beam, near-compressible material ($\nu = 0.4999$). Hexahedral elements. Stress σ_{xx} at the nodes obtained by averaging, on a vertical fiber at $x = 8.25$m of the beam.

3.2.5 Cube of orthotropic material under prescribed displacements

In this example, the goal is to investigate the performance of the proposed method for structures with orthotropic material properties. The domain is a cube of 0.1 m on the side. Displacements are prescribed on the entire surface of the cube: Table 3.1 lists the coefficients of polynomial expression for the three displacement components.

Table 3.1: Expression for the displacement components on the surface in terms of a full quadratic polynomial in x, y, z. The coefficients in the table need to be multiplied with 10^{-3}.

Displacement	1	x	y	z	xy	xz	yz	x^2	y^2	z^2
u_x	0.0	1.0	0.0	1.0	0.0	-1.0	0.0	2.0	0.0	1.0
u_y	0.0	0.0	0.3	0.0	3.0	-2.0	7.0	0.0	8.0	-7.0
u_z	0.0	0.0	0.0	0.7	8.0	3.0	-15.0	2.0	-3.0	0.1

The material is a fibrous composite, with $E_X = 2.5 \times 10^6$ psi, $E_Y = E_Z = 1.0 \times 10^6$ psi, $G_{XY} = G_{XZ} = 0.5 \times 10^6$ psi, $G_{YZ} = 0.2 \times 10^6$ psi, $\nu_{XY} = \nu_{XZ} = \nu_{YZ} = 0.25$, where X signifies the direction parallel to the fibers, Y the transverse direction, and ν_{XY} is the Poisson's ratio measuring strain in the transverse direction under uniaxial normal stress in the longitudinal direction. The orientation of the material with respect to the global Cartesian axes is defined by rotation of -15^o about the global Y axis. The output stresses are computed in the global Cartesian coordinate system.

We consider meshes which are obtained by uniform bisection refinement from the coarsest mesh of $3 \times 3 \times 3$ elements along the side. The quadratic tetrahedral meshes are obtained by dividing each hexahedron of the hexahedral meshes into 6 tetrahedra.

In this study we consider convergence in the RMS error of the stress (3.6). The hexahedral elements converge in the RMS stress error with a convergence rate of approximately 1.18 (standard hexahedral elements H8) and 1.18 (MSOE). The present mean-strain TBE delivers a slightly higher rate of 1.24: call for Figure 3.39. The standard tetrahedral elements T10 yield a convergence rate of about 1.32, whereas the MSOE stresses converge at the rate of 1.3; the TBE stresses converge at the rate of 1.48, even though they are not the most accurate for the initial coarse mesh; call for Figure 3.38. At the moment the reason for the quadratic tetrahedral elements with TBE (and the standard T10E) not realizing the theoretical convergence rate for the stresses is unknown.

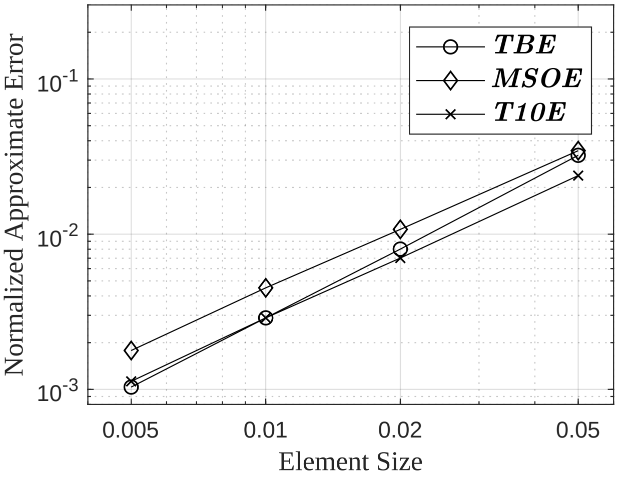

Figure 3.38: Orthotropic material cube - Convergence of normalized approximate error in stress (Tetrahedral elements)

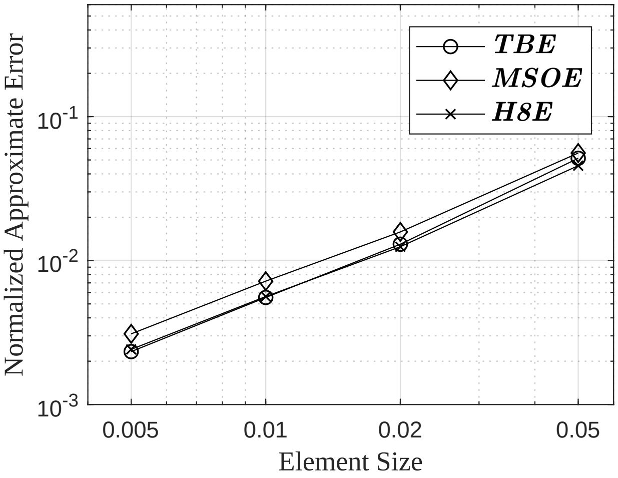

Figure 3.39: Orthotropic material cube - Convergence of normalized approximate error in stress (Hexahedral elements)

3.2.6 Meyer-Piening Sandwich Plate

This example compares the trend-based stresses and mean stresses in the Meyer-Piening Sandwich plate [43]. The beam has three layers: The top and bottom faces are thinner (0.5 mm and 0.1 mm respectively) than the central core (11.4 mm). The composite beam has very different geometric and constitutive properties between core and the faces. The material properties of the faces and core of the sandwich are given in Table 3.2. This example has strong heterogeneities and is not frequently addressed in literature [44]. A localized pressure loading is applied on a rectangular area (5 mm×20 mm) at the center of the beam. Due to symmetry, only one quarter of the beam (50 mm×100 mm) is used for analysis, as shown in Figure 3.40. $A_1B_1C_1D_1$ ($z = 12$ mm) is the top surface of the top face on which the rectangular area of pressure loading is located. The surfaces $A_2B_2C_2D_2$ ($z = 11.9$ mm), $A_3B_3C_3D_3$ ($z = 0.5$ mm) and $A_4B_4C_4D_4$ ($z = 0$ mm) are the top surface of the core, top and bottom surfaces of the bottom face respectively.

The Y-displacements are constrained on surface $A_1A_4B_4B_1$, and X-displacements are constrained on surface $B_1B_4C_4C_1$. The surfaces $A_1A_4D_4D_1$ and $D_1D_4C_4C_1$ are constrained to move only in the XY plane. We analyze the stress quality at Point A_1. The trend-based and mean stresses are compared for both QT10MS and H8MSGSO elements.

Figures 3.41 and 3.42 show the errors in stresses σ_{xx} and σ_{yy} respectively at Point A_1 for quadratic tetrahedral meshes using trend-based stresses, mean stresses and ABAQUS C3D10HS elements. The analytical stresses at A_1 are $< \sigma_{xx}, \sigma_{yy} > = < -624, -241 >$ MPa [43]. The plots indicate an improvement of the trend-based stresses over the mean stresses. Point A_1 belongs to the top face of the composite and is very thin. The normal stress gradients in this layer are very high [43]. Since mean stresses are the averaged stresses of an element, they may not be able to approximate the stresses well. The trend-based stresses predict better stress approximates since the stresses are based on the trend of stress distribution inside the elements. Moreover, we can see that the trend-based stresses converge faster than mean stresses for the same reason.

Figures 3.43 and 3.44 show the errors in stresses σ_{xx} and σyy respectively at Point A_1 for hexahedral meshes using trend-based stresses, mean stresses, ABAQUS C3D8S, C3D8R(enh) and C3D8I elements. We observed a small improvement of trend-based stresses over the mean stresses for σ_{xx} and σ_{yy}, and negligible improvement for σ_{xy}. As discussed above, the normal stresses σ_{xx} and σ_{yy} vary rapidly in the top face of the composite, leading to poorer approximation of mean stresses as compared to the trend-based stresses. Due to the very thin elements in the top face, the form factor of the elements is low, which could potentially decrease the improvement of trend-based stresses over mean stresses.

Table 3.2: Material properties of the Meyer-Piening Sandwich Beam

Faces	Core
$E_1 = 70\text{GPa}$, $E_2 = 71\text{GPa}$ $E_3 = 69\text{GPa}$ $G_{12} = G_{13} = G_{23} = 26\text{GPa}$ $\nu_{12} = \nu_{13} = \nu_{23} = 0.3$	$E_1 = E_2 = 3\text{MPa}$ $E_3 = 2.8\text{MPa}$ $G_{12} = G_{13} = G_{23} = 1.0\text{MPa}$ $\nu_{12} = \nu_{13} = \nu_{23} = 0.25$

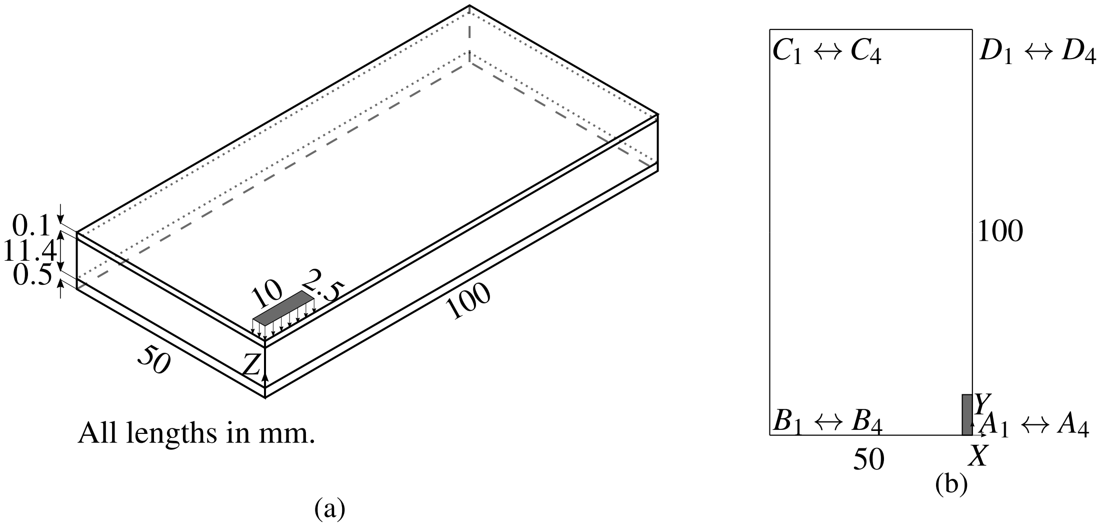

(a)

(b)

Figure 3.40: Quarter model of Meyer-Piening Sandwich Beam. (a) 3-D view (b) Top view.

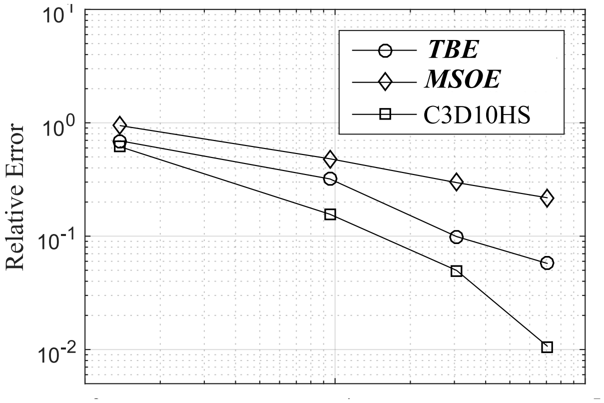

Figure 3.41: Meyer-Piening Sandwich - Errors in σ_{xx} at Point A_1 with mesh refinement (Tetrahedral elements)

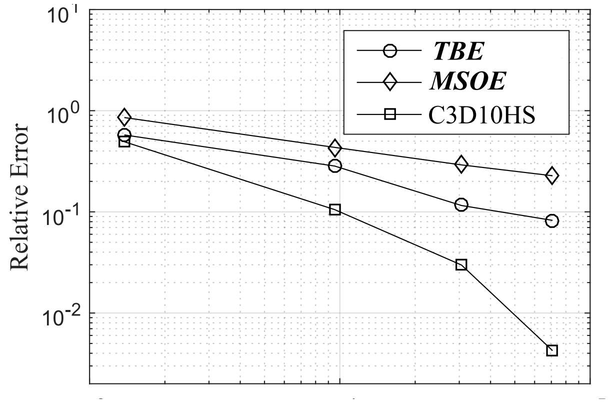

Figure 3.42: Meyer-Piening Sandwich - Errors in σ_{yy} at Point A_1 with mesh refinement (Tetrahedral elements)

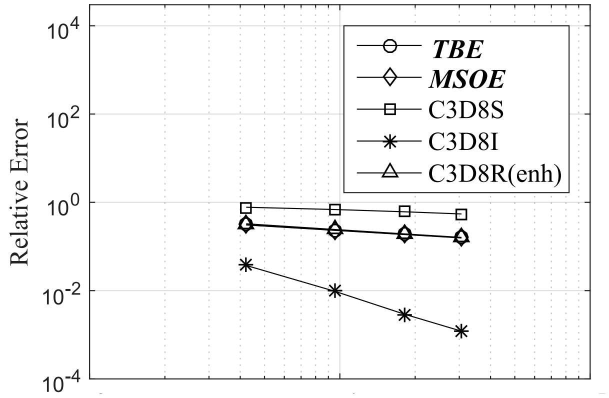

Figure 3.43: Meyer-Piening Sandwich - Errors in σ_{xx} at Point A_1 with mesh refinement (Hexahedral elements)

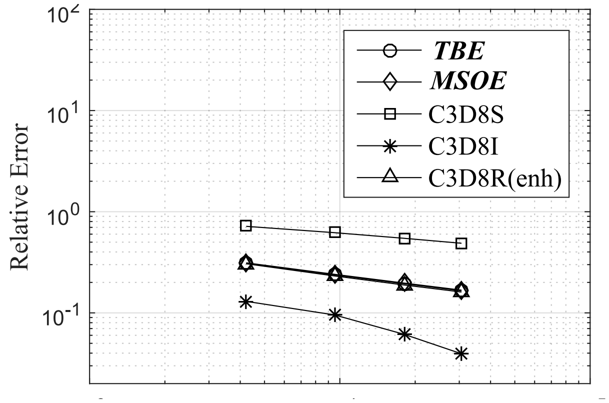

Figure 3.44: Meyer-Piening Sandwich - Errors in σ_{yy} at Point A_1 with mesh refinement (Hexahedral elements)

The trend-based stress estimate thus obtains an optimally convergent and noise-free stress field for the stabilized mean-strain finite elements. The examples with nearly-incompressible materials show that the obtained stresses are noise-free, and the extra terms (the terms after the mean stress) used in the stress field estimate improve the quality of stress approximation. The trend-based stress field is demonstrated to have an improved convergence over the mean stresses, at least in the QT10MS elements where the optimal convergence is of order 2. The examples show stress improvement over mean stresses in QT10MS and H8MSGSO elements. The stress field can also be used without any changes for improved approximation in nonlinear regime.

Chapter 3 has many details taken from the manuscript, “Sivapuram R, Krysl P. Improved Recovered Nodal Stress for Mean-Strain Finite Elements. *Finite Elements in Analysis and Design* 2018; **146**:70-83, doi:10.1016/j.finel.2018.04.005”, and the work is done in collaboration with Prof. Petr Krysl. The dissertation author is the primary investigator of the manuscript.

Chapter 4

Nodally Integrated Continuum Elements

Many complex structural analysis problems are solved by Finite Element Method (FEM) using linear tetrahedral and hexahedral elements. Tetrahedral elements are usually preferred because of the easy and reliable meshing methods available. The hexahedral elements are used when more accuracy is required since they use trilinear basis functions. These low-order elements severely suffer from volumetric locking when a (nearly) incompressible material is involved in the analysis (de Souza Neto et al [45]). Methods involving selective reduced integration of stiffness matrices and B-bar techniques were developed to avoid volumetric locking (Hughes [18, 14]). Additionally, lower order elements are also known to exhibit shear locking: the excessive numerical bending stiffness which limits the ability of finite elements with bad aspect ratios to accurately represent bending deformations (Prathap et al[19]). Some methods use incompatible modes and assumed strains to deal with this numerical defect (Simo et al [46]).

A range of assumed strain elements have been developed by Krysl and collaborators in [47, 20, 48, 21, 29, 24, 30]. The assumed strain is derived using the weak form of the difference between assumed and real strains which are defined using kinematic compatibility. The assumed strain energy is computed using mean strains to eliminate volumetric locking. To prevent the appearance of the hourglass modes caused by the rank-deficient mean strain-based stiffness matrix, a couple of stabilization terms are added, where one term uses full integration and the other uses reduced integration. Krysl and collaborators [20, 21, 24] designed a compressible stabilization material to generate the added stabilization terms for hexahedral, composite-tetrahedral and quadratic tetrahedral elements. The stabilization material is also chosen such that the incorporation of fully-integrated stabilization term does not introduce shear locking into the model using optimal or quasi-optimal energy-sampling stabilization. Sivapuram et al [30] proposed a nodal stress field for these energy-sampling stabilized assumed (mean) strain finite elements and demonstrated theoretical convergence rates.

Nodal integration helps in achieving a favorable constraint ratio when dealing with (nearly) incompressible analyses, which eludes fully integrated elements. Dohrmann et al [49] proposed nodally integrated triangular and tetrahedral elements by constructing node-based constant-strain ”elements” and demonstrated superconvergence using some static analyses. Their work was extended to large deformation applications by Bonet et al [50]. The simplex nodally integrated elements were generalized to hexahedral shapes and higher order in Krysl and Zhu [51] using an assumed-strain technique derived using the a priori weak enforcement of kinematic compatibility. They demonstrated the convergence of linear and quadratic 2D and 3D Nodally Integrated Continuum Elements (NICE) for static problems, and also showed that the elements satisfy patch tests. Using a similar derivation, the Nodally Integrated Plate Elements (NIPE) were developed by Castellazzi and Krysl [52]. A modification to the original formulation was proposed to achieve robustness in case of highly distorted elements and slivers in Krysl et al [53, 54]. The nodally integrated elements have also been used in the context of static analysis for functionally graded plates (Castellazzi et al [55]) and in elastoplastic problems (Artioli et al [56]).

4.1 NICE Formulation

In this section, we briefly review the assumed deformation gradient formulation for the nodally integrated finite elements in context of linear elasticity from Krysl and Zhu [51] and the formulation with increased robustness for highly distorted elements from Krysl and Kagey [53]. This formulation is valid for many types of finite elements but this work focuses only on linear tetrahedral and trilinear hexahedral elements. We use the Voigt notation to represent the tensors in this work. Using nodal quadrature for integration when the structure is made of a nearly-incompressible ($\nu \to 0.5$) material results in favorable constraint-ratio (3 for 3D continuum linear elasticity). The formulation requires gradient operators at the integration points (here, nodes). The element-wise deformation gradient operators are multivalued at the nodes, at least when C^0 shape functions are used in the finite element analysis. An assumed-strain method is thus used to define an assumed nodal deformation gradient operator.

We start by considering the de Veubeke-Hu-Washizu functional [25]

$$\Pi(\overline{\varepsilon},\, \overline{\sigma},\, u) = \int_\Omega \mathcal{U}(\overline{\varepsilon})\, d\Omega + \int_\Omega \overline{\sigma} \cdot (\nabla^s u - \overline{\varepsilon})\, d\Omega - \mathcal{W} \tag{4.1}$$

where Ω is the structural domain, $\overline{\varepsilon}$ is the assumed strain, u is the displacement field, $\nabla^s(\cdot)$ is the symmetric gradient operator and $\mathcal{W}$ is the external work done on Ω. The first term in the potential energy Π signifies the deformation energy of the domain Ω and the second term involves a kinematic constraint with $\overline{\sigma}$ acting as the Lagrange multiplier field corresponding to the constraint. The second term enforces the kinematic constraint weakly, i.e., the assumed strain matches the symmetric gradient of displacement in a volume-averaged sense. The deformation energy (assumed strain energy) per unit volume of the structural domain Ω is given by

$$\mathcal{U}(\overline{\varepsilon}) = \frac{1}{2}\, \overline{\varepsilon} \cdot D \cdot \overline{\varepsilon} \tag{4.2}$$

where D signifies the material properties of the structure. Discretizing the structure Ω using a mesh of n_{el} elements and n_{nd} nodes and representing the fields discretely, the potential energy Equation 4.1 becomes

$$\Pi(\bar{\boldsymbol{\varepsilon}},\, \bar{\boldsymbol{\sigma}},\, \boldsymbol{u}) = \int_{\Omega} \frac{1}{2}\, \bar{\boldsymbol{\varepsilon}}^T \boldsymbol{D} \bar{\boldsymbol{\varepsilon}}\; d\Omega + \int_{\Omega} \bar{\boldsymbol{\sigma}}^T \left(\mathcal{B}\boldsymbol{u} - \bar{\boldsymbol{\varepsilon}}\right)\, d\Omega - \mathcal{W} \tag{4.3}$$

where $\mathcal{B}$ is the deformation gradient operator which is the discretized version of the symmetric gradient operator and all the bolded vectors and matrices correspond to their respective unbolded field variables. A stable equilibrium of the structure is obtained by finding the stationary point of the potential energy Equation 4.3. Variations of the discretized potential energy Equation 4.3 with respect to the three variables vanish as follows.

$$\begin{aligned}
\partial_{\boldsymbol{u}}\Pi(\bar{\boldsymbol{\varepsilon}},\, \bar{\boldsymbol{\sigma}},\, \boldsymbol{u})\cdot\delta\boldsymbol{u} &= \int_{\Omega} \bar{\boldsymbol{\sigma}}^T \mathcal{B}\delta\boldsymbol{u}\; d\Omega - \partial_{\boldsymbol{u}}\mathcal{W}\cdot\delta\boldsymbol{u} = 0\\
\partial_{\bar{\boldsymbol{\varepsilon}}}\Pi(\bar{\boldsymbol{\varepsilon}},\, \bar{\boldsymbol{\sigma}},\, \boldsymbol{u})\cdot\delta\bar{\boldsymbol{\varepsilon}} &= \int_{\Omega} \left(\boldsymbol{D}\bar{\boldsymbol{\varepsilon}} - \bar{\boldsymbol{\sigma}}\right)^T \delta\bar{\boldsymbol{\varepsilon}}\; d\Omega = 0\\
\partial_{\bar{\boldsymbol{\sigma}}}\Pi(\bar{\boldsymbol{\varepsilon}},\, \bar{\boldsymbol{\sigma}},\, \boldsymbol{u})\cdot\delta\bar{\boldsymbol{\sigma}} &= \int_{\Omega} \delta\bar{\boldsymbol{\sigma}}^T \left(\mathcal{B}\boldsymbol{u} - \bar{\boldsymbol{\varepsilon}}\right)\, d\Omega = 0
\end{aligned} \tag{4.4}$$

where the first equation indicates the balance of the external work done performed on a structural displacement $\delta\boldsymbol{u}$ and the deformation energy stored, the second equation yields a definition for the Lagrange multiplier $\bar{\boldsymbol{\sigma}}$ in the units of stress,

$$\bar{\boldsymbol{\sigma}} = \boldsymbol{D}\bar{\boldsymbol{\varepsilon}} \tag{4.5}$$

The third equation in Equation 4.4 is used in deriving the assumed deformation gradient for the NICE formulation. The third equation in Equation 4.4 is modified by plugging in Equation 4.5 as

$$\int_{\Omega} \delta\bar{\boldsymbol{\varepsilon}}^T \boldsymbol{D}\left(\mathcal{B}\boldsymbol{u} - \bar{\boldsymbol{\varepsilon}}\right)\, d\Omega = 0 \tag{4.6}$$

The assumed strain $\bar{\boldsymbol{\varepsilon}}$ is written in terms of the displacement $\boldsymbol{u}$ as

$$\bar{\boldsymbol{\varepsilon}} = \overline{\mathcal{B}}\boldsymbol{u} \tag{4.7}$$

where $\overline{\mathcal{B}}$ is the assumed deformation gradient operator. Substituting the expression for assumed strain Equation 4.7 in Equation 4.6, we get

$$\int_{\Omega} \left(\overline{\mathcal{B}}\delta\boldsymbol{u}\right)^T \boldsymbol{D}\left(\mathcal{B}\boldsymbol{u} - \overline{\mathcal{B}}\boldsymbol{u}\right)\, d\Omega = 0 \tag{4.8}$$

We introduce the finite element approximations for displacement and deformation gradient operator,

$$\boldsymbol{u} = \sum_{I=1}^{n_{nd}} N_I \boldsymbol{u}_I \qquad \overline{\mathcal{B}}\boldsymbol{u} = \sum_{I=1}^{n_{nd}} \overline{\boldsymbol{B}}_I \boldsymbol{u}_I \qquad \mathcal{B}\boldsymbol{u} = \sum_{I=1}^{n_{nd}} \boldsymbol{B}_I \boldsymbol{u}_I \tag{4.9}$$

where N_I is the shape function and $\boldsymbol{u}_I$ is the displacement vector at the I^{th} node, $\boldsymbol{B}_I$ is the strain-displacement operator defined for node I, $\overline{\boldsymbol{B}}_I$ is the assumed strain-displacement operator for node I that will be derived below. Using Equation 4.9 in Equation 4.8 yields

$$\sum_{I,J} \delta\boldsymbol{u}_I^T \cdot \int_{\Omega} \overline{\boldsymbol{B}}_I^T \boldsymbol{D}\left(\boldsymbol{B}_J - \overline{\boldsymbol{B}}_J\right)\, d\Omega \cdot \boldsymbol{u}_J = 0 \tag{4.10}$$

This equation holds true for arbitrary virtual displacements $\delta\boldsymbol{u}_I$. Using this arbitrariness and assuming that the assumed nodal strain-displacement operator is independent of the displacements $\boldsymbol{u}_J$, we convert Equation 4.10 to the requirement

$$\int_{\Omega} \overline{\boldsymbol{B}}_I^T \boldsymbol{D}\left(\boldsymbol{B}_J - \overline{\boldsymbol{B}}_J\right)\, d\Omega = 0 \quad \forall\, I, J \tag{4.11}$$

The patch of elements connected to an arbitrary node I is pictorially shown in Figure 4.1 for triangular and quadrilateral elements. The element patches can similarly be defined for 3D elements. The assumed nodal strain-displacement operator $\overline{\boldsymbol{B}}_I$ is assumed to be constant and

(a) Triangular mesh (b) Quadrilateral mesh

Figure 4.1: Element patches corresponding to a node

non-zero over the element-patch corresponding to node I and zero elsewhere. This modifies Equation 4.11 to

$$\int_{\Omega} \overline{\boldsymbol{B}}_I^T \boldsymbol{D}\big(\boldsymbol{B}_J - \overline{\boldsymbol{B}}_J\big)\, d\Omega = 0 \quad \text{for any fixed } I \text{ and } J \in \texttt{nodes}(\texttt{elems}(I)) \tag{4.12}$$

where $\texttt{elems}(I)$ is the list of elements in the element-patch of node I and $\texttt{nodes}(e)$ is the list of nodes connected by element e. Writing the integral as sum over all the finite element domains, Equation 4.12 becomes

$$\sum_{e \in \texttt{elems}(I)} \int_{\Omega_e} \overline{\boldsymbol{B}}_I^T \boldsymbol{D}\big(\boldsymbol{B}_{eJ} - \overline{\boldsymbol{B}}_J\big)\, d\Omega = 0 \quad \text{for any fixed } I \text{ and } J \in \texttt{nodes}(\texttt{elems}(I)) \tag{4.13}$$

where Ω_e is the domain of finite element e and $\boldsymbol{B}_{eJ}$ is the nodal strain-displacement operator defined for node J in element e. An integral over finite element e can be approximated using nodal integration as

$$\int_{\Omega_e} (\cdot)(\boldsymbol{x})\, d\Omega = \sum_{K \,\in\, \texttt{nodes}(e)} (\cdot)\big|_{\boldsymbol{x}_K}\, \mathcal{J}_e\big|_{\boldsymbol{x}_K} w_e\big|_{\boldsymbol{x}_K} \tag{4.14}$$

where $\mathcal{J}_e\big|_{\boldsymbol{x}_K}$ is the Jacobian determinant of the Jacobian matrix $\boldsymbol{J}_e\big|_{\boldsymbol{x}_K}$ computed at the integration point (here, node) $\boldsymbol{x}_K$ of element e and $w_e\big|_{\boldsymbol{x}_K}$ is the corresponding weight. Using nodal integration Equation 4.14 in Equation 4.13 and assuming uniform material distribution in the structure Ω, we get

$$\sum_{e\in\texttt{elems}(I)}\sum_{K\in\texttt{nodes}(e)} \overline{\boldsymbol{B}}_I\big|_{\boldsymbol{x}_K}^T \boldsymbol{D}\Big(\boldsymbol{B}_{eJ}\big|_{\boldsymbol{x}_K} - \overline{\boldsymbol{B}}_J\big|_{\boldsymbol{x}_K}\Big)\ \mathcal{J}_e\big|_{\boldsymbol{x}_K} w_e\big|_{\boldsymbol{x}_K} = 0 \qquad (4.15)$$

$$\text{for any fixed } I \text{ and } J \in \texttt{nodes}(\texttt{elems}(I))$$

We are interested in solving for the assumed strain-displacement matrix corresponding to each node, so we rearrange the summations as

$$\sum_{K\in\texttt{nodes}(\texttt{elems}(I))}\sum_{e\in\texttt{elems}(K)} \overline{\boldsymbol{B}}_I\big|_{\boldsymbol{x}_K}^T \boldsymbol{D}\Big(\boldsymbol{B}_{eJ}\big|_{\boldsymbol{x}_K} - \overline{\boldsymbol{B}}_J\big|_{\boldsymbol{x}_K}\Big)\ \mathcal{J}_e\big|_{\boldsymbol{x}_K} w_e\big|_{\boldsymbol{x}_K} = 0 \qquad (4.16)$$

$$\text{for any fixed } I \text{ and } J \in \texttt{nodes}(\texttt{elems}(I))$$

For efficiency reasons, we make the integration points (nodes) K independent, and a solution to this equation then follows when each term in the first summation over the nodes vanishes as

$$\sum_{e\in\texttt{elems}(K)} \overline{\boldsymbol{B}}_I\big|_{\boldsymbol{x}_K}^T \boldsymbol{D}\Big(\boldsymbol{B}_{eJ}\big|_{\boldsymbol{x}_K} - \overline{\boldsymbol{B}}_J\big|_{\boldsymbol{x}_K}\Big)\ \mathcal{J}_e\big|_{\boldsymbol{x}_K} w_e\big|_{\boldsymbol{x}_K} = 0 \qquad (4.17)$$

$$\text{for any fixed } I, \text{ and } K, J \in \texttt{nodes}(\texttt{elems}(I))$$

The assumed nodal strain-displacement matrix $\overline{\boldsymbol{B}}_I\big|_{\boldsymbol{x}_K}$ is independent of index e, and $\boldsymbol{D}$ is assumed to be independent of K. Incorporating these assumptions, Equation (4.17) can be rewritten as

$$\overline{\boldsymbol{B}}_I\big|_{\boldsymbol{x}_K}^T \boldsymbol{D}\left[\sum_{e\in\texttt{elems}(K)} \boldsymbol{B}_{eJ}\big|_{\boldsymbol{x}_K}\ \mathcal{J}_e\big|_{\boldsymbol{x}_K} w_e\big|_{\boldsymbol{x}_K} - \overline{\boldsymbol{B}}_J\big|_{\boldsymbol{x}_K} \sum_{e\in\texttt{elems}(K)} \mathcal{J}_e\big|_{\boldsymbol{x}_K} w_e\big|_{\boldsymbol{x}_K}\right] = 0 \qquad (4.18)$$

$$\text{for any fixed } I, \text{ and } K, J \in \texttt{nodes}(\texttt{elems}(I))$$

Equation Equation 4.18 can be satisfied by nullifying the term in square brackets. This gives the expression for the assumed nodal strain-displacement matrix for node J at quadrature point K,

$$\overline{\boldsymbol{B}}_J\Big|_{\boldsymbol{x}_K} = \frac{\sum\limits_{e\in\mathtt{elems}(K)} \boldsymbol{B}_{eJ}\Big|_{\boldsymbol{x}_K} \mathcal{J}_e\Big|_{\boldsymbol{x}_K} w_e\Big|_{\boldsymbol{x}_K}}{\sum\limits_{e\in\mathtt{elems}(K)} \mathcal{J}_e\Big|_{\boldsymbol{x}_K} w_e\Big|_{\boldsymbol{x}_K}} \tag{4.19}$$

We can observe that the assumed nodal strain-displacement matrix for a node is given by the nodal averaging of the element-wise strain-displacement matrices. For the case of linear tetrahedral elements, this formulation simplifies to the nodally integrated tetrahedral (UT4) elements. For details, refer to [49, 57] where the theoretical convergence of the nodally integrated tetrahedral elements was shown. The theoretical convergence of general nodally integrated elements using our formulation can be easily developed extending Puso and Solberg [57].

We can readily observe that the nonzero structure of the assumed nodal strain-displacement matrix is the same as that of the element-based strain-displacement matrices, which are constructed using the shape function gradients. This indicates that instead of the assumed strain-displacement matrices, we can use the prescription for nodal averaging to compute the assumed nodal shape function gradients for J at quadrature point K as

$$\overline{\nabla N_J}\Big|_{\boldsymbol{x}_K} = \frac{\sum\limits_{e\in\mathtt{elems}(K)} \nabla N_{eJ}\Big|_{\boldsymbol{x}_K} \mathcal{J}_e\Big|_{\boldsymbol{x}_K} w_e\Big|_{\boldsymbol{x}_K}}{\sum\limits_{e\in\mathtt{elems}(K)} \mathcal{J}_e\Big|_{\boldsymbol{x}_K} w_e\Big|_{\boldsymbol{x}_K}} \tag{4.20}$$

where $N_{eJ}\Big|_{x_K}$ is the shape function defined in element e for node J at quadrature point K, $\overline{\nabla N_J}\Big|_{x_K}$ is the assumed nodal shape function gradient defined for node J at quadrature point K. In order for the formulation effectively deal with near-to-zero volume thin elements and slivers, Krysl and Kagey [53] proposed a modification to Equation 4.20. The element-based shape function gradients can be written in terms of shape function gradients in the parametric domain and the

Jacobian matrix of the element, as

$$\nabla N_{eJ}\big|_{x_K} = \nabla_{\boldsymbol{\xi}} N_{eJ}\big|_{\boldsymbol{\xi}(x_K)} \cdot J_e^{-1}\big|_{x_K} \tag{4.21}$$

where $\boldsymbol{\xi}(\cdot)$ refers to the parametric coordinate. The element-based shape function gradients in Equation 4.21 involve an inversion of the Jacobian matrix. In case of thin near-to-zero volume elements and slivers, $\mathcal{J}_e\big|_{x_K} \to 0$. This causes ill-conditioning of the inverse of the Jacobian matrix and hence causes loss of accuracy of the assumed nodal shape function gradients. This drawback is avoided by using the definition of the inverse of the Jacobian matrix,

$$J_e^{-1}\big|_{x_K} = \frac{1}{\mathcal{J}_e\big|_{x_K}}\ \mathtt{adj}\left(J_e\big|_{x_K}\right) \tag{4.22}$$

in terms of the adjugate matrix, where $\mathtt{adj}(\cdot)$ is the adjugate operator of a matrix. Using Equation 4.22, we reformulate Equation 4.20 as

$$\overline{\nabla N}_J\big|_{\boldsymbol{x}_K} = \frac{\sum\limits_{e\in\mathtt{elems}(K)} \nabla_{\boldsymbol{\xi}} N_{eJ}\big|_{\boldsymbol{\xi}(x_K)} \cdot \mathtt{adj}\left(\boldsymbol{J}_e\big|_{\boldsymbol{x}_K}\right) w_e\big|_{\boldsymbol{x}_K}}{\sum\limits_{e\in\mathtt{elems}(K)} \mathcal{J}_e\big|_{\boldsymbol{x}_K} w_e\big|_{\boldsymbol{x}_K}} \tag{4.23}$$

With division by the Jacobian determinant eliminated, the formulation can efficiently deal with extremely thin elements and slivers as demonstrated in Krysl and Kagey [53]. This nodally integrated finite element formulation is referred to as NICE (Nodally Integrated Continuum Elements) formulation by Krysl and collaborators [51, 53, 52, 55, 58]. We mention that the assumed nodal strain-displacement matrix formulation is distantly related to the element-based B-bar technique (Hughes [14]).

The derivation above assumed uniform distribution of material in the volume of the structure. If the material stiffness matrix D is multi-valued at a node, we can create multiple element patches for the node such that each of them has a uniform material distribution. The summation Equation 4.17 can be split into separate terms corresponding to these patches, and we can again use the same arguments used above to derive the assumed nodal deformation gradients. Some general observations of this formulation can provide insights about the advantages and the disadvantages of the formulation.

1. Equation Equation 4.23 gives the shape function gradients at an integration point (node) K for a shape function corresponding to node J. The way in which we defined the element patches for a node implies that the nodes J and K are connected by an element.

2. When the node K lies on a multi-material interface, one can define multiple element patches for the node, each one consisting of elements with the same material. The derivation can be slightly modified, which includes sums over these element patches, each of which can be equated to zero. This again leads to the expression for shape function gradient in Equation Equation 4.23.

3. The NICE formulation can be interpreted as a variant to the $\overline{\boldsymbol{B}}$-technique pioneered by [14] in that, an average of strain-displacement operators is used to construct the assumed strain-displacement operator (Equation Equation 4.19). [14] operator is element-based, and the strain-displacement operator is averaged element-wise. In NICE formulation, averaging is done node-wise over the element patches.

4. The stiffness matrix obtained using the NICE formulation is symmetric, owing to Equation Equation 4.12.

$$\int_{\Omega} \overline{\boldsymbol{B}}_I^T \boldsymbol{D} \overline{\boldsymbol{B}}_J \, d\Omega = \int_{\Omega} \overline{\boldsymbol{B}}_I \boldsymbol{D} \boldsymbol{B}_J \, d\Omega = \int_{\Omega} \boldsymbol{B}_I^T \boldsymbol{D} \overline{\boldsymbol{B}}_J \, d\Omega \tag{4.24}$$

5. The mass matrix obtained using nodal integration is diagonal, which helps in faster inversion in transient dynamic analysis. The mass matrix of an element e is given as

$$\boldsymbol{M}_e = \int_{\Omega_e} \rho_e \boldsymbol{N}^T \boldsymbol{N} \, d\Omega_e \tag{4.25}$$

where ρ_e is the density of the material in the element e, and $\boldsymbol{N}$ is a matrix with shape function values. For constant Jacobian elements, e.g. tetrahedra, the nodally integrated mass matrix becomes

$$\boldsymbol{M}_e = \rho_e \mathcal{J}_e \boldsymbol{I}_{n \times n} \tag{4.26}$$

where $\boldsymbol{I}_{n \times n}$ is an Identity matrix of size n (12 for tetrahedra). For non-constant Jacobian elements, e.g. hexahedra, the nodally integrated mass matrix is given by the scalar product of density of the material and a diagonal matrix with Jacobian determinants computed at the integration points as the diagonal elements.

4.2 Patch Test

The assumed strain-displacement operator at node K in Equation Equation 4.19 is obtained by averaging the strain-displacement operators from the neighboring elements. In terms of strains, nodal strains are obtained by averaging the strains in the neighboring to the corresponding nodes.

$$\bar{\boldsymbol{\varepsilon}}\Big|_{\boldsymbol{x}_K} = \frac{\sum\limits_{e \in \texttt{elems}(K)} \boldsymbol{\varepsilon}_e\big|_{\boldsymbol{x}_K} \mathcal{J}_e\big|_{\boldsymbol{x}_K} w_e\big|_{\boldsymbol{x}_K}}{\sum\limits_{e \in \texttt{elems}(K)} \mathcal{J}_e\big|_{\boldsymbol{x}_K} w_e\big|_{\boldsymbol{x}_K}} \tag{4.27}$$

where $\bar{\boldsymbol{\varepsilon}}\Big|_{\boldsymbol{x}_K}$ is the assumed strain at node K, and $\boldsymbol{\varepsilon}_e\big|_{\boldsymbol{x}_K}$ is the strain in element e.
The patch test is satisfied if the assumed-strain at node K reproduces a constant strain over its element patch. Assuming a constant strain over the element patch,

$$\boldsymbol{\varepsilon}_e\Big|_{\boldsymbol{x}_K} = \boldsymbol{\varepsilon} \quad \forall\, e \in \texttt{elems}(K) \tag{4.28}$$

This implies that the assumed strain given by Equation Equation 4.27 as $\bar{\boldsymbol{\varepsilon}}\Big|_{\boldsymbol{x}_K} = \boldsymbol{\varepsilon}$. Thus, the NICE formulation satisfies the patch test ensuring the consistency of the formulation.

4.3 Dynamic Instability of the NICE formulation

The NICE formulation does not contain any spurious modes in static analyses, as demonstrated in [51]. However, for dynamic problems, e.g. free vibration, some low-energy spurious modes are yielded by the NICE formulation. We illustrate this by means of an example saw-tooth mode. Consider an infinite 1D mesh and nodal integration, with one degree of freedom per node.

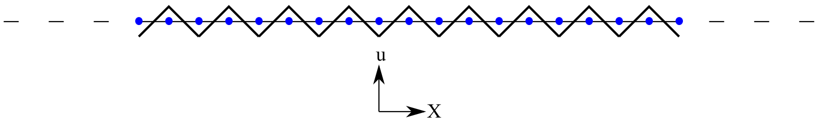

Figure 4.2: Spurious mode in 1D nodal integration

Consider the gradient of field $\boldsymbol{u}$ that varies from positive to negative across the mesh as shown in Figure 4.2. Since nodal gradients are defined as averages of gradient contributions from the connected elements, this setting yields zero nodal strains. This leads to zero potential energy and a spurious stable state for the structure. In a finite mesh, the zero-energy modes are converted to low-energy modes because zero nodal strains do not occur at boundary nodes. This is the reason for such modes not occurring in static analyses. However, these low-energy modes can appear as spurious vibration modes in dynamic simulations. This explanation can be easily extended to 2D and 3D problems. We may also note that structures with large surface to volume ratio (in terms of number of nodes) are less troubled with spurious modes.

In the next chapter, we propose a stabilization procedure to eliminate the spurious modes from the NICE formulation for free vibration problems using a technique we call *Energy-Sampling Stabilization*. Some examples juxtaposing the eigenmodes obtained using stabilized and unstabilized NICE formulations are shown to demonstrate the effectiveness of the stabilization.

4.4 Observations

Upon close analysis of the NICE formulation, some important observations can be made, throwing insights on the bottlenecks of the formulation.

1. The locking in finite elements can be eliminated by using higher order finite elements. This increases computational cost because of requiring to solve larger matrix sizes with larger band widths. The NICE formulation is locking-free without adding additional degrees of freedom. However, because of the way element patches are defined, the band width of the stiffness matrix obtained using NICE elements is larger as compared to the original finite elements from which the NICEs are computed from. The size of matrices of the consistent and assumed-strain formulation is same, but the assumed-strain formulation is thus a bit more expensive.

2. In case of many materials in the structure, each node can be associated with many element patches. This leads to“more” integration points in the formulation, affecting the constraint ratio which could cause some locking if all the materials involved are nearly-incompressible.

3. After some close analysis, one can notice that the assumed-strain at a node K is independent of the displacements $\boldsymbol{u}_K$ at that node. Consider an interior patch with triangular elements for a node K, e.g. Figure 4.1. The assumed-gradient of the shape function corresponding to

node K at integration point (node) K is given using Equation 4.20 as

$$\begin{aligned}
\overline{\nabla N_K}\big|_{\boldsymbol{x}_K} &= \frac{\sum\limits_{e\in\texttt{elems}(K)} \nabla N_{eK}\big|_{\boldsymbol{x}_K} \mathcal{J}_e\big|_{\boldsymbol{x}_K} w_e\big|_{\boldsymbol{x}_K}}{\sum\limits_{e\in\texttt{elems}(K)} \mathcal{J}_e\big|_{\boldsymbol{x}_K} w_e\big|_{\boldsymbol{x}_K}} \\
&= \frac{\sum\limits_{e\in\texttt{elems}(K)} \nabla N_{eK}\mathcal{J}_e}{\sum\limits_{e\in\texttt{elems}(K)} \mathcal{J}_e} \\
&= \frac{\sum\limits_{e\in\texttt{elems}(K)} \nabla N_{eK}\mathcal{A}_e}{\sum\limits_{e\in\texttt{elems}(K)} \mathcal{A}_e} \\
&= \frac{\sum\limits_{e\in\texttt{elems}(K)} \int_{\Omega_e} \nabla N_{eK}\, d\Omega_e}{\sum\limits_{e\in\texttt{elems}(K)} \int_{\Omega_e} d\Omega_e} \\
&= \frac{\int_{\Omega_K} \nabla N_{eK}\, d\Omega_K}{\int_{\Omega_K} d\Omega_K} \\
&= \frac{\int_{\Gamma_K} N_{eK}\, d\Gamma_K}{\int_{\Omega_K} d\Omega_K} \\
&= 0
\end{aligned} \tag{4.29}$$

where the second equation is obtained from the first, using the information that in triangular finite elements, all the weights of nodal integration points are equal and the elements have a constant Jacobian. The third equation is obtained by using the relationship between Jacobian $\mathcal{J}_e$ and the element area $\mathcal{A}_e$. Since the shape function gradients are constant functions inside each element, the third equation can be written as sum of integrals over elements Ω_e, which can be simply put as an integral over the element patch Ω_K. Using Green's theorem, this integral can be transformed to a boundary integral over Γ_K, the boundary of the patch. Observing that the shape function corresponding to node K is zero on the boundary of the patch, we can see that the contribution of displacements at node K to the assumed-strain computed at node K is zero. Given a patch, for different values of displacements at the node K, the assumed-strain at node K is the same, as long as the displacements at the other nodes remain the same. However, the displacements at node K do affect the assumed-strains at other nodes whose element patches contains node K.

4. For non-constant Jacobian elements, e.g. quadrilaterals, the above derivation doesn't prove the independence of assumed-strain at a node K and the displacements at node K. However, it can be shown by hand calculations that the assumed-strain at a node of quadrilateral mesh is independent of displacements at that node. This is extensible to three dimensions for tetrahedra and hexahedra.
5. The dynamic instability of the NICE formulation can cause oscillations in dynamic, free vibration, buckling analyses, and some coercivity is to be added to the NICE formulation to eliminate the oscillations.

Chapter 4 has many details taken from the manuscript, "Sivapuram R, Krysl P. On the Energy-Sampling Stabilization of Nodally Integrated Continuum Elements for Dynamic Analyses. *Finite Elements in Analysis and Design* 2019; **167**:103322, doi:10.1016/j.finel.2019.103322.", and the work is done in collaboration with Prof. Petr Krysl. The dissertation author is the primary investigator of the manuscript.

Chapter 5

Energy–Sampling Stabilization of Nodally Integrated Continuum Elements

As discussed in Chapter 4, the Nodally Integrated Continuum Elements are prone to instability in eigenvalue problems, e.g. free vibration, buckling, etc. This chapter discusses an Energy-Sampling based stabilization technique to remove the spuriousness from the formulation. Several examples are shown to demonstrate the stabilization of eigenmodes obtained, both at the lower and the higher ends of the spectrum.

Bonet et al [50] mentioned, but only theoretically, a stabilization using Stabilized Upwind Petrov-Galerkin (SUPG) method to eliminate spurious modes. Broccardo et al [58] used nodally integrated elements for solving large deformation and buckling problems. The stability was provided with a penalty term based on L_2-norm of difference between assumed and real deformation gradients in their formulation to avoid spuriousness of the buckling modes. However, no rules for choosing the amount of penalization were given and the penalty factor was purely chosen out of numerical experience. Puso and Solberg [57] used a stabilization term based on a matrix norm which was designed using a (compressible) material stiffness matrix for tetrahedral (UT4s) elements. The deviatoric part of material stiffness matrix was used to formulate the stabilization terms in Gee et al [60]. These works employed a uniform stabilization (or penalty) factor over the entire mesh, which was chosen by trial-and-error. Also, they studied the performance of these ad-hoc methods using some large-deformation problems and lower vibration eigenmodes (the incompressible unit cube problem, also analyzed herein). The performance for higher frequency eigenmodes was not demonstrated. The problem of spurious modes is also observed in nodally integrated meshfree methods, and Hillman et al [61] and Wu et al [62] use a strain-gradient based stabilization approach to impart coercivity to their formulations.

Choosing a stabilization factor which works for a range of applications seems to be nontrivial. Using a high amount of stabilization results in stiff modes corresponding to higher frequencies because of shear locking. The use of a uniform stabilization factor over all elements in the mesh can induce shear locking in regions with over-stabilized elements and spuriousness in some other regions where the elements are under-stabilized. Thus, there is a need to develop a consistent way of determining a (nonuniform) stabilization factor for each element of the mesh. We suppose that using mechanics-based stabilization factor would be more effective in choosing about the right amount of stabilization. The aspect ratios of lower order elements directly affect shear locking, so our formulation of stabilization is aimed at eliminating the shear locking from the stabilization terms. The previous research in literature indirectly addressed this issue by choosing a small value for the stabilization factor which seemed nevertheless capable to remove spurious modes from lower end of the frequency spectrum for the problems considered in their respective works. The choice of the stabilization factor tends to matter, as we show in this chapter.

In this work, we employ the concept of energy-sampling stabilization to eliminate the spurious modes produced by nodally integrated elements. We use low-order tetrahedral and hexahedral elements for demonstration. This procedure involves consistent incorporation of stabilization energy terms. The stabilization energy is produced from the displacement-generated strains using full integration and from the assumed strains using nodal integration. The stabilization energies are computed using a fictitious stabilization material, which is designed to reduce shear locking and to eliminate volumetric locking. The shear locking effect is reduced by using a stabilization factor. In this work, we computed the stabilization factor: 1. for tetrahedral elements, fitting a power function to the data collected from numerical experiments on a beam discretized with six tetrahedral elements, 2. for hexahedral elements, using the analytical expression for finite element-based fully-integrated strain energy of a rectangular element (Krysl [47], Sivapuram et al [30]). It bears emphasis that the energy-sampling stabilization was in the past developed for and used with mean-strain assumed-strain formulations [47, 20, 48, 21, 29, 24, 30]. In the present work we marry the energy-sampling stabilization with the nodally integrated elements. The stabilization is used alongside nodally integrated formulation to eliminate spuriousness in free vibration modes. The static analyses are devoid of spuriousness and the stabilization does not affect the ability of NICE formulation in obtaining static solutions. The stabilization can make the NICE formulation a bit more accurate, but the current work focuses only on stabilizing the spurious free vibration modes.

The Energy–Sampling stabilized Nodally Integrated Continuum Elements (ESNICE) formulation is built upon the NICE formulation derived in Chapter 4, using the fully integrated formulation and element aspect ratios to define the amount of stabilization. The next section derives the ESNICE formulation and computes the amount of stabilization required for a candidate tetrahedral or hexahedral element.

5.1 Energy–Sampling Stabilization

This section describes the concept of energy-sampling stabilization which is used to stabilize the nodally integrated elements to eliminate the spurious modes. The strain energy of the structure in question is modified by consistently adding and subtracting strain energy terms that are evaluated using full integration and nodal integration respectively,

$$\Psi(\overline{\boldsymbol{\varepsilon}},\boldsymbol{\varepsilon}) = \int_{\Omega} \mathcal{U}(\overline{\boldsymbol{\varepsilon}})\, d\Omega + \int_{\Omega} \widehat{\mathcal{U}}(\boldsymbol{\varepsilon})\, d\Omega - \int_{\Omega} \widehat{\mathcal{U}}(\overline{\boldsymbol{\varepsilon}})\, d\Omega \tag{5.1}$$

where $\boldsymbol{\varepsilon}$ are the displacement-based strains and $\overline{\boldsymbol{\varepsilon}}$ are the assumed strains defined by Equation 4.7. The newly incorporated stabilization energy density terms are given by

$$\widehat{\mathcal{U}}(\boldsymbol{\varepsilon}) = \frac{1}{2}\boldsymbol{\varepsilon}^T \widehat{\boldsymbol{D}} \boldsymbol{\varepsilon} \qquad \text{and} \qquad \widehat{\mathcal{U}}(\overline{\boldsymbol{\varepsilon}}) = \frac{1}{2}\overline{\boldsymbol{\varepsilon}}^T \widehat{\boldsymbol{D}} \overline{\boldsymbol{\varepsilon}} \tag{5.2}$$

where $\widehat{\boldsymbol{D}}$ is a suitably chosen stiffness matrix. We refer to this artificial material model as the stabilization material. The coefficients of the stabilization material are selected to be related to the coefficients of the real material but such that the formulation improves the response in bending and no locking (shear, or related to stiff material deformation modes, such as incompressibility) is introduced. The first term in Equation 5.1 is nodally integrated, and so it avoids the difficulties due to volumetric locking. The second term in Equation 5.1 is fully integrated and helps in avoiding the spurious modes caused by nodally integrating the first term. The nodally integrated third term is subtracted to maintain consistency of the formulation. The strain energy of the structure using these integration rules is given by

$$\begin{aligned} \Psi(\boldsymbol{u}) = & \sum_{K=1}^{n_{nd}} \sum_{I,J \in \texttt{nodes(elems(K))}} \frac{1}{2} \boldsymbol{u}_I^T \overline{\boldsymbol{B}}_I\big|_{\boldsymbol{x}_K}^T \boldsymbol{D} \overline{\boldsymbol{B}}_J\big|_{\boldsymbol{x}_K} \boldsymbol{u}_J V_K \\ & + \sum_{e=1}^{n_{el}} \sum_{I,J \in \texttt{nodes}(e)} \sum_{K \in \texttt{nodes}(e)} \frac{1}{2} \boldsymbol{u}_I^T \boldsymbol{B}_{eI}\big|_{\boldsymbol{x}_K}^T \widehat{\boldsymbol{D}} \boldsymbol{B}_{eJ}\big|_{\boldsymbol{x}_K} \boldsymbol{u}_J\, \mathcal{J}_e\big|_{\boldsymbol{x}_K} w_e\big|_{\boldsymbol{x}_K} \\ & - \sum_{K=1}^{n_{nd}} \sum_{I,J \in \texttt{nodes(elems(K))}} \frac{1}{2} \boldsymbol{u}_I^T \overline{\boldsymbol{B}}_I\big|_{\boldsymbol{x}_K}^T \widehat{\boldsymbol{D}} \overline{\boldsymbol{B}}_J\big|_{\boldsymbol{x}_K} \boldsymbol{u}_J V_K \end{aligned} \tag{5.3}$$

where $\boldsymbol{u}_I$ is the displacement vector of node I, $V_K = \sum_{e \in \texttt{elems}(K)} \mathcal{J}_e\big|_{X_K} w_e\big|_{X_K}$ is the nodal volume associated with node K.

We design the stabilization material (i.) to be simple, which is consistent with choosing an isotropic model, (ii.) to correct the excessive bending stiffness associated with full integration (shear locking), and (iii.) to avoid introducing volumetric locking. For an isotropic material model, two coefficients are needed - the Poisson's ratio $\widehat{\nu}$ and the Young's modulus $\widehat{E}$. In order to make the material compressible, we know that the Poisson's ratio used should be less than 0.5. The Poisson's ratio of the stabilization material $\widehat{\nu}$ used is adopted here as

$$\widehat{\nu} = \begin{cases} \nu & : \nu \leq 0.3 \\ \dfrac{\nu + 0.3}{2} & : \nu > 0.3 \end{cases} \tag{5.4}$$

The use of full integration engenders shear locking, especially when using linear elements which are used in this work. In order to enhance the bending response, we choose the Young's modulus of the stabilization material $\widehat{E}$ as

$$\widehat{E} = \Gamma E \tag{5.5}$$

where Γ is a factor used to reduce the shear locking effect. For anisotropic materials, the equations Equation 5.4 and Equation 5.5 can use the smallest Poisson's ratio and smallest Young's modulus respectively as ν and E as discussed in [30]. Γ depends on a shape factor Φ which is hypothesized to be a function of the aspect ratio of the finite element. We call this factor Γ the stabilization factor for the rest of the paper. For hexahedral elements, this factor can be directly defined using the analytical expression for the strain energy of a rectangular beam. The analytical strain energy of a rectangular beam is given by

$$\mathcal{U} = \frac{EI}{2L}\alpha^2 \tag{5.6}$$

where α is half the bending angle of the beam, E is the Young's modulus and I is the second moment of area of the beam cross-section. The details of the derivation of the stabilization factor for hexahedral elements is given in [47, 30]. The optimal stabilization factor Γ for hexahedral elements can be computed using the shape factor Φ as

$$\Gamma = \frac{\Phi}{1+\Phi} \quad \text{where} \quad \Phi = 2(1+\widehat{\nu})\frac{\min[h_x^2, h_y^2, h_z^2]}{\max[h_x^2, h_y^2, h_z^2]} \tag{5.7}$$

where h_x, h_y, h_z are the characteristic heights of the hexahedral element.

We use a slightly different approach to formulate the shape factor for linear tetrahedral elements. Again our point of departure is the bending of a beam of uniform rectangular cross-section. The beam is discretized using 6 tetrahedral elements. Bending displacements are applied to the beam and the deformation energy of the beam is computed using linear isoparametric tetrahedral elements. The analytical solution for deformation energy of a rectangular beam subjected to pure bending is given in Equation 5.6. The ratio of the analytical and the finite element based deformation energies yields an estimate of the shear locking undergone by the finite elements. We assume the stabilization factor again as $\Gamma = \dfrac{\Phi}{1+\Phi}$, where we adopt the functional relationship

$$\Phi = br^a \tag{5.8}$$

Here, r is the aspect ratio for tetrahedral elements and (a, b) are fitting parameters, For a given tetrahedral element, four ratios are computed between heights of the tetrahedron and lengths of edges contained in the faces normal to these heights. The aspect ratio r of a tetrahedral element is defined as

$$\begin{aligned} r &= \min[r_1, r_2, r_3, r_4] \\ r_i &= \frac{h_i}{\max[L_{i1}, L_{i2}, L_{i3}]} \end{aligned} \tag{5.9}$$

where h_i is the height of the tetrahedron normal to face i, L_{ij} is the length of edge $j \in [1,3]$ of face i. Since the tetrahedral mesh of the beam is anisotropic, the ratio between finite element-based and analytical strain energies is computed when the bending deformation is applied along both the Y and Z axes (length of the beam is along the X axis). The ratio of energies is computed for the various aspect ratios and for different Poisson ratios of the beam.

This yields the data for the fitting of the coefficients (a,b). For the case of bending along Y axis, the parameters are fitted for each of the Poisson's ratios considered. The same is repeated for the case of bending along Z-axis and the fit parameters are averaged across all the cases. The averaged parameters (a,b) are used to compute the shape factor using Equation 5.8. The fitting is shown in Figure 5.1. We can see that the fitted values of (a,b) would be different if one would consider the bending with respect to Y and Z axes separately. We observed that the dependence of strain energy ratio on Poisson's ratio is weak and so made the ansatz by averaging the fitted (a,b) values across different Poisson's ratios $\big([0.0, 0.4]$ are the possible Poisson's ratios for the stabilization material$\big)$. Accepting the uncertainty of the bending direction in the problems being solved, we averaged the fitted (a,b) values obtained from the two cases. The fitted values are $(a,b) = (2.1016, 1.3113)$ (rounded-off). The stabilization factor used in this work for tetrahedral elements is optimal with respect to this data.

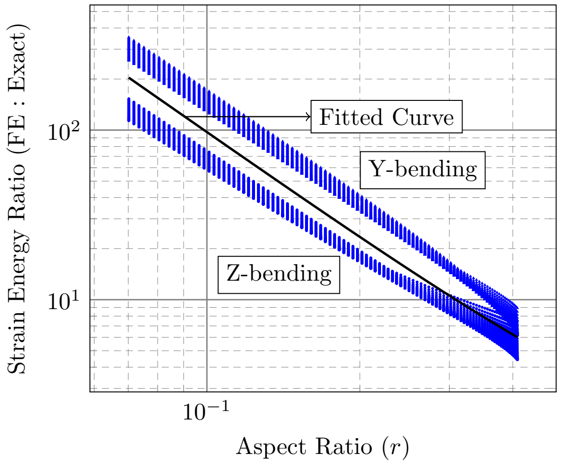

Figure 5.1: Beam with 6 T4 elements - Fit of aspect ratio Vs strain energy ratio

The shape factors for hexahedral and tetrahedral elements are computed using Equation 5.7 and Equation 5.8 respectively. The numerical examples shown in the later sections demonstrate that the stabilization factors help in removing the spurious modes caused by nodal integration.

The stabilization terms do not introduce any volumetric locking because we use a compressible stabilization material. The formulation does not suffer much from shear locking because of the incorporation of the stabilization factor which removes the excess bending stiffness from the elements. The knowledge of the bending plane can further improve the estimation of stabilization factor. In this work, we accepted the uncertainty of the bending plane and so the stabilization factor is computed based on the smallest aspect ratio of the element. We can clearly see that the computation of stabilization factor is very cost-effective. We call this formulation the ESNICE (Energy Sampling-stabilized NICE) formulation in our results and discussion.

In summary, the stabilization material properties reflect both the properties of the real material, and also the shape of the finite elements. Importantly, these are *not* user-controlled quantities, and their values are mechanically determined. This work deals only with linear elasticity, and for nonlinear elasticity similar stabilization terms can be used with the stabilization factor computed using the element aspect ratio as discussed in Krysl [48] and Pakravan et al [29]. The stabilization material for inelastic applications is yet to be investigated and developed.

5.2 Bounds for the Stabilization Factor

A reasonable question is: can we guarantee removal of unphysical (spurious) modes? It is not possible in general, but for meshes of well-shaped elements we can offer some arguments as to how the energy-sampling stabilization of the nodally-integrated formulation is able to eliminate spurious modes successfully. We consider a compressible (say $\nu = 0.3$) material, but the derived bounds are not sensitive to the Poisson's ratio of the material.

The generalized eigenvalue problem for the nodally integrated formulation is used to compute the first (spurious) mode as

$$\boldsymbol{K}_n \boldsymbol{\phi} = \lambda_n \boldsymbol{M} \boldsymbol{\phi} \tag{5.10}$$

where $\boldsymbol{\phi}$ is the first spurious mode in the spectrum obtained using the NICE formulation, λ_n is the corresponding eigenvalue, $\boldsymbol{K}_n$ is the stiffness matrix computed based using the NICE formulation and $\boldsymbol{M}$ is the nodally-integrated (yielding a lumped) mass matrix. Consider the eigenvalue problem using the fully integrated formulation

$$\boldsymbol{K}_f\boldsymbol{\eta} = \lambda_f\boldsymbol{M}\boldsymbol{\eta} \tag{5.11}$$

where $\boldsymbol{K}_f$ is the full integration-based stiffness matrix and $(\lambda_f,\ \boldsymbol{\eta})$ is the eigen pair corresponding to the largest eigenvalue computed using the fully-integrated formulation. The generalized eigenvalue problem for the ESNICE formulation is given by

$$\boldsymbol{K}_s\boldsymbol{\psi} = \lambda_s\boldsymbol{M}\boldsymbol{\psi} \tag{5.12}$$

where $\boldsymbol{K}_s$ is the ESNICE-based stiffness matrix and $(\lambda_s,\ \boldsymbol{\psi})$ is the eigen pair corresponding to the largest eigenvalue computed using the ESNICE formulation. The spurious modes do not occur in the ESNICE formulation when the corresponding last eigenvalue λ_s is smaller than the Rayleigh quotient of the first spurious mode $\boldsymbol{\phi}$ of the NICE formulation. The ESNICE-based stiffness matrix for this setting can be expressed as

$$\boldsymbol{K}_s = (1-\Gamma)\boldsymbol{K}_n + \Gamma\boldsymbol{K}_f \tag{5.13}$$

where Γ is the stabilization factor. It is easy to observe that the ESNICE formulation is softer than the fully-integrated formulation, and so $\lambda_f \geq \lambda_s$. This assumption is true when $\Gamma < 1$, meaning the formulation involves a positive combination of nodally integrated and fully integrated terms (and so is not indefinite). All the eigenvectors in the above equations are assumed to be mass-normalized. The Rayleigh quotient of the first spurious mode $\boldsymbol{\phi}$ of the NICE formulation with respect to $\boldsymbol{K}_f$ can be computed as

$$\begin{aligned} R(\boldsymbol{K}_s,\ \phi) = \phi^T \boldsymbol{K}_s \phi &= (1-\Gamma)R(\boldsymbol{K}_n, \phi) + \Gamma R(\boldsymbol{K}_f,\ \phi) \\ &= (1-\Gamma)\lambda_n + \Gamma R(\boldsymbol{K}_f,\ \phi) \end{aligned} \tag{5.14}$$

where $R(\boldsymbol{K}_f,\ \phi)$ and $R(\boldsymbol{K}_n,\ \phi)$ are the Rayleigh quotients of the spurious mode ϕ with respect to the fully integrated stiffness matrix $\boldsymbol{K}_f$ and the nodally integrated stiffness matrix $\boldsymbol{K}_n$ respectively. The spurious modes can be eliminated using the ESNICE formulation when

$$(1-\Gamma)\lambda_n + \Gamma R(\boldsymbol{K}_f,\ \phi) \geq \lambda_s \tag{5.15}$$

But λ_s depends on Γ too making this a nonlinear inequality. However, we also have $\lambda_f \geq \lambda_s$, and so the above inequality can also be satisfied when

$$\begin{aligned} (1-\Gamma)\lambda_n + \Gamma R(\boldsymbol{K}_f,\ \phi) &\geq \lambda_f \\ 1 > \Gamma \geq \frac{\lambda_f - \lambda_n}{R(\boldsymbol{K}_f,\ \phi) - \lambda_n} &> 0 \end{aligned} \tag{5.16}$$

The lower bound is greater than zero because the largest eigenvalue of the fully integrated formulation λ_f and the computed Rayleigh quotient $R(\boldsymbol{K}_f,\ \phi)$ correspond to high energies as compared to the eigenvalue λ_n of the low energy spurious mode. So, both the numerator and denominator of the bound are positive and hence $\Gamma > 0$.

The bound in Equation 5.16 shows that we can choose a stabilization factor Γ satisfying the inequality and that the chosen factor eliminates the spurious modes from the ESNICE formulation. This derivation holds true for both linear and higher order finite elements. Unlike the higher order elements, the fully integrated stiffness matrix of the linear elements (used in this work) suffers from shear locking. High values of Γ will lead to stiff eigenmodes, and this imposes an upper bound on the Γ value to be chosen. In this work, the Γ value is chosen such that minimal shear locking is observed when the structure is subjected to pure bending. We show through examples in the next section that this procedure for computing Γ efficiently eliminates spurious modes (even at high frequencies) and the modes obtained are devoid of shear locking.

We present the calculations for Γ for some well-shaped elements using energy-sampling stabilization to demonstrate that the Γ chosen this way does satisfy the bounds Equation 5.16. Consider tetrahedra constructed using right triangles (Figure 5.2a) and equilateral triangles (Figure 5.2b), which are seen in regular meshes.

(a) Right-Angled Tetrahedron (b) Equilateral Tetrahedron

Figure 5.2: Regular Tetrahedra

We consider the free vibration of a compressible ($\nu = 0.3$) unit cube discretized using a regular tetrahedral mesh (32 elements per edge) to compute the bound Equation 5.16 for Γ. Solving the free vibration analyses using the nodally-integrated and fully integrated formulations, we find that $\lambda_n = 0.04847$, $\lambda_f = 499.889$ and $R(K_f,\ \phi) = 4190.2418$. The lower bound for Γ from Equation 5.16 can be computed to be 0.11929.

For the right-angled tetrahedron with unit legs in Figure 5.2a, the coordinates are $A := [0,0,0]$, $B := [1,0,0]$, $C := [0,1,0]$, $D := [0,0,1]$. The smallest aspect ratio is given by $h(A \to BCD)$, the perpendicular distance from vertex A to the opposite face BCD and the edge lengths of the face BCD. The aspect ratio is computed using Equation 5.9 as $\dfrac{h(A \to BCD)}{\max(|DB|,\ |DC|,\ |BC|)} = \dfrac{1}{\sqrt{6}}$. Using the aspect ratio and Equation 5.8, we can compute Γ to be 0.1668, which satisfies the bound 0.1193 computed using Equation 5.16 showing that the mechanics-based stabilization eliminates the spurious modes.

For the equilateral tetrahedron with unit edges in Figure 5.2b, the coordinates are $A :=$

$[0,0,0]$, $B := [1,0,0]$, $C := \left[\frac{1}{2}, 0, \frac{\sqrt{3}}{2}\right]$, $D := \left[\frac{1}{2}, \sqrt{\frac{2}{3}}, \frac{1}{2\sqrt{3}}\right]$. All the heights are equal in such a tetrahedron, and the aspect ratio is given by $h(D \to ABC)$, the perpendicular distance from D to the face ABC and the edge lengths of face ABC. The aspect ratio is computed using Equation 5.9 as $\frac{h(D \to ABC)}{\max(|AB|,\ |BC|,\ |CA|)} = \sqrt{\frac{2}{3}}$. The stabilization factor Γ can then be computed to be 0.4613, which also satisfies the bound for Γ showing that the element shape-based factor offers enough stabilization to remove spuriousness.

For regular hexahedral elements, the aspect ratio is 1 (since they are perfect cubes). The Γ computed using Equation 5.7 is 0.7222, which again satisfies the bounds and so guarantees the removal of unphysical free vibration modes from the spectrum of the ESNICE formulation.

5.3 Computing the Nodal Stabilization Factor via Patch Test

As mentioned in the previous section, the stabilization factor is computed element-wise, based on the aspect ratio of the finite elements. However, since our integration points are the nodes, the stabilization factors at each node are multi-valued with different values coming from different neighboring elements. In this section, we ensure that the ESNICE formulation satisfies the patch test by imposing a relationship between the stabilization factor at a node and the stabilization factors of the elements in the corresponding element patch.

The ESNICE formulation uses the volume average of element-based stabilization factors to compute the nodal stabilization factors. We know from the literature that the NICE formulation satisfies the patch test so long as the underlying finite elements satisfy the same. The nodal stabilization factor can be designed based on the element-based stabilization factors by making the ESNICE formulation satisfy the patch test. Consider a node K and a corresponding element-patch. Assume a constant strain $\boldsymbol{\varepsilon}$ across the element-patch. The NICE formulation, i.e., the first term of ESNICE formulation is known to satisfy patch test because the nodal strain equals the constant element-patch strain. This indicates that the ESNICE formulation satisfies the patch test when the second and third terms together have a trivial contribution to the strain energy at node K. Defining $\tilde{\mathcal{U}}_K = \frac{1}{2}\boldsymbol{\varepsilon}^T \widetilde{\boldsymbol{D}} \boldsymbol{\varepsilon}$ as the strain energy density where $\widetilde{\boldsymbol{D}}$ is the stabilization material stiffness matrix without the stabilization factor, this cancellation condition at node K can be written as

$$-\overline{\Gamma}_K \ \tilde{\mathcal{U}}_K V_K + \sum_{e \in \mathtt{elems}(K)} \Gamma_e \ \tilde{\mathcal{U}}_K \mathcal{J}_e\big|_{\boldsymbol{x}_K} w_e\big|_{\boldsymbol{x}_K} = 0 \tag{5.17}$$

where $\overline{\Gamma}_K$ is the stabilization factor for node K and Γ_e is the stabilization factor for element e. Removing the constant factor $\tilde{\mathcal{U}}_K$ from the equation and using the expression for nodal volume, we obtain

$$\overline{\Gamma}_K = \frac{\sum_{e \in \mathtt{elems}(K)} \Gamma_e \ \mathcal{J}_e\big|_{\boldsymbol{x}_K} w_e\big|_{\boldsymbol{x}_K}}{\sum_{e \in \mathtt{elems}(K)} \mathcal{J}_e\big|_{\boldsymbol{x}_K} w_e\big|_{\boldsymbol{x}_K}} \tag{5.18}$$

This expression indicates the volumetric averaging of the element-based stabilization factors to compute the stabilization factor for node K. We use this in the ESNICE formulation so as to enable the formulation to satisfy the patch test.

We should note that nodal integration is full integration for T4 elements but not for H8 elements. For H8 elements, we use the $2 \times 2 \times 2$ Gaussian quadrature for the fully integrated term in Equation 5.3. However, for the purpose of patch test, we need to consider constant strains in the elements of the element patch corresponding to the node K. For constant strains, the strain energy is constant over the elements. This implies that the fully integrated term using Gaussian quadrature for H8 elements can be replaced by nodal integration for the purpose of constant-strain patch test. This implies the nodal stabilization factor in Equation 5.18 holds for H8 elements also, even though they use a non-nodal integration for the fully integrated term in the ESNICE formulation.

Some additional observations can be made about the ESNICE formulation which throw some insight into a deeper understanding of the formulation.

1. The fully integrated term in the ESNICE formulation appears to be susceptible to ill-

conditioning for slivers and other poorly shaped elements. We can observe that the stabilization factor depends on the element aspect ratio. The shape factor Φ in Equation 5.8 involves a quadratic exponent (for ESNICE-T4 elements, it is slightly higher than quadratic) of aspect ratio r. This makes the stabilization factor Γ reach zero faster than element volume in the limit of a sliver,

$$\lim_{t \to 0} \frac{\Gamma}{V} = 0 \tag{5.19}$$

where V is element volume and t is the element thickness. This makes the contribution from the stabilization terms in case of slivers trivial. Thus, in case of near-to-zero volume elements and slivers, only the first term of the ESNICE formulation is significant. The first term can robustly handle slivers, extremely thin elements, and even elements of negative volume, as shown in Krysl and Kagey [53].

2. The ESNICE formulation yields symmetric stiffness matrices, just as the NICE formulation.
3. Using the nodal stabilization factor as mentioned in Equation 5.18, the patch test is satisfied.
4. Nodes on multi-material interfaces could be dealt just like in the case of NICE formulation, by defining multiple element patches for each node.

5.4 Examples

Given that our goal was to stabilize the nodally-integrated formulation so that it would become suitable for free-vibration problems we omit any illustrations of the response in static problems herein.

The stabilization is designed so that the static response is enhanced, if anything, relative to the unstabilized NICE formulation [51] as the formulation without stabilization tends to be quite flexible. The stabilization would tend to work against this excessive flexibility.

This section shows some free vibration analysis problems demonstrating the effectiveness of ESNICE formulation. Both tetrahedral and hexahedral elements are investigated. We test the NICE [51, 53] formulations, the UT4s of [57], and high fidelity elements (quadratic 27-node and 20-node hexahedra and 10-node tetrahedra) for comparison. In the analyses shown, NICE formulation does not use any stabilization unless otherwise specified.

5.4.1 Unconstrained Cylinder, compressible material

This example considers the free vibration of a cylinder (radius 6 inch, length 24 inch) to demonstrate the effectivity of energy-sampling stabilization in curbing the spurious modes due to nodal integration. The cylinder is not subjected to any boundary conditions. The Young's modulus, Poisson's ratio and density of the compressible material (aluminum) are respectively 70 GPa, 0.33 and 2700 $\mathrm{kg/m^3}$. The ESNICE formulation is tested for both tetrahedral (ESNICE-T4) and hexahedral (ESNICE-H8) elements against high fidelity frequencies obtained using a fine triquadratic hexahedral (H27) mesh. A tetrahedral mesh (28372 elements, 5697 nodes) and a hexahedral mesh (7980 elements, 9021 nodes) are used for investigation.

5.4.1.1 Varying amounts of stabilization

The results obtained with a stabilized NICE formulation using varying amounts of stabilization demonstrate that the frequency spectrum depends greatly on the amount of stabilization used. The stabilization procedure is same as that of the ESNICE formulation except that a fixed amount of stabilization is used uniformly across all the finite elements in lieu of using the proposed shape-dependent stabilization factors.

We can clearly observe from the frequency spectra in Figure 5.3a that the performance of NICE-T4s is subject to appropriately chosen stabilization, and choosing such value a priori is not possible. This limits the use of such ad-hoc values for stabilizing the NICE formulation. The frequency spectra obtained using NICE-H8s and varying amounts of stabilization is shown in Figure 5.3b. It can be seen that the chosen stabilization values greatly affect the frequency spectrum, just as in the tetrahedral case. When appropriate amount of stabilization (unknown a priori) is not used, the obtained eigenmodes can be very unphysical. When the elements are over-stabilized, i.e. the stabilization factor used is much higher than an appropriate value, shear-locking occurs or even worse the stiffness matrix of the formulation can become indefinite.

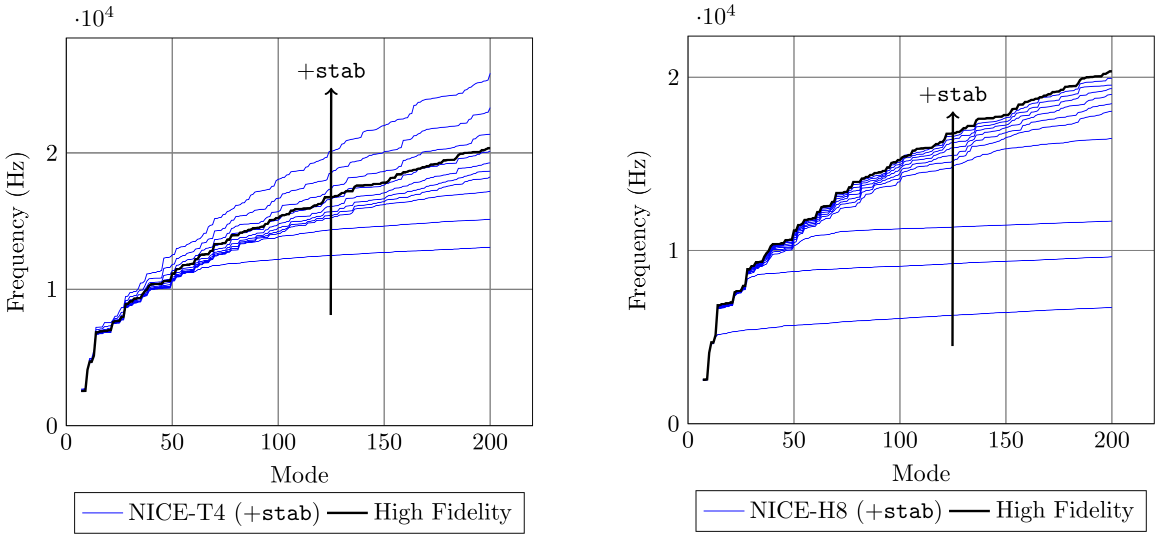

(a) NICE-T4 (`stab` $\in [0.04, 4.0]$)

(b) NICE-H8 (`stab` $\in [0.01, 1.2]$)

Figure 5.3: Aluminum Cylinder (NICEs with uniform stabilization) - Frequency spectrum $(7-200)$

The lower frequency eigenmodes such as eigenmode 10 do not show spuriousness for the range of stabilization factors used in the investigation. For the sake of brevity, we do not show the mode shapes since they match well with the mode shape obtained using T4 elements shown in Figure 5.4c. The higher frequency eigenmodes however depend very much on the amount of stabilization chosen. The mode shapes of eigenmode 95 is shown in Figures 5.5b, 5.5c, 5.5d using different amounts of stabilization. These eigenmodes display less spuriousness than when using no stabilization (see Figure 5.5a). It is observed that using low amount of stabilization, the eigenmode 95 exhibits spuriousness (see Figure 5.5b) and the mode shape is observed to be corresponding to a low-frequency eigenmode due to spuriousness at the lower end of frequency spectrum. Using high amount of stabilization (Figure 5.5d) induces shear locking and yields a stiff eigenmode corresponding to a higher frequency (cf. the eigenmode obtained using T4 elements in Figure 5.5f).

For the hexahedral mesh used, eigenmode 13 obtained using different amounts of stabilization is shown in Figures 5.7b, 5.7c, 5.7d and we can observe that for this example, the spuriousness decreases as the stabilization factor chosen is increased (cf. the eigenmode obtained using H8 elements in Figure 5.7e). The same characteristic is observed at higher frequency eigenmodes like eigenmode 50 as shown in Figures 5.8b, 5.8c, 5.8d for increasing amounts of stabilization. For very low amount of stabilization used, the eigenmode obtained is observed to be completely unphysical (see Figure 5.7b). The spuriousness of the eigenmode decreases for higher stabilization factors. The use of uniform stabilization leads to some portions of the structure exhibiting spuriousness as seen in Figure 5.8c. This disappears on further increasing the stabilization factor.

This study demonstrates that choosing the stabilization factor a priori is nontrivial and a badly chosen stabilization factor can lead to shear-locked or spurious eigenmodes. We show that the use of energy-sampling technique yields optimum amount of stabilization for each finite element which helps to curb spuriousness in eigenmodes whilst not causing shear locking.

5.4.1.2 ESNICE stabilization

We start by comparing the mode shapes at the lower and higher ends of the frequency spectrum using tetrahedral elements. We can see from Figure 5.4 that ESNICE-T4s eliminate the spuriousness caused by the NICE-T4s (UT4s elements do the same) and the mode shape matches well with that produced by T4 elements. Figure 5.5 shows eigenmode 95 using all the considered tetrahedral elements. It can be seen that the UT4s elements yield spurious higher eigenmodes because of insufficient stabilization. The ESNICE-T4s give the correct (nonspurious) mode shape matching with that produced by T4 elements. The energy-sampling stabilization applies a nonuniform stabilization factor over the mesh. In this example, the nodal stabilization factors obtained for the tetrahedral elements are observed to be in range $[0.1045, 0.3245]$ (rounded-off). This example demonstrates that energy-sampling stabilization gets rid of spurious modes effectively both at the lower and higher ends of the frequency spectrum. A further fine mesh is used to investigate the (non)spuriousness of the eigenmodes obtained using ESNICE-T4s. We can see from Figure 5.6 that eigenmode 2000 obtained using ESNICE-T4s is nonspurious (spuriousness is associated with jagged shapes). This shows that the energy-sampling stabilization helps in removing spuriousness from higher order modes too using shape-based stabilization.

For the hexahedral mesh, eigenmode 13 is shown in Figure 5.7 using different hexahedral elements. The NICE-H8s exhibit spuriousness which is efficiently eliminated using ESNICE-H8s. Figure 5.8 shows the eigenmode 50 and again, ESNICE-H8s produce physical eigenmode which matches well with that produced by H8 elements. The nonuniform stabilization factor based on the element aspect ratio computed using Equation 5.7 is observed to be in range $[0.4901, 0.7168]$ (rounded off).

The tetrahedral mesh is used to compare the frequency spectra obtained using ESNICE, NICE and UT4s elements (Puso and Solberg [57]). The UT4s elements use a uniform stabilization factor of 0.05 while the ESNICEs use nonuniform stabilization computed using Equation 5.8. The comparison of frequency spectra obtained using ESNICE-T4, unstabilized NICE-T4 and UT4s elements is shown in Figure 5.9a. We can observe that the NICE-T4 and UT4s spectra flatten out (the former faster than the latter) because of the existence of spurious modes in the respective spectra. The UT4s elements provide stabilization (elimination of spuriousness) at lower end of the spectrum but seem to exhibit spurious higher eigenmodes. The ESNICE-T4s on the other hand, do not contain spurious modes and so the flattening out of the frequency spectrum is prevented in the frequency range considered. The frequency spectra obtained using ESNICE-H8 and unstabilized NICE-H8s are compared against high fidelity frequencies in Figure 5.9b. The NICE-H8s produce spurious modes, indicated by the flat curve in the spectrum. The ESNICE-H8s do not produce spurious modes and can be observed to match the high fidelity frequencies even at higher end of the frequency spectrum. The H8 elements also seem to produce a very good estimation of the spectrum.

This example demonstrates the effectivity of energy-sampling stabilization in eliminating the spurious modes in both tetrahedral and hexahedral elements.

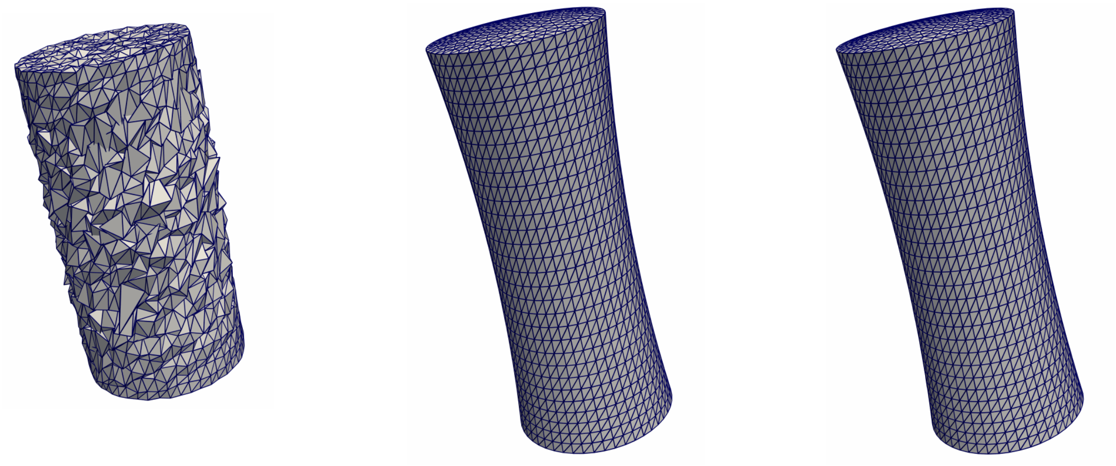

(a) NICE-T4

(b) ESNICE-T4

(c) T4

Figure 5.4: Aluminum Cylinder (Tetrahedral mesh) - Mode 10

5.4.2 Unconstrained Cylinder, Nearly-Incompressible material

The analysis of an unconstrained cylinder is repeated using the same tetrahedral and hexahedral meshes as in Subsection 5.4.1 with a nearly-incompressible material ($\nu = 0.49999$). The Young's modulus and density of the material used are 70 GPa and 2700 $\mathrm{kg/m^3}$ respectively. The stabilization material is chosen as compressible according to Equation 5.4 which is a bit different from the one chosen in the UT4s formulation (cf. Puso et al [57]).

Figure 5.10a shows the frequency spectra obtained using T4, ESNICE-T4, NICE-T4 and UT4s formulations compared with a frequency spectrum corresponding to a fine H27 mesh. The T4 elements undergo high amount of locking, yielding very high frequencies. The NICE spectrum flattens out after a few physical lower eigenmodes implying spuriousness. The UT4s formulation

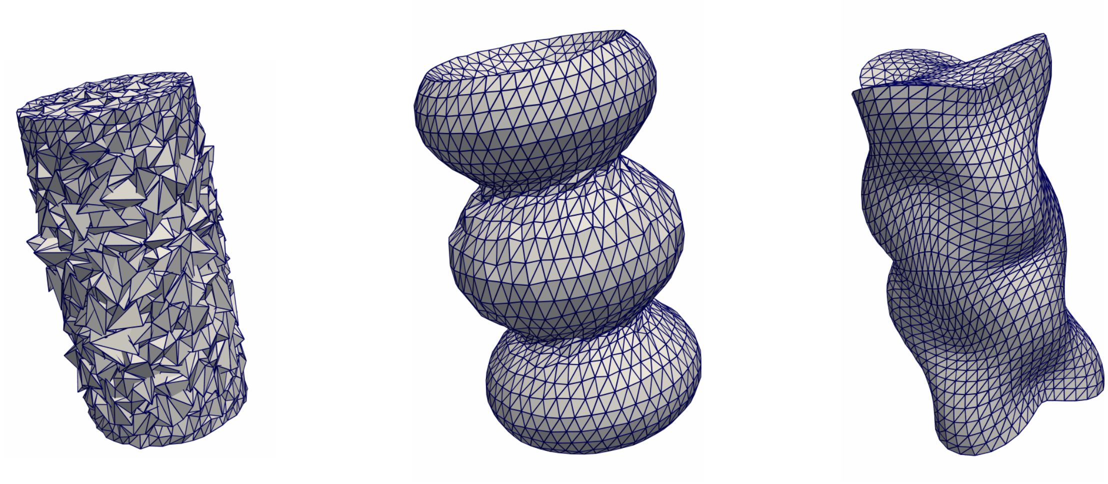

(a) NICE-T4

(b) NICE-T4 ($\texttt{stab} = 0.04$)

(c) NICE-T4 ($\texttt{stab} = 0.86$)

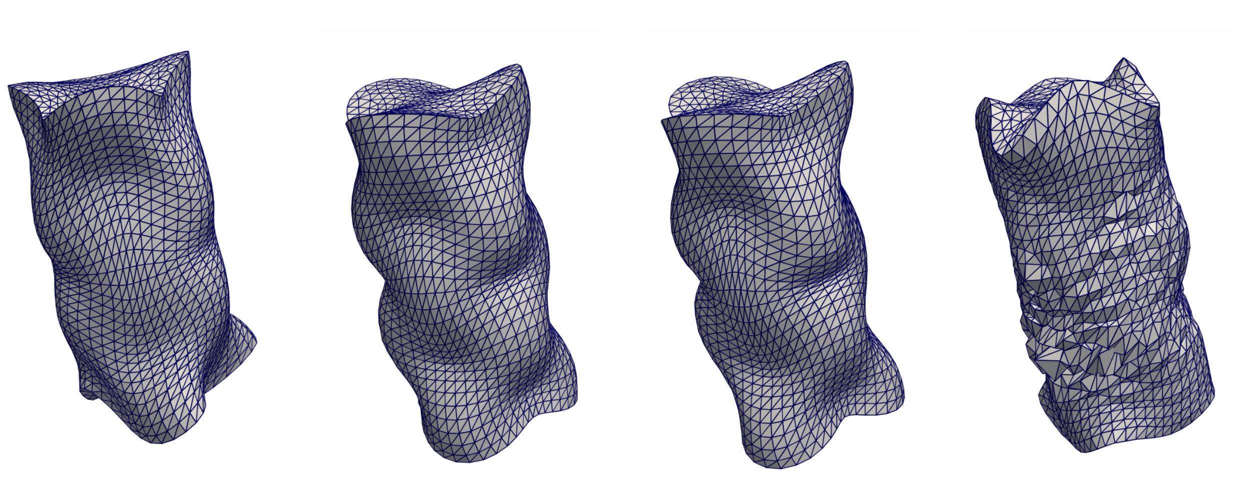

(d) NICE-T4 ($\texttt{stab} = 4.0$)

(e) ESNICE-T4

(f) T4

(g) UT4s

Figure 5.5: Aluminum Cylinder (Tetrahedral mesh) - Mode 95

effectively stabilizes the lower modes. For higher modes, ESNICE-T4s show better accuracy in terms of frequency and nonspuriousness. Figure 5.10b shows the frequency spectra estimated by H8, NICE-H8 and ESNICE-H8 formulations compared with a high fidelity H27-based frequency spectrum. The NICE-H8s show spuriousness even at the lower frequency eigenmodes. The NICE-H8 formulation is expected to exhibit more spurious modes than the NICE-T4 formulation because the former uses bilinear strains in the elements as compared to the latter which uses

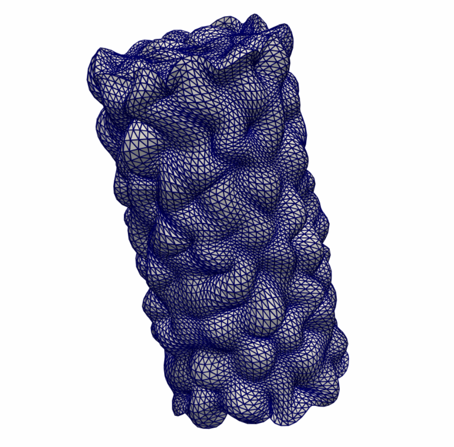

Figure 5.6: Aluminum Cylinder (Fine mesh and ESNICE-T4) - Mode 2000

constant strains. This leads to more variables involved in describing the elemental strains and so more ways to make the nodal strains zero in the NICE-H8s.

Figure 5.11 and Figure 5.12 show the mode shapes of lower and higher frequency eigenmodes resolved using the tetrahedral elements considered. The T4 elements lock volumetrically, and so the corresponding stiff eigenmodes are not shown. We can clearly see that the stabilization added in both UT4s and ESNICE-T4 formulations is sufficient to yield physical modes 11 and 94 (as examples) where NICE-T4 elements exhibit spuriousness. However, we observe that the UT4s elements display spuriousness at even higher eigenmodes. We show in Figure 5.13 and Figure 5.14 some higher frequency eigenmodes corresponding to UT4s elements and ESNICE-T4s respectively, and we can clearly observe that the UT4s modes are spurious unlike the ESNICE-T4 modes. The regions of spuriousness in the UT4s eigenmodes indicate the under-stabilization in some elements. This does not occur in ESNICE-T4s since they use different appropriate amounts of stabilization for differently-shaped elements. The mismatch between ESNICE-T4 and high fidelity spectra is attributed to the inaccurate (not yet converged) eigenvalues estimated by the ESNICE formulation.

Figure 5.15 and Figure 5.16 show the 7th and 50th eigenmodes respectively obtained using H20, NICE-H8 and ESNICE-H8 formulations. We can clearly observe that the ESNICE

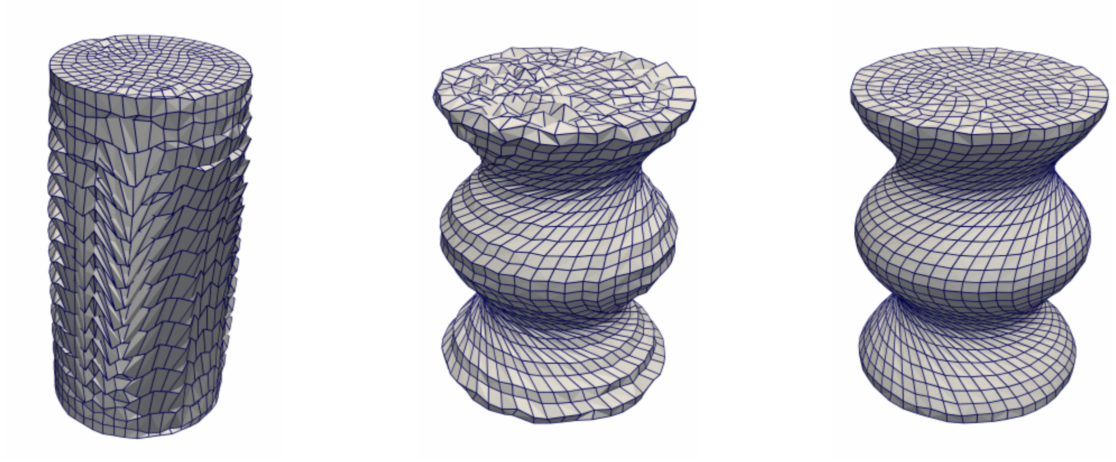

(a) NICE-H8 (b) NICE-H8 ($\texttt{stab} = 0.01$) (c) NICE-H8 ($\texttt{stab} = 0.12$)

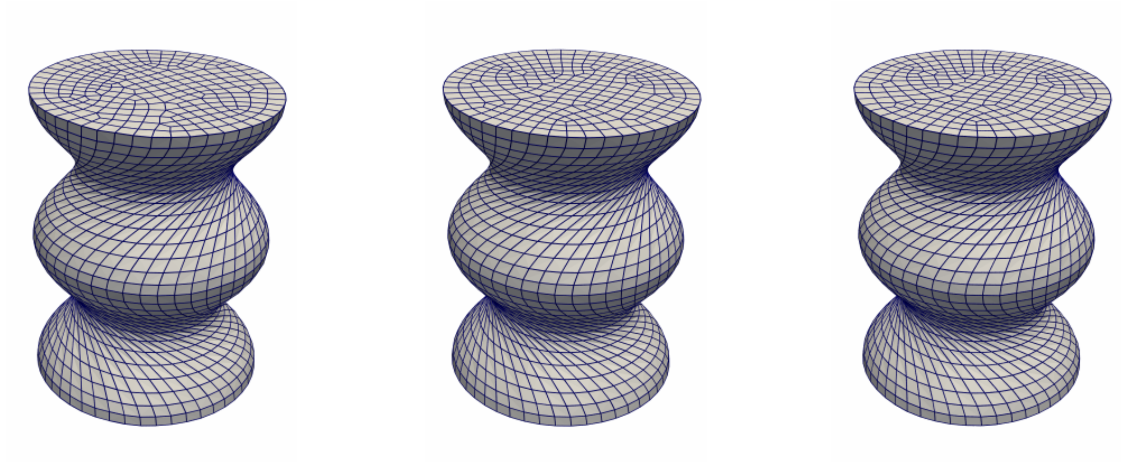

(d) NICE-H8 ($\texttt{stab} = 0.6$) (e) H8 (f) ESNICE-H8

Figure 5.7: Aluminum Cylinder (Hexahedral mesh) - Mode 13

formulation eliminates the spuriousness caused by nodal integration in both of the eigenmodes. The obtained ESNICE modes also match well with the corresponding H20-based modes.

5.4.3 Rectangular Plate

We consider the free vibration of a moderately thick rectangular plate ($4.0 \times 1.0 \times 0.1$ m^3) with no boundary conditions applied. The density, Young's modulus and Poisson's ratio of the material used are 7850 kg/m^3, 210 GPa and 0.3 respectively. The performance of energy-sampling stabilized elements is tested and convergence studies are performed using tetrahedral

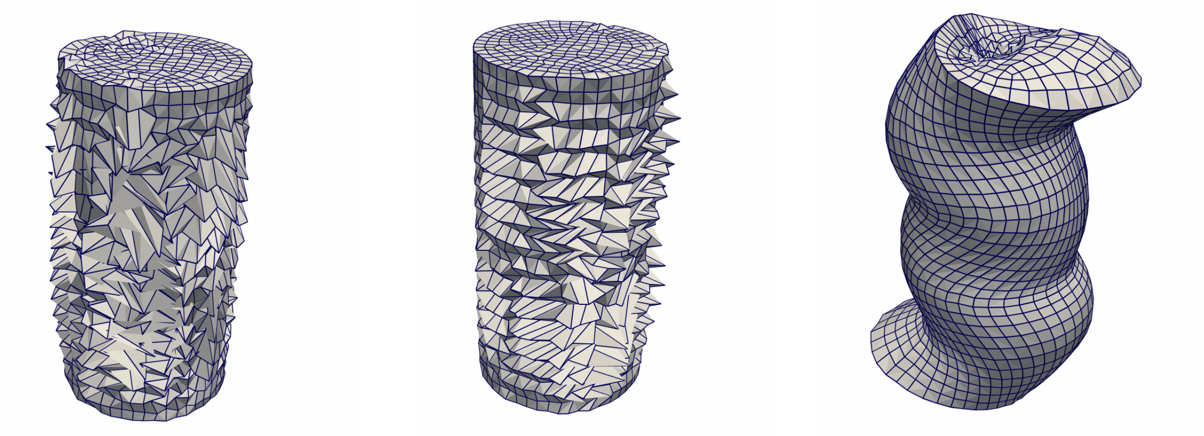

(a) NICE-H8 (b) NICE-H8 (`stab` = 0.01) (c) NICE-H8 (`stab` = 0.12)

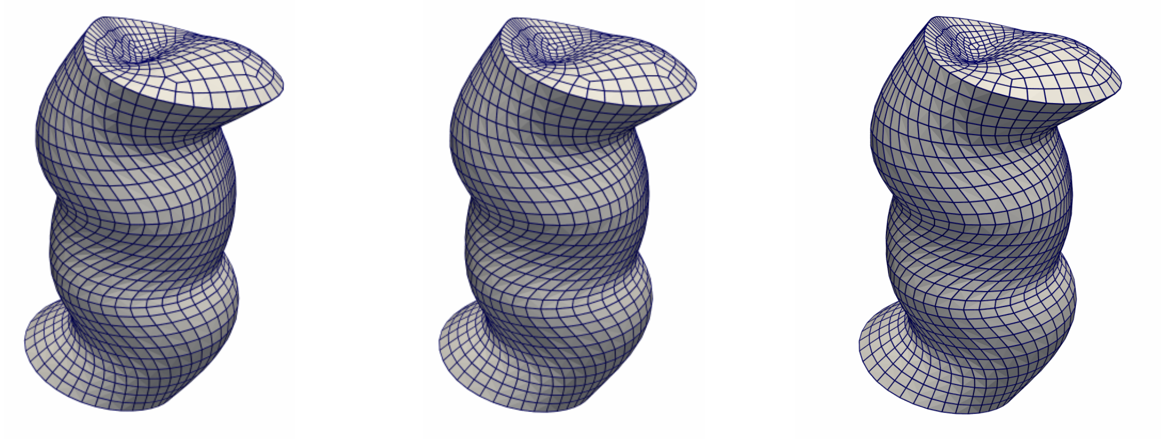

(d) NICE-H8 (`stab` = 0.6) (e) H8 (f) ESNICE-H8

Figure 5.8: Aluminum Cylinder (Hexahedral mesh) - Mode 50

and hexahedral meshes. The coarsest meshes (refinement level 0) used for convergence study are shown in Figure 5.17. The mesh is refined by doubling the number of elements along each of the edges. The convergence plots are made using the finest H20-based spectrum (High Fidelity) as reference values.

The comparison of frequencies obtained using ESNICE-T4, NICE-T4, T4 and UT4s elements is shown in Figure 5.18a at refinement level 2. We can observe that the T4 elements overestimate the frequencies as compared to the H20-based frequencies because of shear locking. The NICE-T4s produce low energy spurious modes and are observed to have a spectrum very different (low frequency estimates) as compared to the high fidelity spectrum. We observe

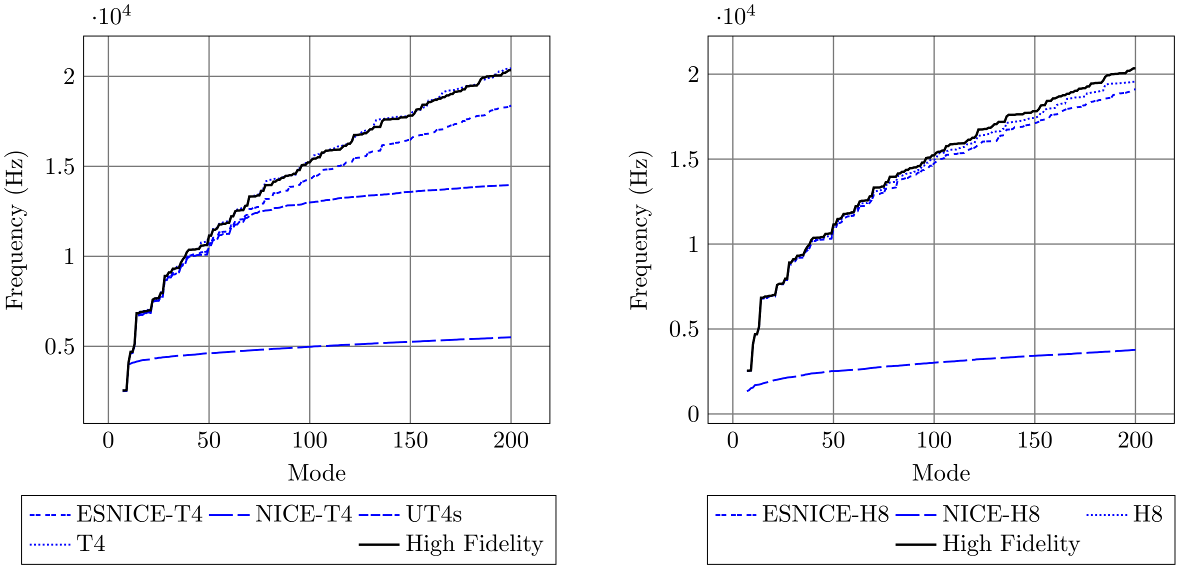

(a) Comparison of ESNICE, NICE, UT4s elements (b) Comparison of ESNICE and NICE elements

Figure 5.9: Aluminum Cylinder - Frequency spectrum $(7-200)$

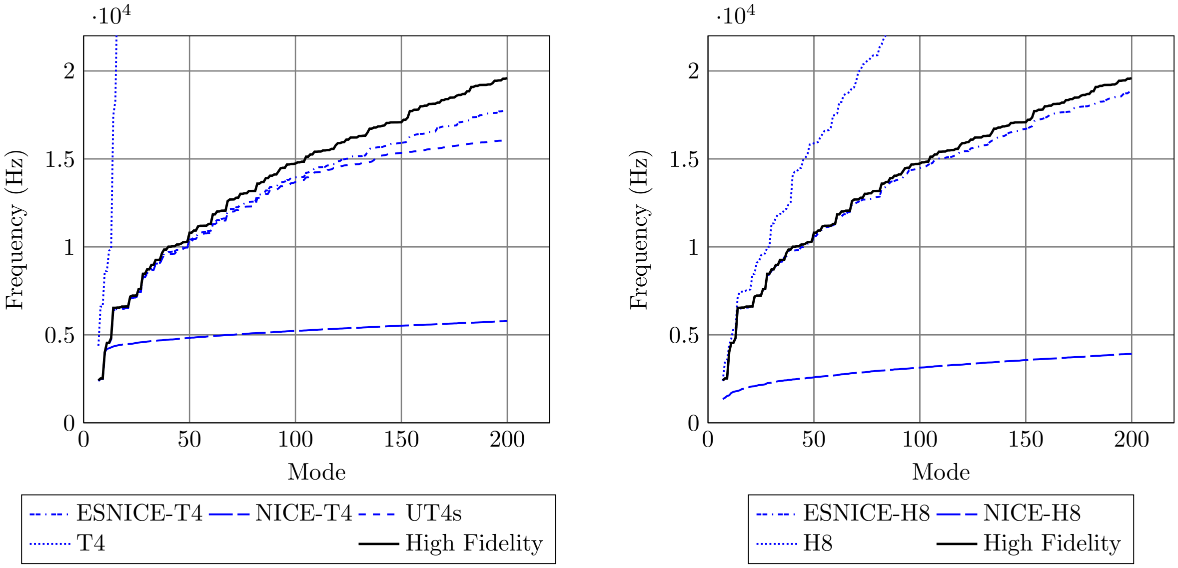

(a) Tetrahedral elements (b) Hexahedral elements

Figure 5.10: Nearly-Incompressible Cylinder - Frequency spectrum $(7-200)$

that at refinement level 2, both ESNICE-T4 and UT4s elements yield very good approximation of frequencies, with ESNICE-T4s being marginally more accurate. Figure 5.18b compares the frequency spectra of H8, ESNICE-H8 and NICE-H8 formulations against the high fidelity

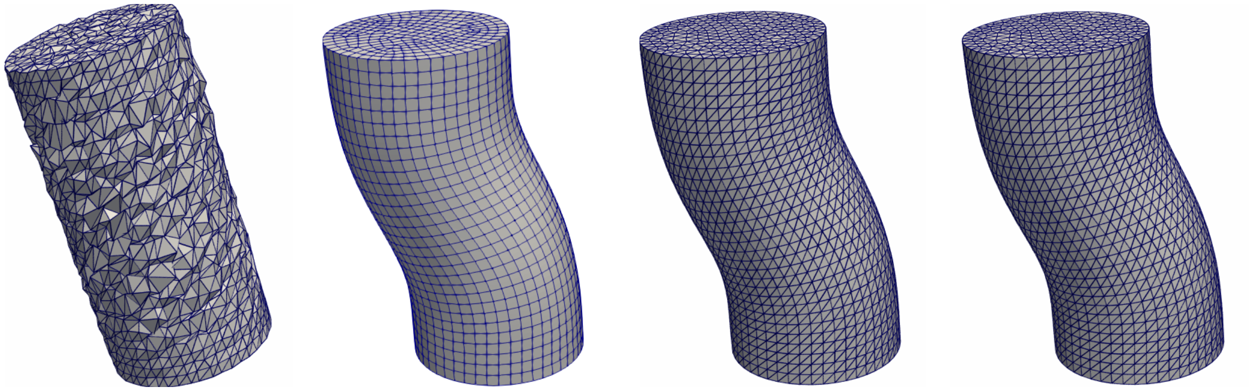

(a) NICE-T4 (b) H20 (c) ESNICE-T4 (d) UT4s

Figure 5.11: Nearly-Incompressible Cylinder (Tetrahedral mesh) - Mode 11

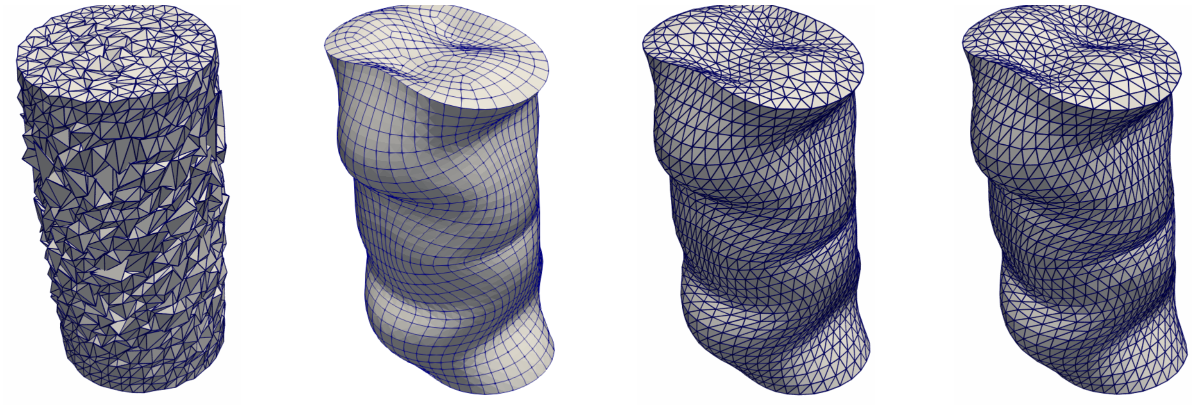

(a) NICE-T4 (b) H20 (c) ESNICE-T4 (d) UT4s

Figure 5.12: Nearly-Incompressible Cylinder (Tetrahedral mesh) - Mode 94

spectrum at refinement level 2. The shear locking tendency is usually less in H8 elements as compared to T4 elements (because of the trilinear shape functions) and so they approximate the spectrum better than T4 elements. The NICE-H8s produce a spectrum completely dominated by spurious modes whilst the ESNICE-H8s effectively stabilize the nodally integrated elements yielding a spectrum closely matching the high fidelity spectrum.

The mode shape of eigenmode 15 is shown in Figure 5.19 for all the tetrahedral elements considered at refinement level 1. The NICE-T4s exhibit spuriouness (Figure 5.19a), the T4 elements yield an eigenmode (Figure 5.19c) corresponding to a high frequency (we observed that it matches with eigenmode 22) because of shear locking whilst the UT4s (Figure 5.19d) and

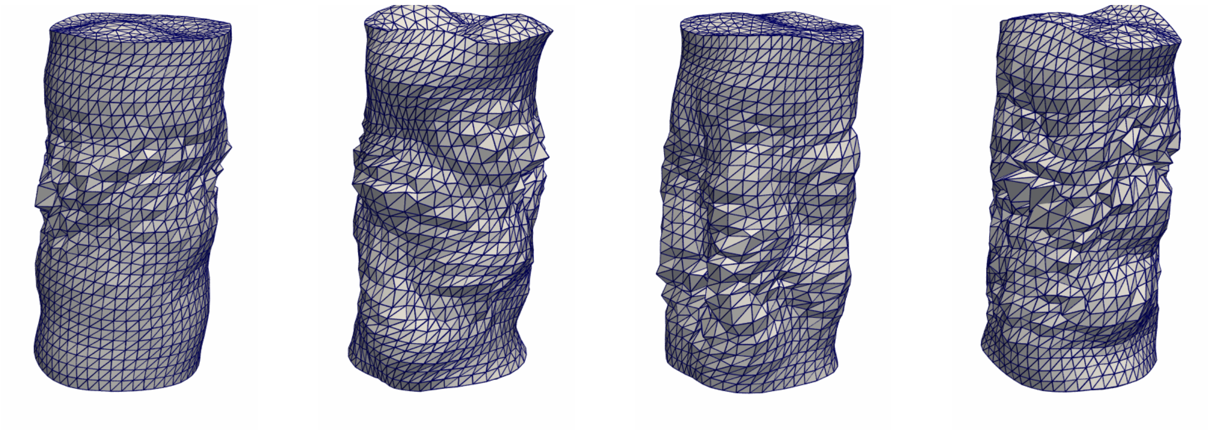

(a) Mode 137 (b) Mode 162 (c) Mode 174 (d) Mode 192

Figure 5.13: Nearly-Incompressible Cylinder - UT4s formulation

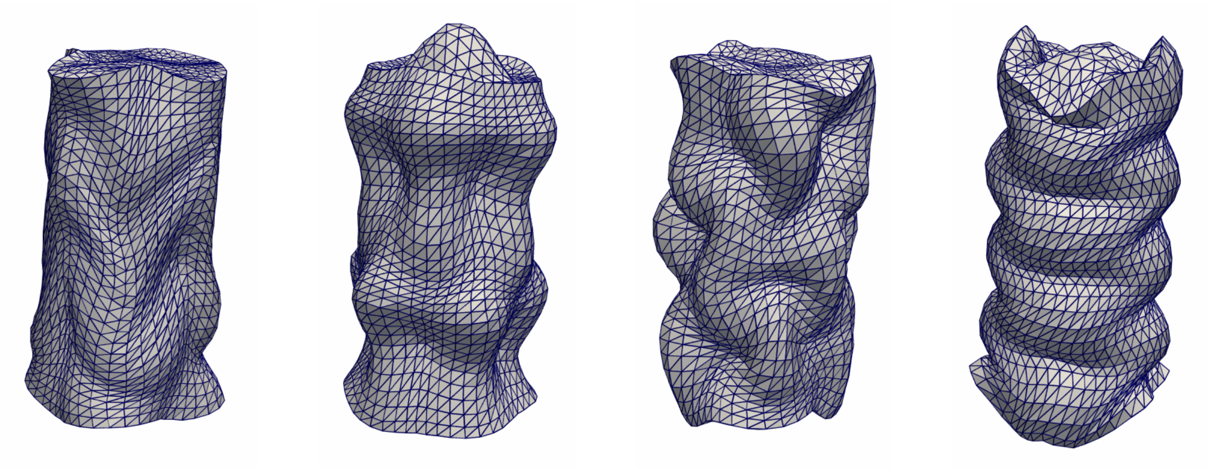

(a) Mode 137 (b) Mode 162 (c) Mode 174 (d) Mode 192

Figure 5.14: Nearly-Incompressible Cylinder - ESNICE-T4 formulation

ESNICE-T4 (Figure 5.19b) formulations incorporate sufficient stabilization to curb the spuriousness. We can also observe that the modes obtained using UT4s and ESNICE-T4 formulations match with that produced by H20 mesh (see Figure 5.19e). A general observation is that plate like structures exhibit fewer spurious modes because of higher surface-to-volume ratio as discussed in Section 5.1. This is the reason that there is no spurious mode observed using the nodal integration until the eigenmode 15. The UT4s formulation works well in eliminating spuriousness too, but we observe spurious higher eigenmodes when coarse meshes are used. Figure 5.20 shows

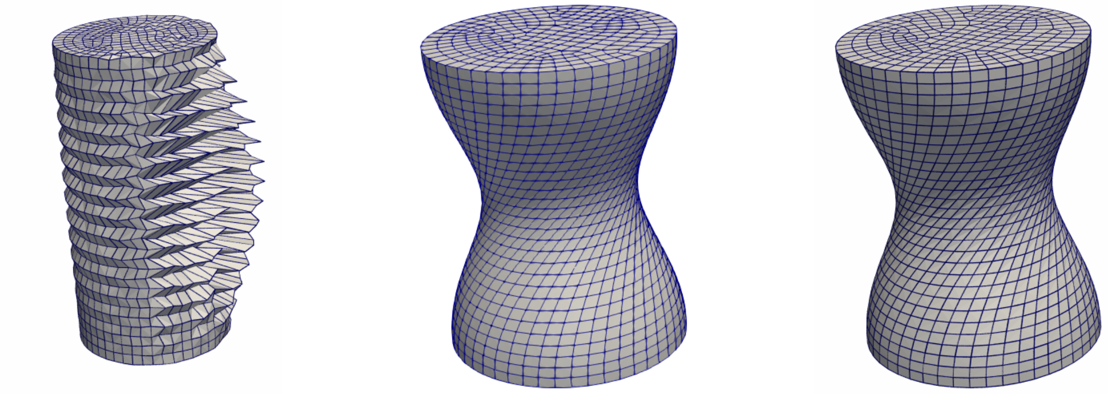

(a) NICE-H8 (b) H20 (c) ESNICE-H8

Figure 5.15: Nearly-Incompressible Cylinder (Hexahedral mesh) - Mode 7

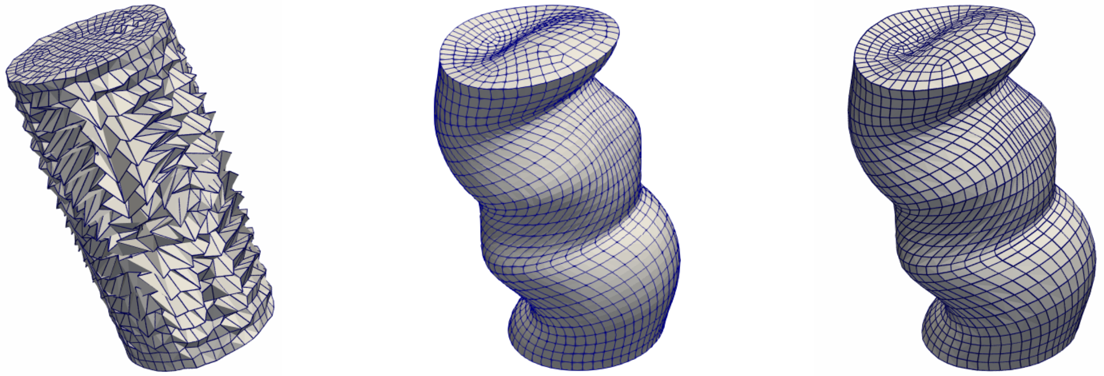

(a) NICE-H8 (b) H20 (c) ESNICE-H8

Figure 5.16: Nearly-Incompressible Cylinder (Hexahedral mesh) - Mode 50

eigenmode 93 produced using ESNICE-T4 and UT4s formulations, and the UT4s elements exhibit spuriousness unlike the ESNICE-T4s. We note that the stabilization factor computed using energy-sampling theory is roughly around 0.089 (rounded-off) for all the tetrahedral elements. The mode shape of eigenmode 13 using hexahedral elements is shown in Figure 5.21 which shows that the ESNICE-H8s effectively curb the spuriousness caused by nodal integration (cf. the spurious mode produced by NICE-H8s in Figure 5.21a). We observe that the stabilization factor computed using energy sampling Equation 5.7 is 0.394 (rounded-off) for all the hexahedral elements in the mesh.

It can be seen by comparing the convergence plots of frequencies obtained using ESNICE-T4 (Figure 5.22c) and UT4s (Figure 5.22d) formulations that ESNICE-T4s perform better in terms of accuracy. The eigenmodes produced by T4 elements are marked by shear locking (especially using coarse meshes), and the frequency error is observed to be higher than that of ESNICE-T4s and UT4s elements, as shown in Figure 5.22. The NICE-T4s do not contain any spurious mode in the range $[7, 11]$, and so the convergence is smooth, yet the errors are higher than those of ESNICE-T4s. Figure 5.23 shows the convergence plots showing the errors in frequency estimation caused by the considered hexahedral elements. The NICE-H8s do not converge, because of spurious modes while the H8 elements and ESNICE-H8s show good convergence because of not being affected by any type of locking. The convergence of ESNICEs is sometimes oscillatory, when the frequencies converging from above the exact frequencies shift to below, and vice-versa. Such a convergence is not unexpected of an assumed-strain approach.

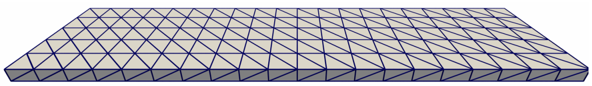

(a) Tetrahedral mesh

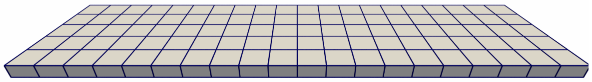

(b) Hexahedral mesh

Figure 5.17: Rectangular Plate - Coarsest Meshes (refinement level 0) used in convergence study

5.4.4 Nearly-incompressible Cube

We consider a unit cube made of nearly incompressible material ($\nu = 0.499$) to demonstrate the superior performance of ESNICEs over both NICEs and fully integrated elements. The fictitious material used for this example has a Young's Modulus of 1 Pa and density of 1 $\mathrm{kg/m^3}$ [57]. The investigation is performed using both tetrahedral and hexahedral meshes. The error comparison is done relative to the frequency spectrum obtained using a dense H20 (high fidelity)

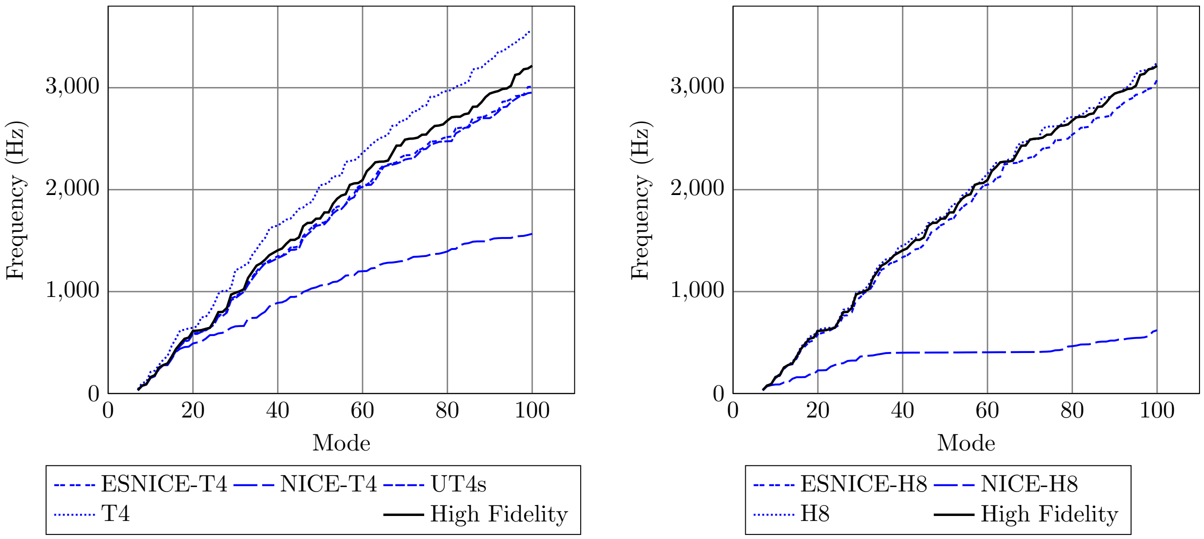

(a) Tetrahedral mesh

(b) Hexahedral mesh

Figure 5.18: Rectangular Plate (refinement level 2) - Frequency spectrum ($7-100$)

mesh. The coarsest meshes (refinement level 0) used in the convergence study are shown in Figure 5.24a) and Figure 5.24b). The mesh is refined by doubling the number of elements along each edge.

The frequency spectra obtained using ESNICE-T4, NICE-T4, T4 and UT4s elements are compared against the high fidelity spectrum at refinement level 3. The NICE-T4s give rise to spurious modes and this manifests as a flattened frequency spectrum as can be seen in Figure 5.25a. It can also be seen that the spectra obtained using ESNICE-T4 and UT4s elements match very closely with the high-fidelity spectrum showing the efficiency of the stabilization techniques. But we see later that the UT4s modes at the higher end of the spectrum are spurious for coarser meshes. We can also see that the spectrum computed using T4 elements predicts higher frequencies because of volumetric locking. The frequency spectrum using hexahedral elements is plotted in Figure 5.25b at refinement level 3. The NICE-H8s produce a spectrum far below the high-fidelity H20 spectrum because of the spurious modes. The ESNICE formulation effectively eliminates this spuriousness and produces a spectrum very close to that of the H20 elements over the broad range of frequencies considered. The H8 elements yield high frequencies,

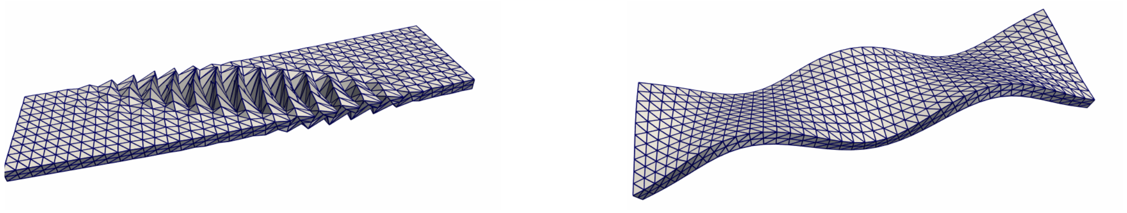

(a) NICE-T4 (b) ESNICE-T4

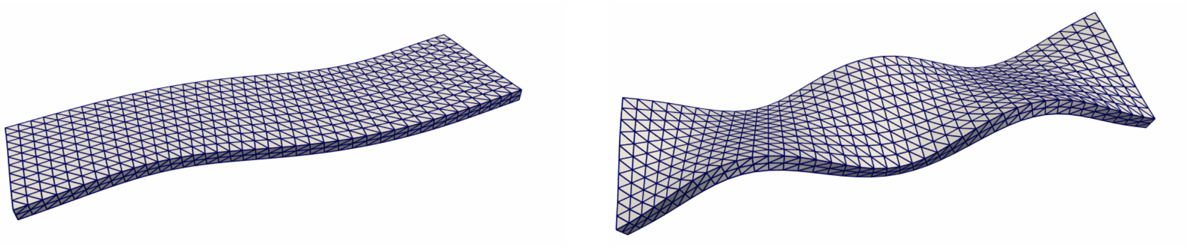

(c) T4 (d) UT4s

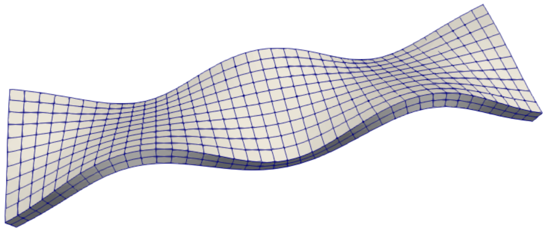

(e) H20

Figure 5.19: Rectangular Plate (Tetrahedral Mesh, refinement level 1) - Mode 15

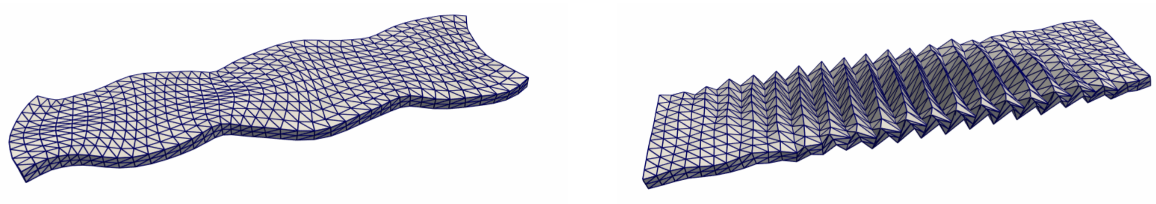

(a) ESNICE-T4 (b) UT4s

Figure 5.20: Rectangular Plate (Tetrahedral Mesh, refinement level 1) - Mode 93

as expected, because of volumetric locking (but they lock less than the T4 elements).

Figure 5.26 shows the convergence of frequencies at the lower end of the spectrum using all types of tetrahedral elements considered in this work. The T4 elements converge poorly because of the volumetric locking caused by using full integration when a nearly-incompressible material is dealt with. The NICE-T4s also show a poor convergence because of the spurious modes.

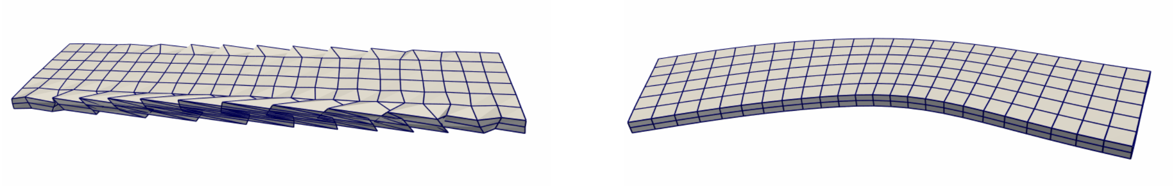

(a) NICE-H8 (b) ESNICE-H8

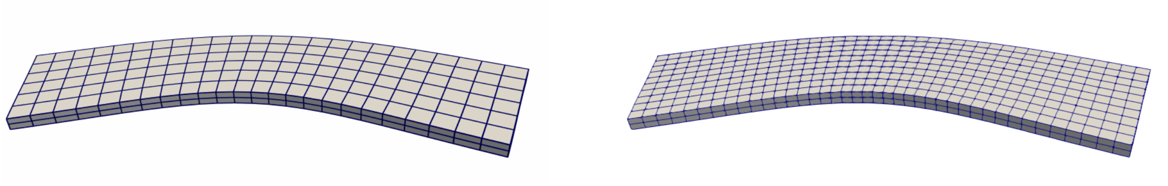

(c) H8 (d) H20

Figure 5.21: Rectangular Plate (Hexahedral Mesh, refinement level 1) - Mode 13

Spurious modes typically occur when nodal integration is used to resolve structures with higher volume-to-surface ratios. The ESNICE-T4 and UT4s elements are observed to be converging with almost the same convergence rate with the ESNICEs being marginally more accurate. This is because the stabilization used in both formulations is sufficient to curb spuriousness in the low frequency eigenmodes. The convergence of the NICE-H8s is very poor due to the presence of too many spurious modes (see Figure 5.27b). The convergence rate of H8 elements is poor as well, because of excessive volumetric stiffness (see Figure 5.27a). The ESNICE-H8s demonstrate good convergence (Figure 5.27c), because of being unaffected by both locking and spuriousness.

We show the mode shape of eigenmode 7 for tetrahedral elements (refinement level 2) in Figure 5.28 where we can see that the ESNICE-T4 and the UT4s elements match the mode shape obtained using H20 elements whilst the NICE-T4s yield a spurious mode (matching with the results from Puso and Solberg [57]). The stabilization curbs the spurious mode, as expected. Figure 5.28 also shows the eigenmode 7 using hexahedral elements. Again, the NICE-H8s yield a spurious mode and the ESNICE-H8s stabilize the formulation well and yield the physical mode. Figure 5.29 shows the mode shapes of eigenmode 72 where NICE-T4s produce a spurious mode and again, the ESNICE-T4s yield a physical mode which matches well with that produced by the H20 elements. The UT4s elements show spuriousness at this higher eigenmode because of

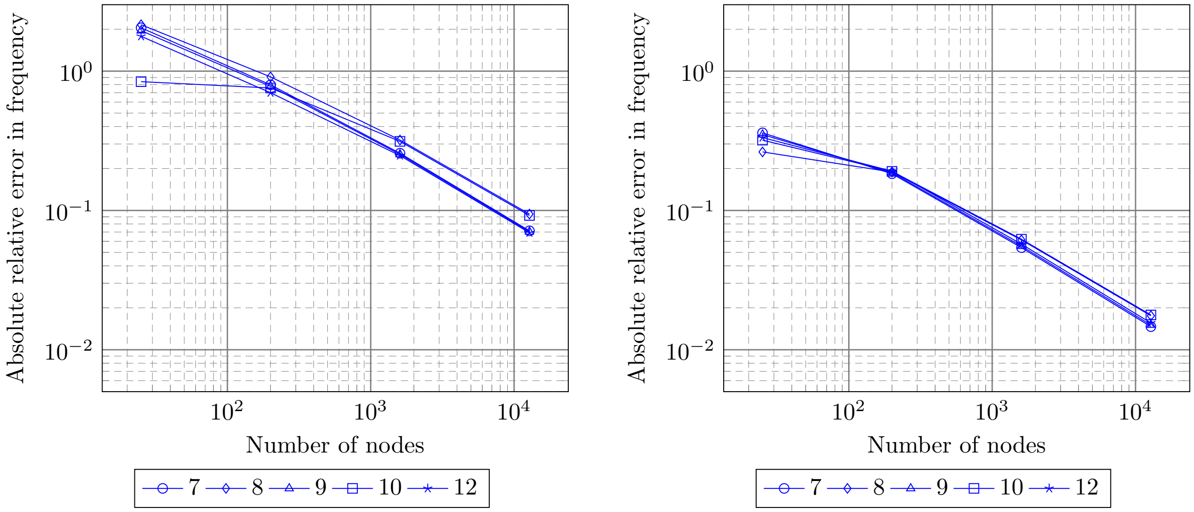

(a) T4 (b) NICE-T4

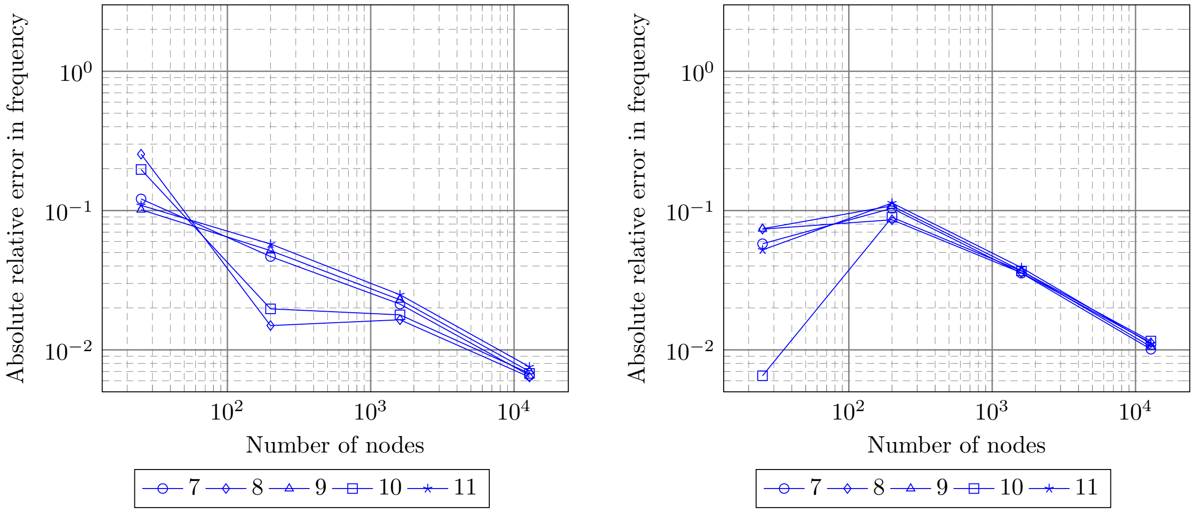

(c) ESNICE-T4 (d) UT4s

Figure 5.22: Rectangular Plate (Tetrahedral mesh) - Convergence of frequencies $(7-11)$

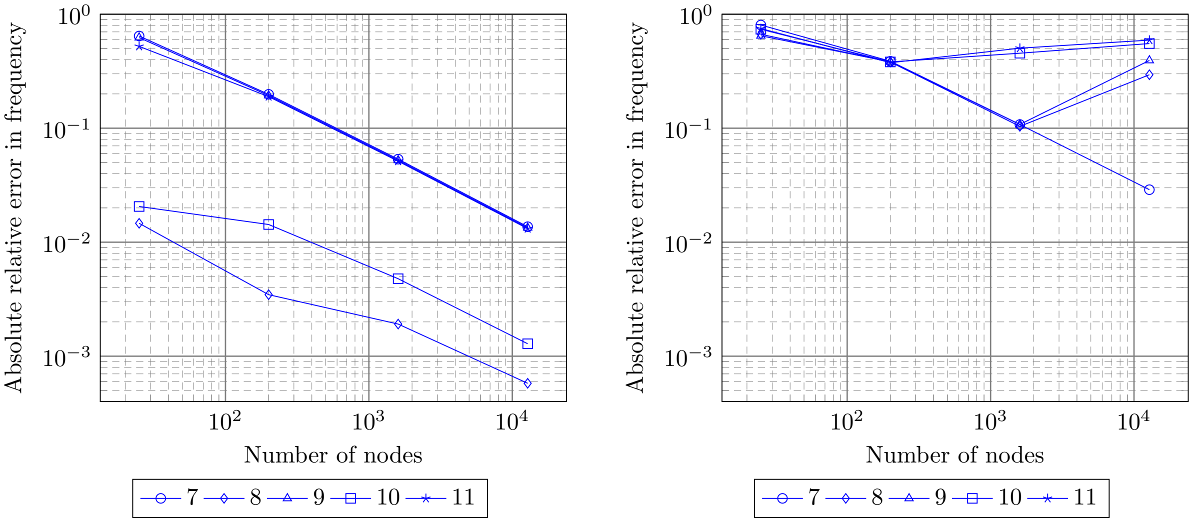

(a) H8

(b) NICE-H8

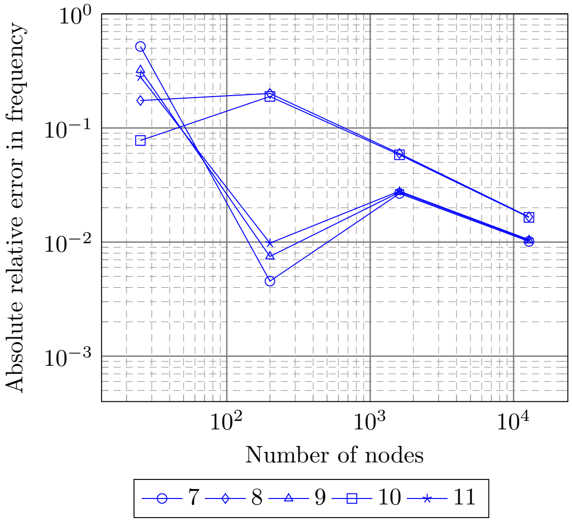

(c) ESNICE-H8

Figure 5.23: Rectangular Plate (Hexahedral mesh) - Convergence of frequencies $(7-11)$

the insufficient stabilization used. This example demonstrates the superiority of ESNICE-T4s in terms of the frequency spectrum and spuriousness over the T4, NICE-T4 and the UT4s elements. The ESNICE-T4s are observed to use a nodal stabilization factor closely around 0.1663 (rounded off) over the uniform mesh in this example. We wish to remind the reader that this value is not comparable with the 0.05 used by UT4s elements because of differences in the choice of the stabilization material. The (higher) eigenmode 70 is presented in Figure 5.30b to demonstrate that the ESNICE-H8s produce physical higher modes (cf. mode obtained using H20 mesh in Figure 5.30c), eliminating the spuriousness caused by nodal integration (Figure 5.30a). The stabilization factor is observed to be 0.7368 (rounded off) constant over the uniform hexahedral mesh, computed using Equation 5.7.

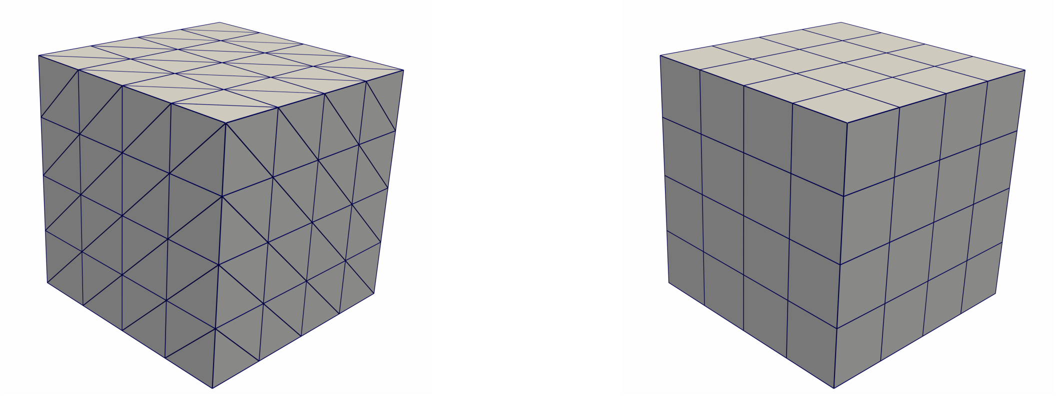
(a) Tetrahedral elements

(b) Hexahedral elements

Figure 5.24: Nearly-incompressible Cube - Coarsest Meshes (Refinement Level 0) used in convergence study

5.4.5 Thin square plate

A thin square plate ($10 \times 10 \times 0.05$ mm^3) is investigated for free vibration analysis without using any boundary conditions. This geometry is used in the NAFEMS FV12 example [63]. The Young's Modulus, Poisson's ratio and density of the material used are respectively 200 GPa, 0.3 and 8000 kg/m^3. We investigated the frequency spectrum of the ESNICEs by comparing with

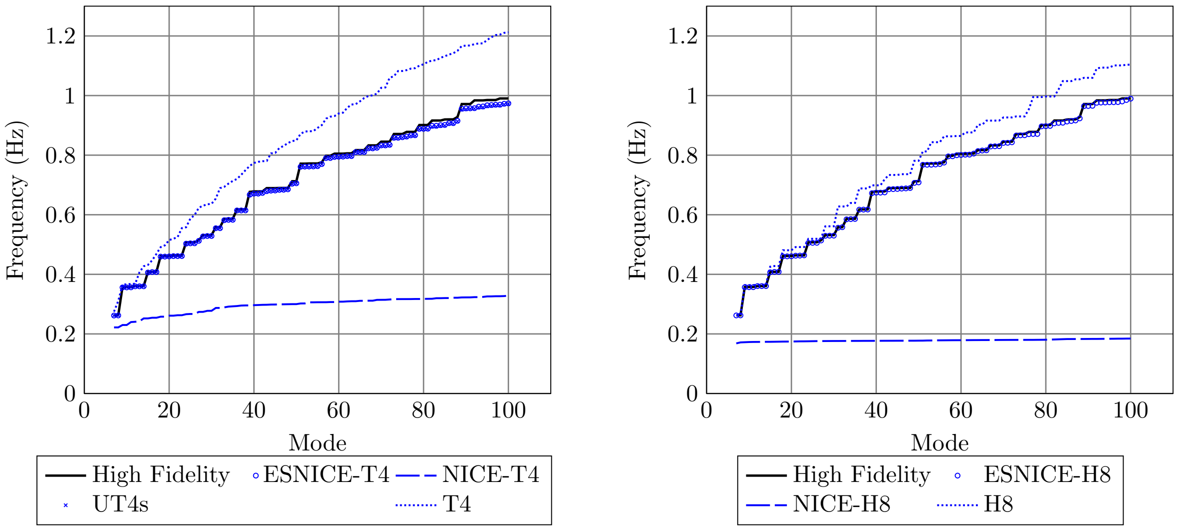

(a) Tetrahedral elements (b) Hexahedral elements

Figure 5.25: Nearly-incompressible Cube (refinement level 3) - Frequency spectrum $(7-100)$

frequencies computed using a fine H27-based (high fidelity) analysis. The coarsest tetrahedral and hexahedral meshes used in convergence study are shown in Figure 5.31. The mesh is refined by doubling the number of elements along the three Cartesian directions.

The frequency spectra (modes $7-14$) obtained using ESNICE-T4, NICE-T4, T4 and UT4s elements are compared against high fidelity spectrum in Figure 5.32a at refinement level 3. The T4 elements use full integration, and so are severely affected by shear locking (since the elements are very thin). This leads to computing exaggerated structural stiffness and the frequencies are overestimated. The NICE-T4 formulation is able to produce physical modes when the surface-to-volume ratio of the structure in question is large, as explained in Section 5.1. We can observe that the NICE-T4s and ESNICE-T4s yield frequency spectra very close to the high fidelity frequencies. This is because the ESNICE formulation adds just enough amount of stabilization and since not much stabilization is required in this example, ESNICE-T4s produce very similar spectrum to that of NICE-T4s, with the frequencies estimated by ESNICE-T4s being marginally more accurate. The UT4s formulation does not use the element aspect ratio to decide on the stabilization factor, and when a factor of 0.05 is used for stabilization, the structural

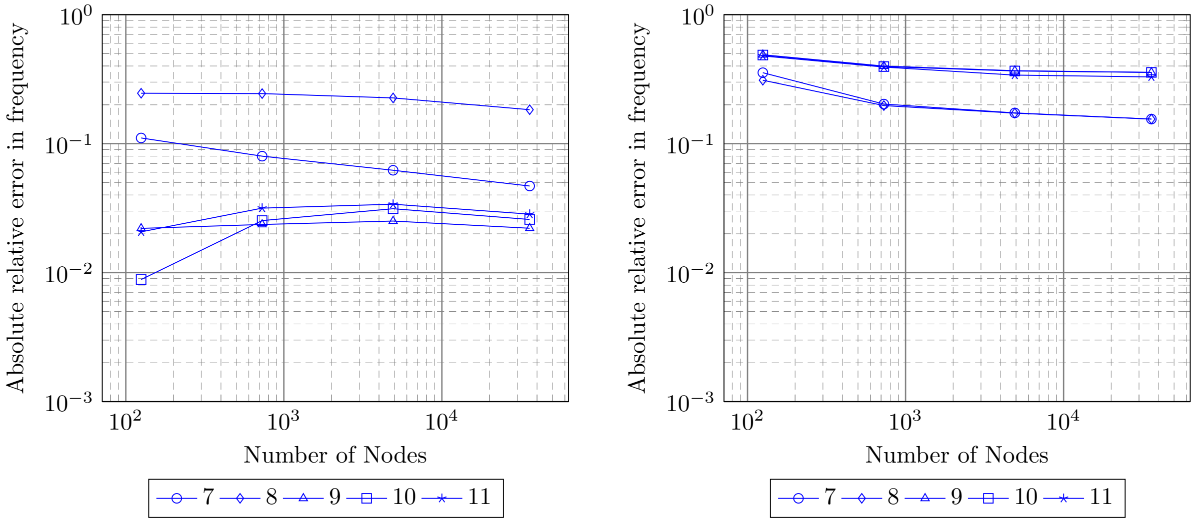

(a) T4 (b) NICE-T4

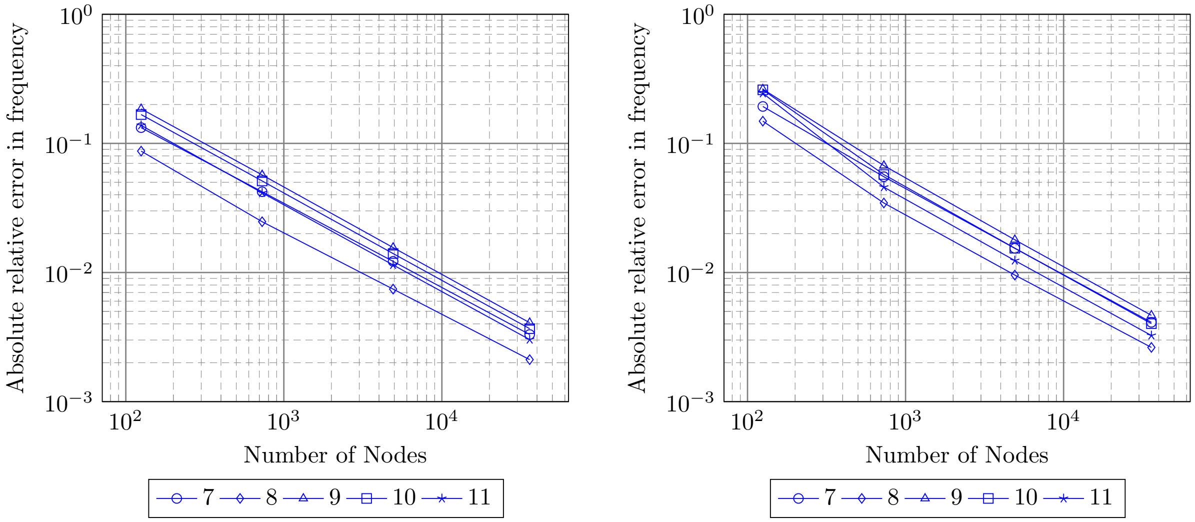

(c) ESNICE-T4 (d) UT4s

Figure 5.26: Nearly-incompressible Cube (Tetrahedral mesh) - Convergence of frequencies $(7-11)$

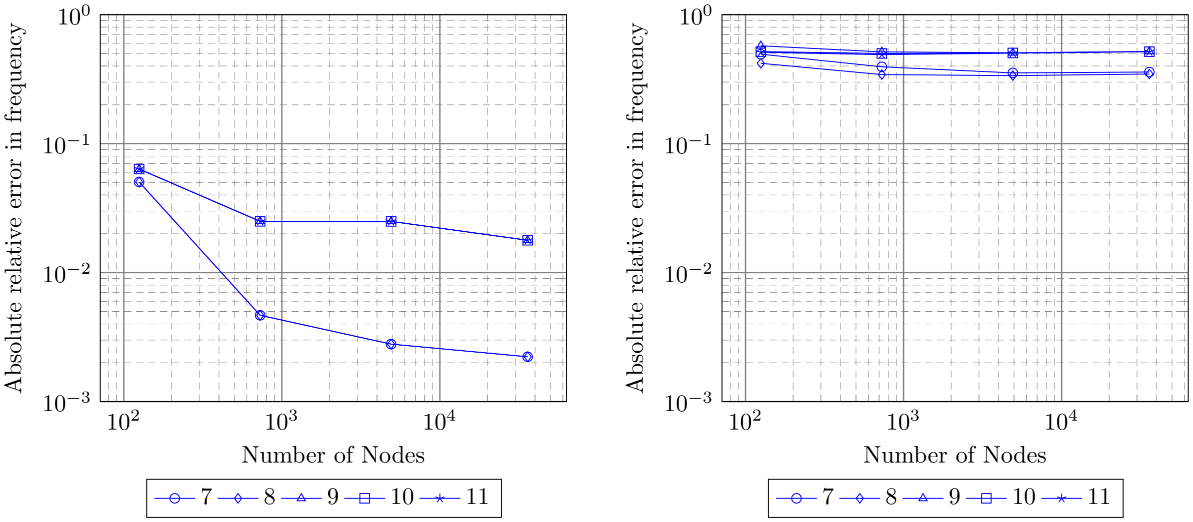

(a) H8 (b) NICE-H8

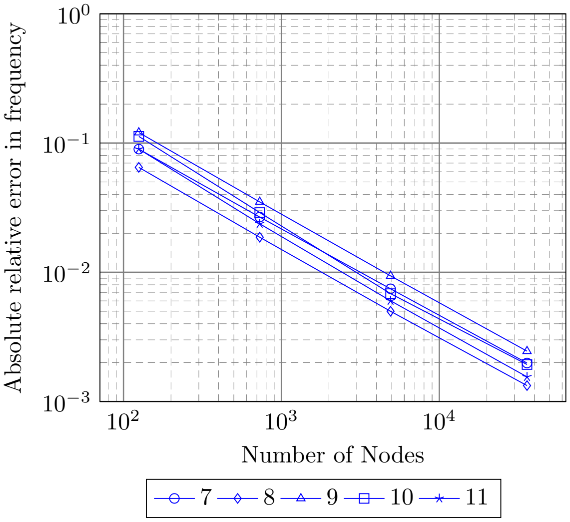

(c) ESNICE-H8

Figure 5.27: Nearly-incompressible Cube (Hexahedral mesh) - Convergence of frequencies $(7-11)$

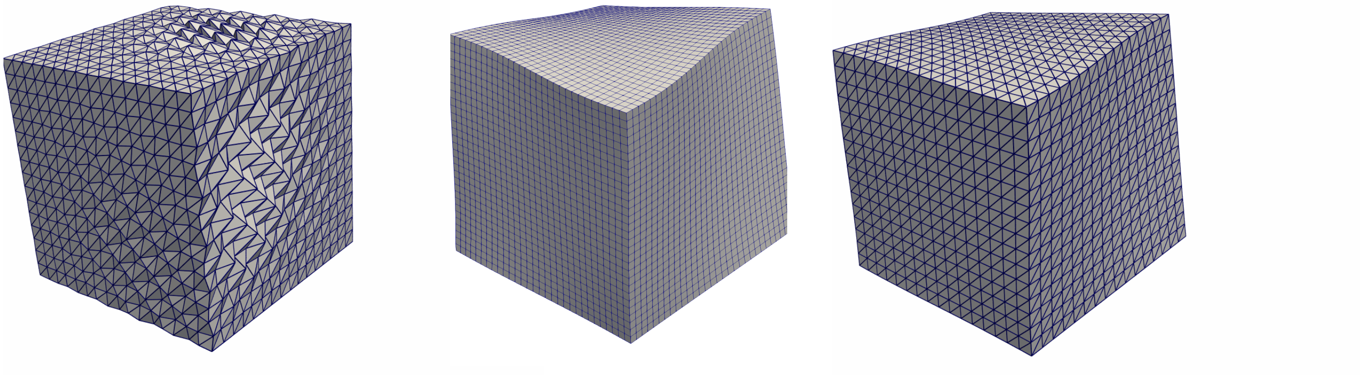

(a) NICE-T4 (b) H20 (c) ESNICE-T4

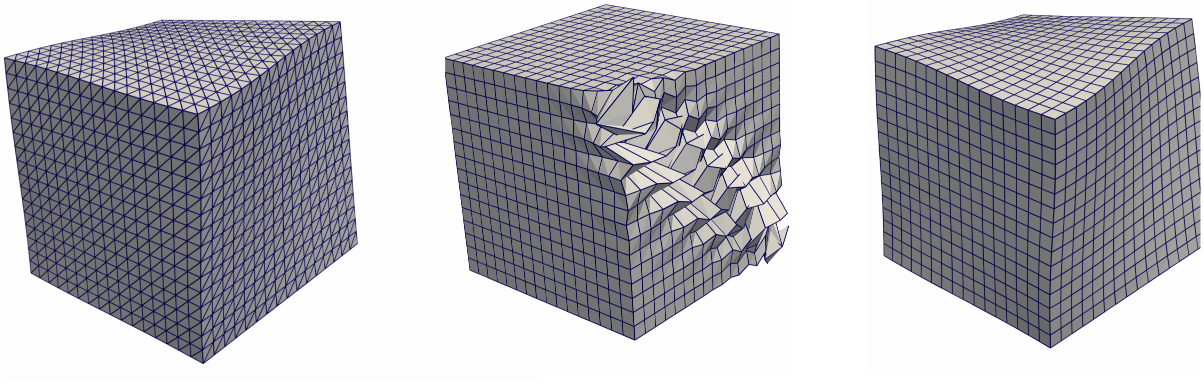

(d) UT4s (e) NICE-H8 (f) ESNICE-H8

Figure 5.28: Nearly-Incompressible Cube (refinement level 2) - Mode 7

stiffness is very exaggerated. This leads to overestimated UT4s-based frequencies as seen in Figure 5.32a. The frequency spectra of the ESNICE-H8, NICE-H8 and H8 elements are compared against the high fidelity frequencies in Figure 5.32b. The H8 elements produce stiff modes due to shear locking and thus overestimate the eigenvalues (and so, the frequencies). The NICE-H8s yield spurious modes, and so the spectrum can be seen below the high fidelity spectrum. The ESNICE-H8s add the right amount of stabilization and the spectrum obtained matches with the high fidelity frequencies.

The shear locking undergone by T4 elements is also manifested as large errors in the convergence plot (Figure 5.33a). The NICE-T4s and ESNICE-T4s produce physical modes 7 – 14 which can also be seen from the similarity in their convergence plots (compare Figure 5.33b and

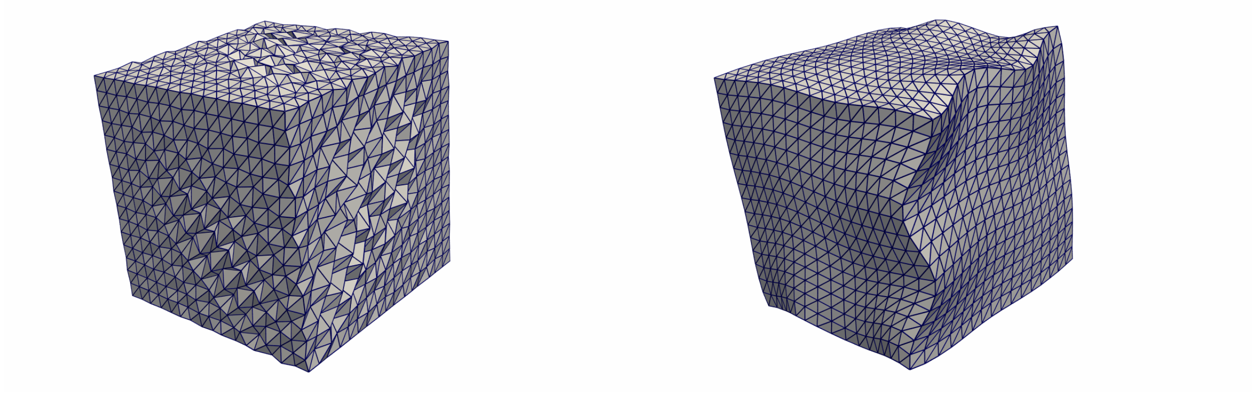

(a) NICE-T4 (b) ESNICE-T4

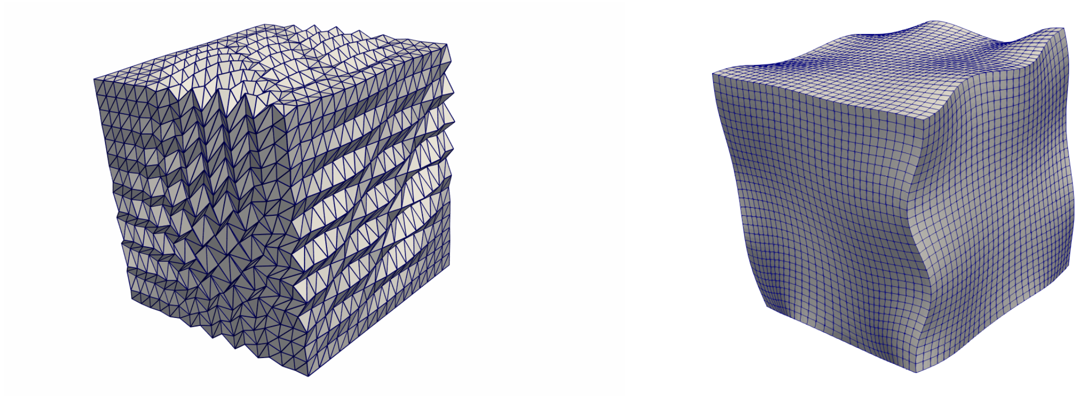

(c) UT4s (d) H20

Figure 5.29: Nearly-Incompressible Cube (refinement level 2, Tetrahedral mesh) - Mode 72

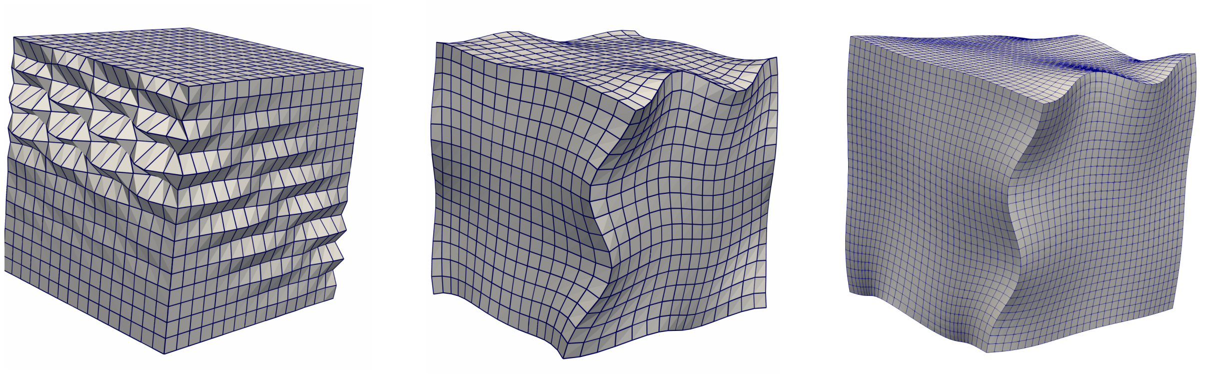

(a) NICE-H8 (b) ESNICE-H8 (c) H20

Figure 5.30: Nearly-incompressible Cube (refinement level 2, Hexahedral mesh) - Mode 70

Figure 5.33c). Since the material used is compressible, the stabilization material used by UT4s and ESNICE-T4 formulations are similar except for the stabilization factors. We can observe that the errors in frequency spectrum obtained using UT4s formulation (see convergence plot 5.33d) is higher than that produced by NICE-T4 (Figure 5.33b) and ESNICE-T4 (Figure 5.33c) formulations because the UT4s formulation uses $\Gamma = 0.05$ and induces shear locking for the mesh used in this example. Just as in the case of fully integrated tetrahedral elements, the quality of frequencies estimated using H8 elements is poor, as seen in the convergence plot shown in Figure 5.34a. The NICE-H8s are observed to exhibit spuriousness leading to poor convergence (see Figure 5.34b). The convergence of ESNICE-H8s (Figure 5.34c) show a decrease in error of the frequency estimates. The increase in error of a couple of frequency estimates is due to the predicted frequencies transitioning from convergence from above to below (or vice-versa) of the high fidelity spectrum.

The mode shape of eigenmode 14 is shown in Figure 5.35 using ESNICE-T4, NICE-T4, UT4s, T4 and H20 elements. The NICE-T4s do not exhibit spuriousness in this example, and so the mode shape produced by NICE-T4s (Figure 5.35a) and ESNICE-T4s (Figure 5.35c) match very well with that of H20 (Figure 5.35e) elements. The T4 elements produce a stiff mode (Figure 5.35b) due to shear locking and thus the mode shape produced looks very different from that obtained using H20 elements. The UT4s formulation produces stiffer modes (less stiff than T4 elements) because of the over-stabilization. This leads to a slightly stiff eigenmode 14 produced by the UT4s formulation as shown in Figure 5.35d. This highlights that the amount of stabilization added should be neither too high nor too low. In this example, the fully integrated stiffness matrix is marked by heavy shear locking, so we expect the stabilization factor to be very small to get rid of the artificial bending stiffness. Since the mesh used is uniform, the stabilization factor used by ESNICE-T4 formulation is computed to be closely around 0.00116 for all the elements, which is very different from the 0.05 used by UT4s formulation.

The mode shape of eigenmode 10 is shown in Figure 5.36 using NICE-H8, ESNICE-H8, H8 and H20 elements. The NICE-H8s produce a spurious mode whilst the ESNICE-H8s produce a physical mode matching well with that produced by H20 elements. The H8 elements produce a mode shape similar to that of H20 elements despite the locking. The ESNICE-H8s use a stabilization factor of 0.00646 (rounded off) constant over all the elements which proves to be just enough to curb the spuriousness caused by nodal integration. This example also indicates that NICE-H8s are more prone to spuriousness than NICE-T4s, possibly because of the bilinear strains used by hexahedral elements.

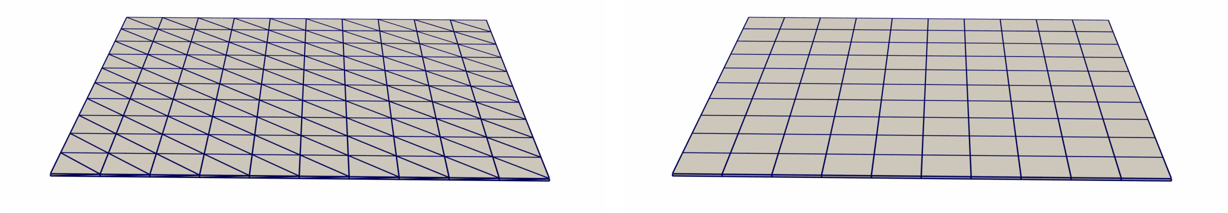

(a) Tetrahedral elements

(b) Hexahedral elements

Figure 5.31: Thin Square Plate - Coarsest Meshes (Refinement Level 0) used in convergence study

5.4.6 Curved Cantilever

We consider a curved cantilever beam made of nearly incompressible material. The isotropic material used has the properties $E = 1$ MPa, $\nu = 0.499$, density $\rho = 1$ kg/m^3. We

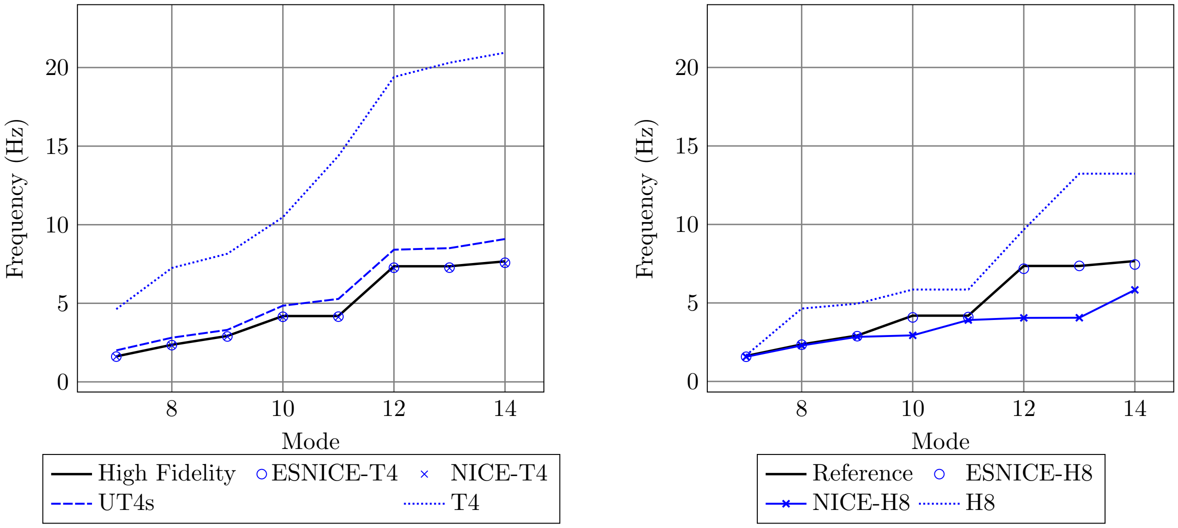

(a) Tetrahedral elements

(b) Hexahedral elements

Figure 5.32: Thin Square Plate (refinement level 3) - Frequency spectrum $(7-14)$

analyze a couple of mode shapes (lower and higher eigenmodes) for this structure using ESNICE-T4, NICE-T4, UT4s, ESNICE-H8, NICE-H8 and H20 elements.

We show the mode shapes of eigenmode 8 when ESNICE-T4, NICE-T4, UT4s and H20 elements are used in 5.37. The NICE-T4s exhibit spuriousness without using any stabilization. This spuriousness is observed to be eliminated by using UT4s 5.37d and ESNICE-T4 5.37c formulations. The modeshapes obtained using UT4s and ESNICE-T4 elements is observed to match well with that obtained using H20 elements (5.39a) The UT4s stabilization is observed to be insufficient for higher eigenmodes. The mode shapes of eigenmode 130 are shown in 5.38 using different tetrahedral elements. The UT4s elements exhibit spuriousness besides NICE-T4s because of the insufficient stabilization used. The ESNICE formulation uses the aspect ratio dependent stabilization and is observed to obtain a physical eigenmode matching well with that of H20 elements 5.38a. This behavior is reflected in the plot of frequency spectrum comparison in 5.41a. The spectrum from NICE-T4s starts flattening out (because of the spurious low-energy modes) very early in the spectrum. At about mode-130, the UT4s spectrum starts exhibiting spurious modes which is associated with the flattening out of the spectrum. The ESNICE-T4s

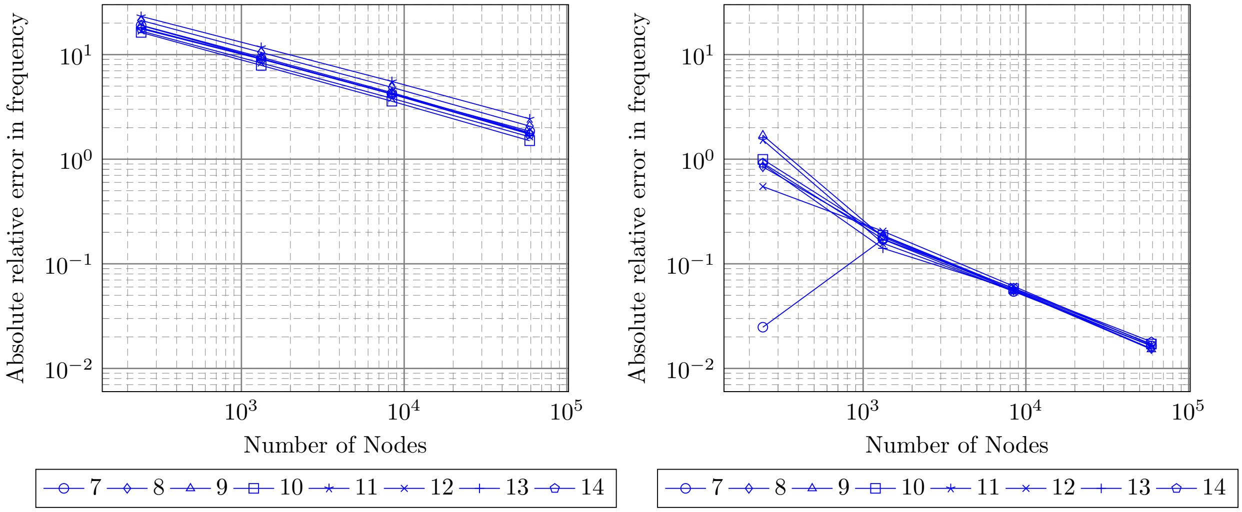

(a) T4 (b) NICE-T4

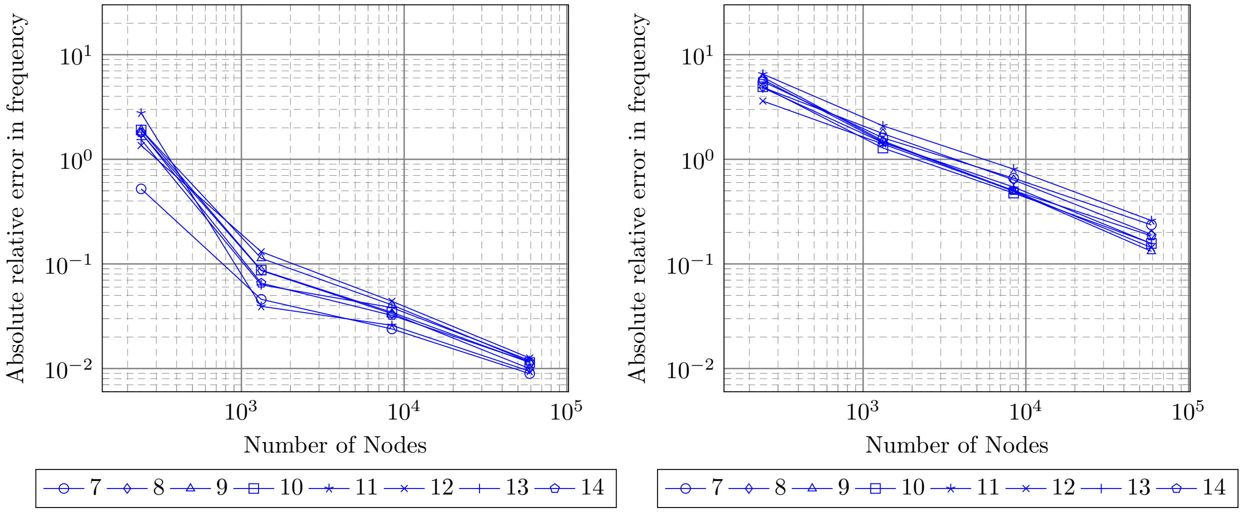

(c) ESNICE-T4 (d) UT4s

Figure 5.33: Thin Square Plate (Tetrahedral mesh) - Convergence of frequencies $(7-14)$

produce a spectrum close to the H20 spectrum because of the sufficient amount of stabilization added. We observed that the stabilization factor for this example using the chosen mesh is in the range $[0.1064, 0.1651]$ (rounded-off). The T4 spectrum overestimates the frequencies greatly because of volumetric locking.

Similar analyses as that of tetrahedral elements is done using a hexahedral mesh using ESNICE-H8, NICE-H8 and H20 elements. The NICE-H8s again exhibit spuriousness very early in the spectrum at mode-3 5.39b. This can be effectively curbed using energy-sampling

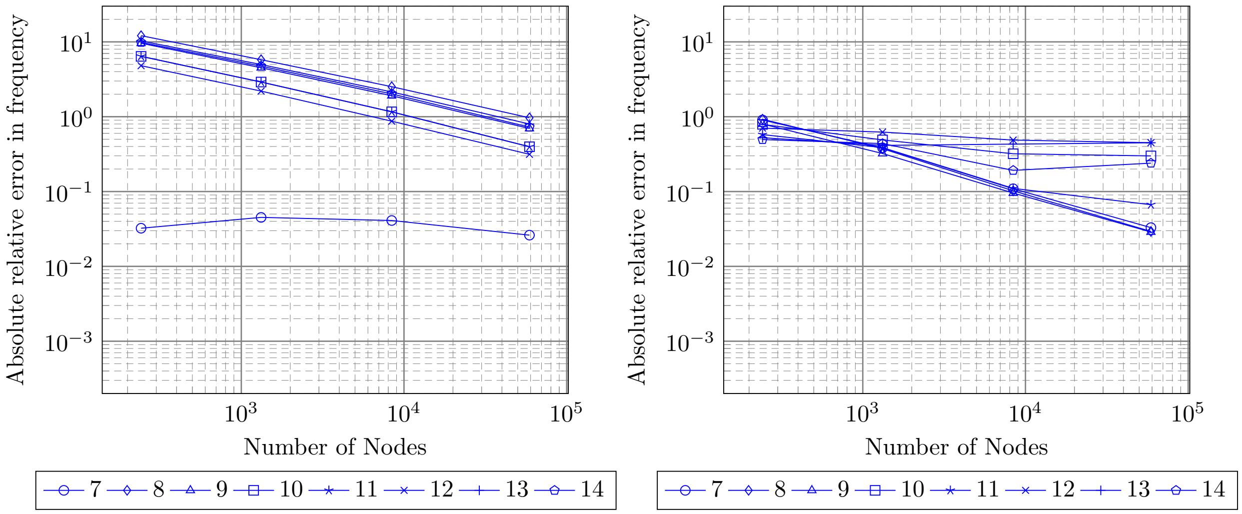

(a) H8 (b) NICE-H8

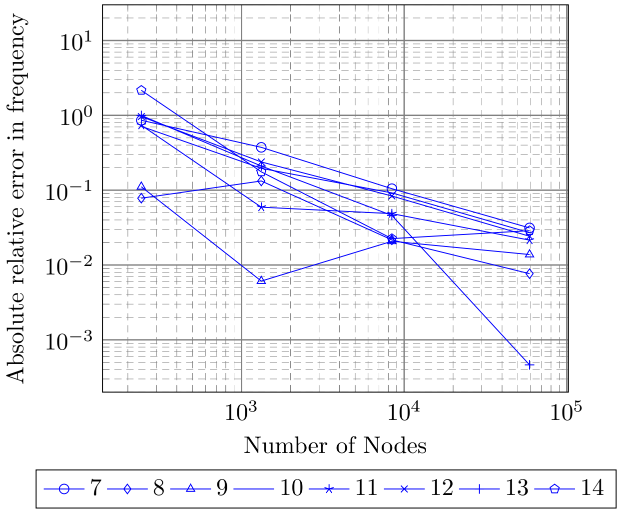

(c) ESNICE-H8

Figure 5.34: Thin Square Plate (Hexahedral mesh) - Convergence of frequencies $(7-14)$

stabilization as seen in 5.39c. The mode shape obtained using ESNICE-H8s is also observed to match well with that obtained using H20 elements 5.37a. 5.40 shows eigenmode 85 to show that ESNICE-H8s produce a nonspurious higher eigenmode 5.40c which matches with the eigenmode produced by H20 elements 5.40a whilst the NICE-H8s produce a spurious mode 5.40b which is not a surprise. The comparison of frequency spectra using these hexahedral element formulations is shown in 5.41b. The NICE-H8s show almost a horizontal line as the frequency spectrum because of the numerous spurious (low-energy) modes. The ESNICE-H8s produce a spectrum

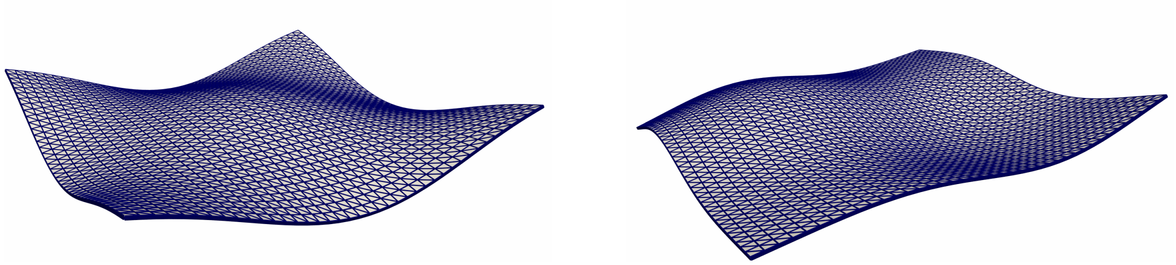

(a) NICE-T4 (b) T4

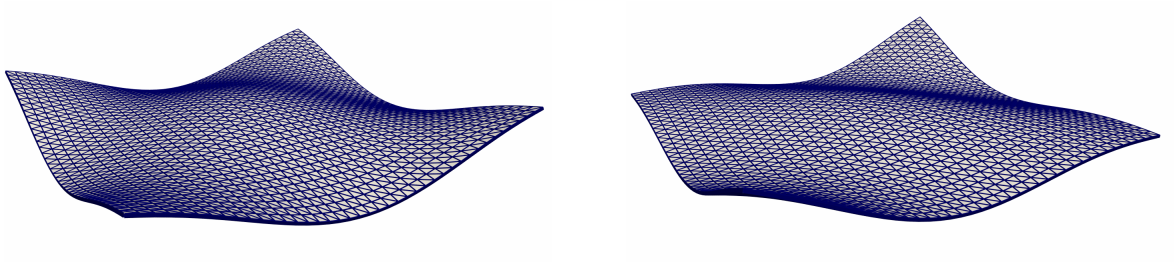

(c) ESNICE-T4 (d) UT4s

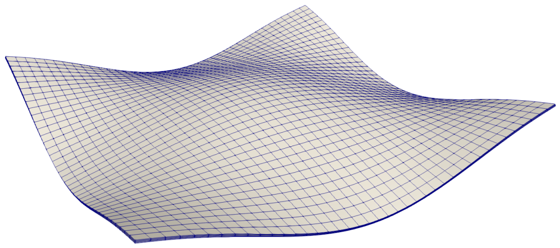

(e) H20

Figure 5.35: Thin Square Plate (Tetrahedral mesh, refinement level 2) - Mode 14

with non-spurious modes which closely matches the H20-based spectrum. The H8 elements produce a stiff spectrum as a result of volumetric locking. The stabilization factor the ESNICE-H8 elements used is observed to be in the range $[0.5131, 0.7296]$ (rounded-off) in this example.

5.4.7 Axle Bracket

This example demonstrates the effectivity of ESNICE formulation using free vibration analyses of an axle bracket. This kind of bracket is ubiquitously used for holding rotating shafts. The bracket is made of steel with Young's modulus, Poisson's ratio and density 210 GPa, 0.3 and 7850 $\mathrm{kg/m^3}$ respectively. The two holes on either side of the axle mount are constrained. The

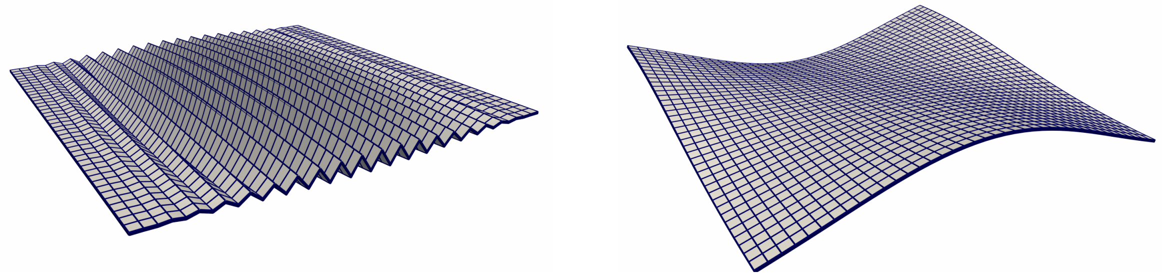

(a) NICE-H8 (b) ESNICE-H8

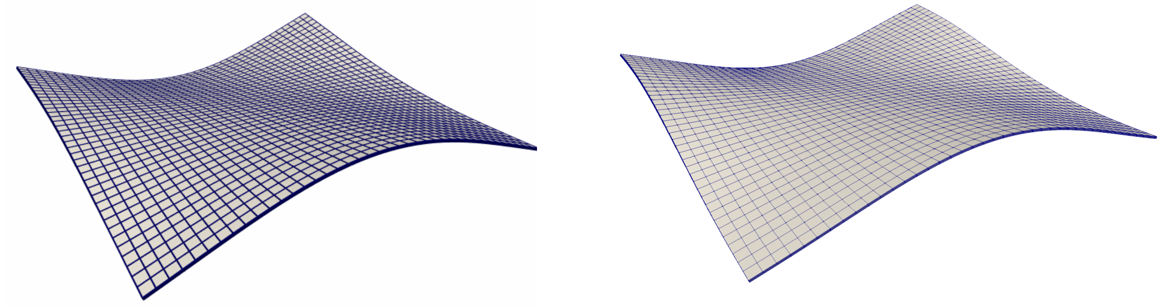

(c) H8 (d) H20

Figure 5.36: Thin Square Plate (Hexahedral mesh, refinement level 2) - Mode 10

ESNICE formulation is investigated using both tetrahedral and hexahedral elements.

Figure 5.42a shows the frequency spectrum obtained using ESNICE-T4, NICE-T4, UT4s, T4 and T10 elements. The NICE-T4 spectrum flattens out after a few modes because of the spurious modes. The UT4s spectrum flattens out after some physical lower frequency eigenmodes because of under-stabilization leading to spuriousness. The T4 elements undergo some shear locking and so the spectrum produced is slightly above the T10-based spectrum. The frequency spectrum obtained using hexahedral elements H8, ESNICE-H8, NICE-H8 and H20 elements is shown in Figure 5.42b. The H8 elements undergo negligible locking and so the spectrum matches well with the H20-based frequency spectrum. The NICE-H8s show spuriousness in the very early modes whilst the ESNICE-H8s successfully produce physical modes and the spectrum matches well with the H20-based frequency spectrum.

The eigenmode 24 obtained using the tetrahedral elements is shown in Figure 5.43. The NICE-T4s yield a spurious eigenmode which is effectively stabilized by both ESNICE-T4 and

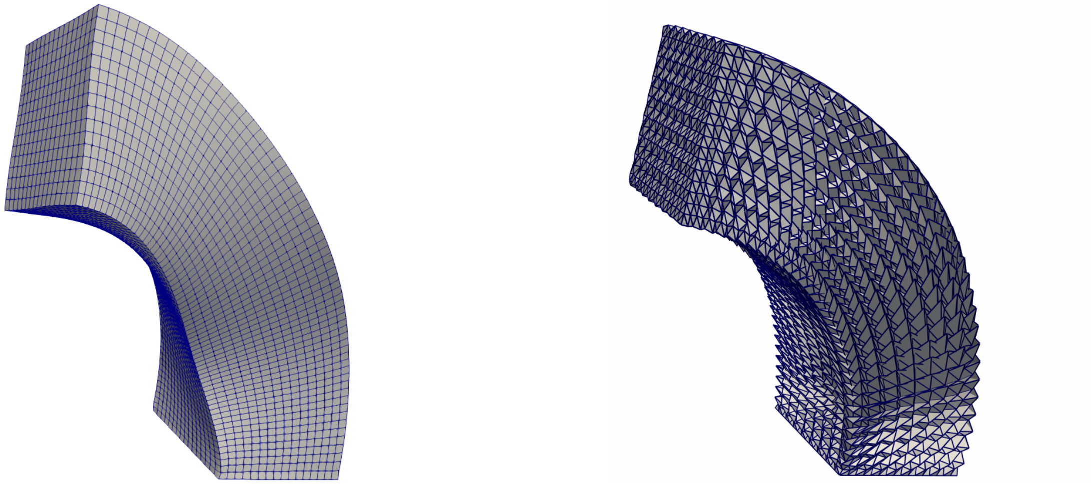

(a) H20 elements (b) NICE-T4 elements (No stabilization)

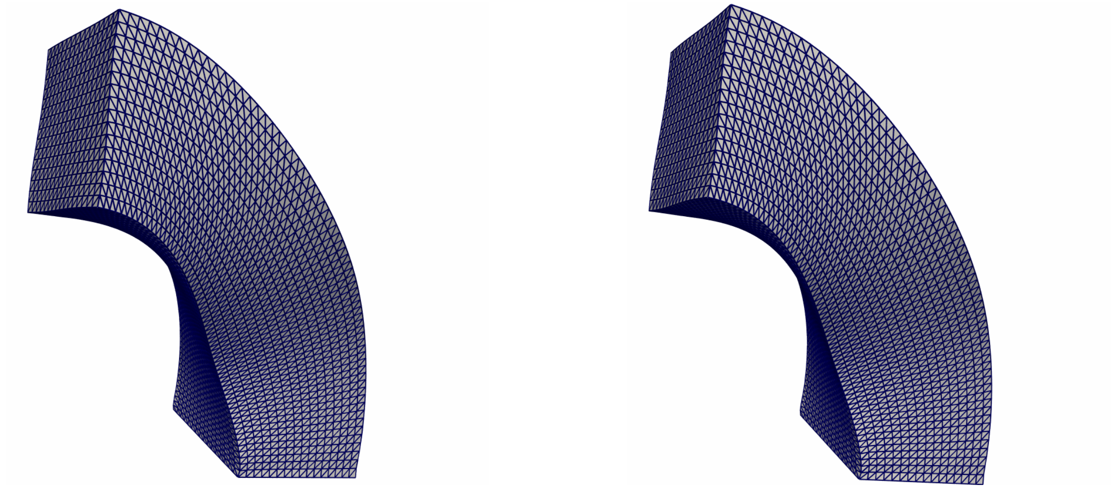

(c) ESNICE-T4 elements (d) UT4s elements

Figure 5.37: Curved Cantilever Beam (Tetrahedral mesh) - Mode 8

UT4s (0.05 stabilization factor) formulations. The obtained physical eigenmode 24 also matches well with that produced by T10 elements. We note that the eigenvalue estimated using ESNICE-T4s and UT4s elements is close to the 23rd eigenvalue estimated by T10s and so the comparison is done using eigenmode 23 produced by T10 elements. We observe that UT4s formulation yields spurious higher frequency eigenmodes and we show eigenmode 69 (Figure 5.44c) as an example. The NICE-T4s exhibit spuriousness as expected, whilst the ESNICE-T4s produce a physical mode matching with that produced by T10s. We compared the 69th eigenmodes

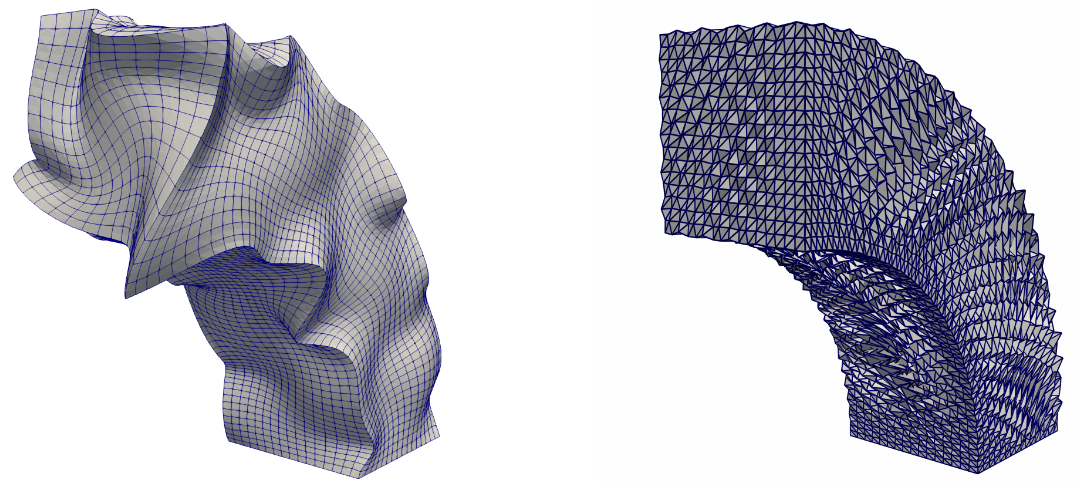

(a) H20 elements

(b) NICE-T4 elements (No stabilization)

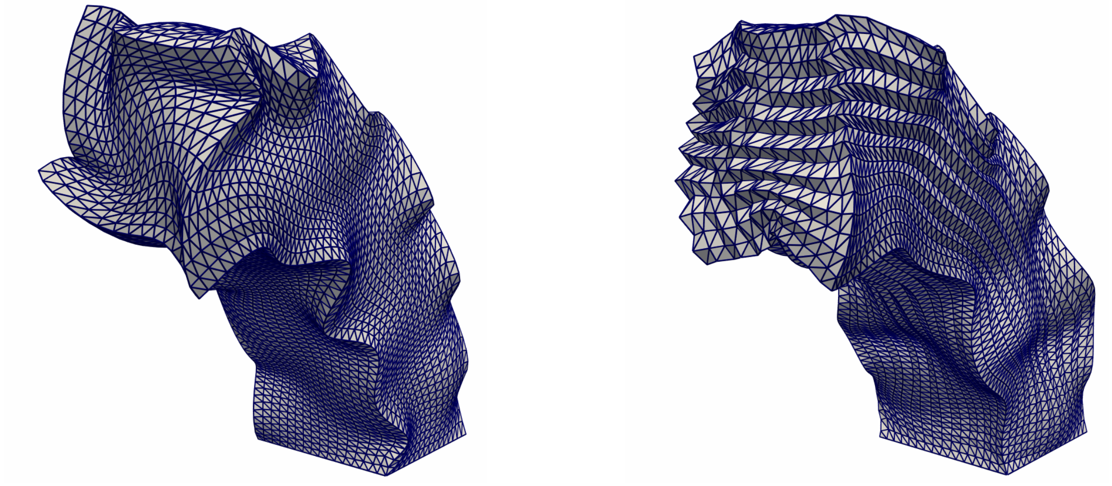

(c) ESNICE-T4 elements

(d) UT4s elements

Figure 5.38: Curved Cantilever Beam (Tetrahedral mesh) - Mode 130

with the 67th mode produced by T10s because of matching eigenvalues. The matrix norm used for stabilization for UT4s and ESNICE formulations is the similar for this example and so the stabilization factors are comparable. The nodal stabilization factors computed using ESNICE formulation in this example lie in the range $[0.073, 0.286]$ as compared to UT4s formulation which uses constant stabilization throughout the mesh. This exemplifies the importance of using nonuniform stabilization and demonstrates that the stabilization computed using energy-sampling is very effective in ameliorating spurious modes.

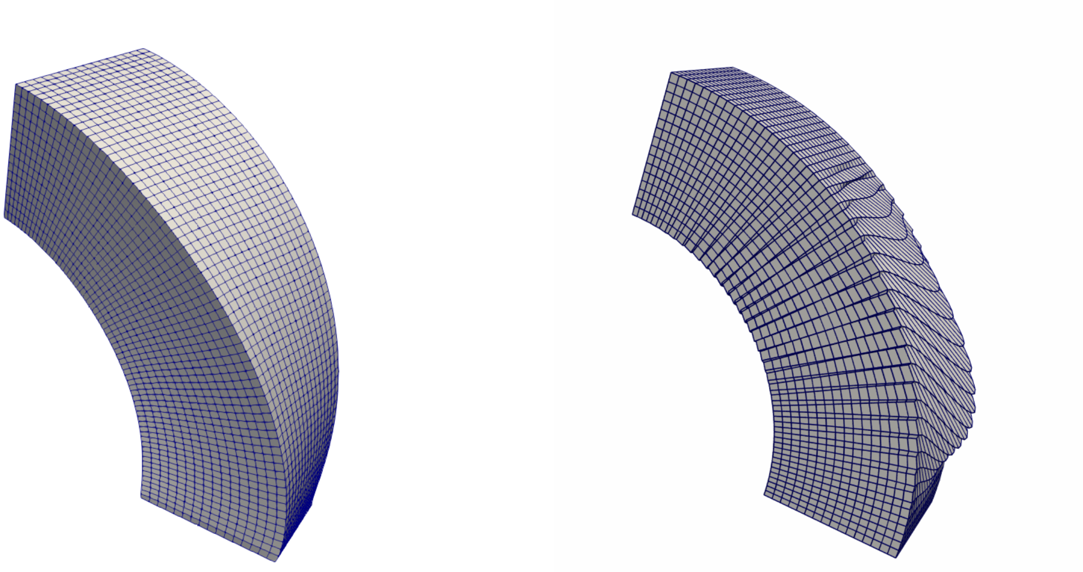

(a) H20 elements

(b) NICE-H8 elements (No stabilization)

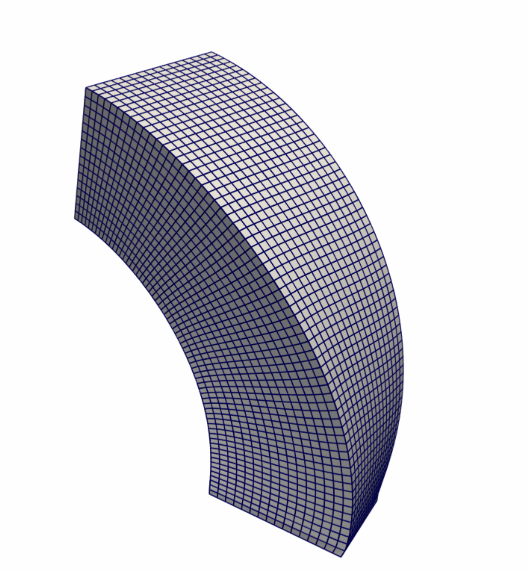

(c) ESNICE-H8 elements

Figure 5.39: Curved Cantilever Beam (Hexahedral mesh) - Mode 3

The eigenmode 10 and eigenmode 50 produced by NICE-H8s and ESNICE-H8s are compared against H20-based eigenmodes in Figure 5.45 and Figure 5.46 respectively. We observe that the spuriousness of eigenmodes produced by the NICE formulation is effectively eliminated using energy sampling-based ESNICE formulation. The ESNICEs produce modes which match well with those produced by H20 elements. The range of nodal stabilization factors computed

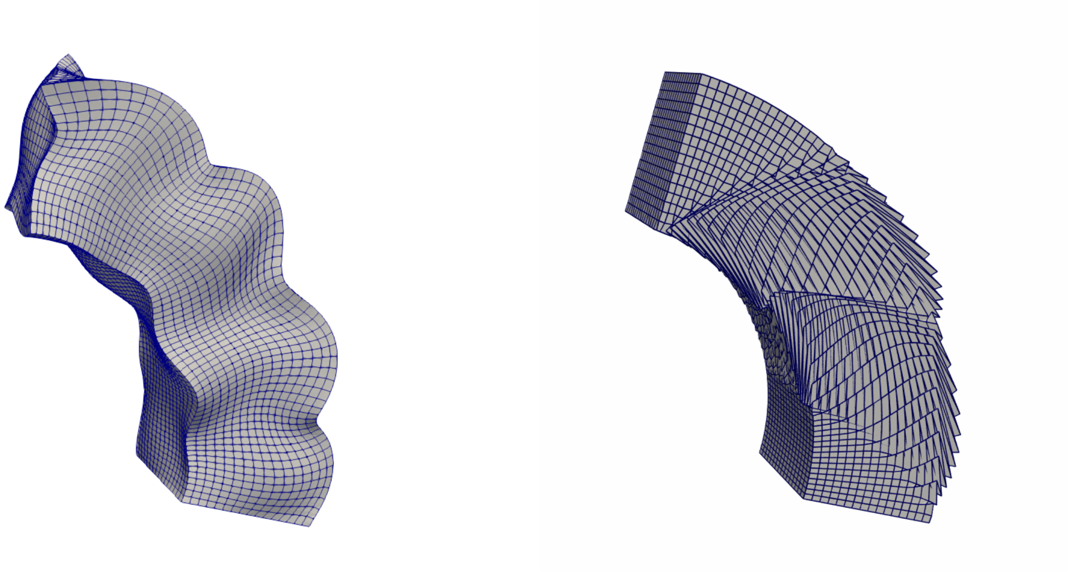

(a) H20 elements (b) NICE-H8 elements (No stabilization)

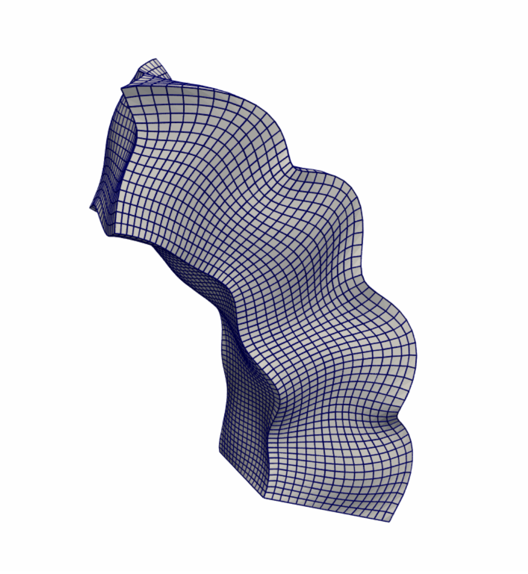

(c) ESNICE-H8 elements

Figure 5.40: Curved Cantilever Beam (Hexahedral mesh) - Mode 85

using the energy-sampling technique is observed to be $[0.3773, 0.7131]$.

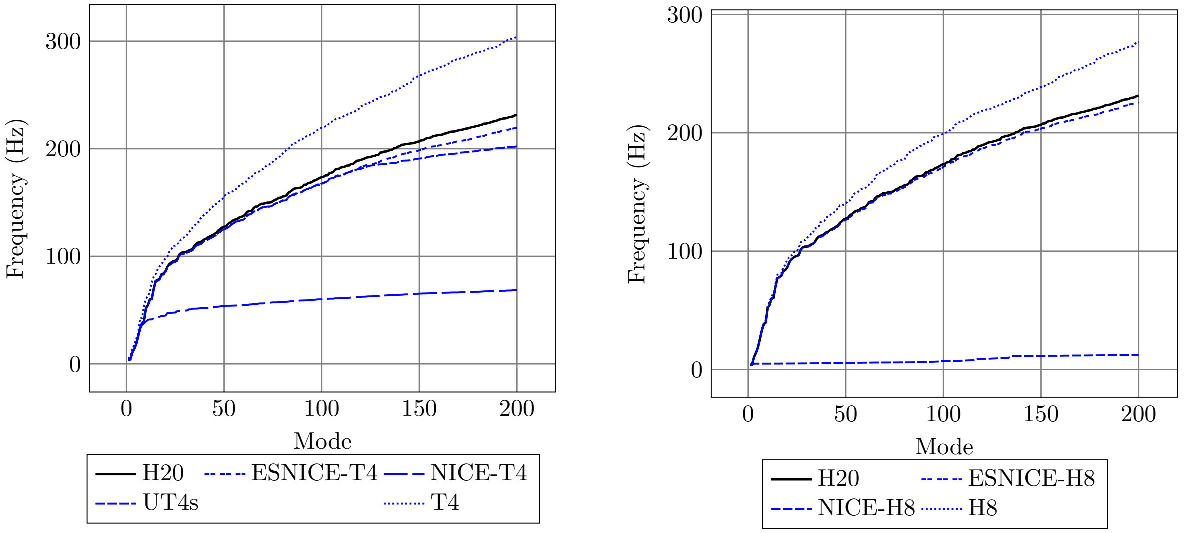

(a) Tetrahedral elements

(b) Hexahedral elements

Figure 5.41: Curved Cantilever Beam - Frequency Spectrum ($[1,200]$)

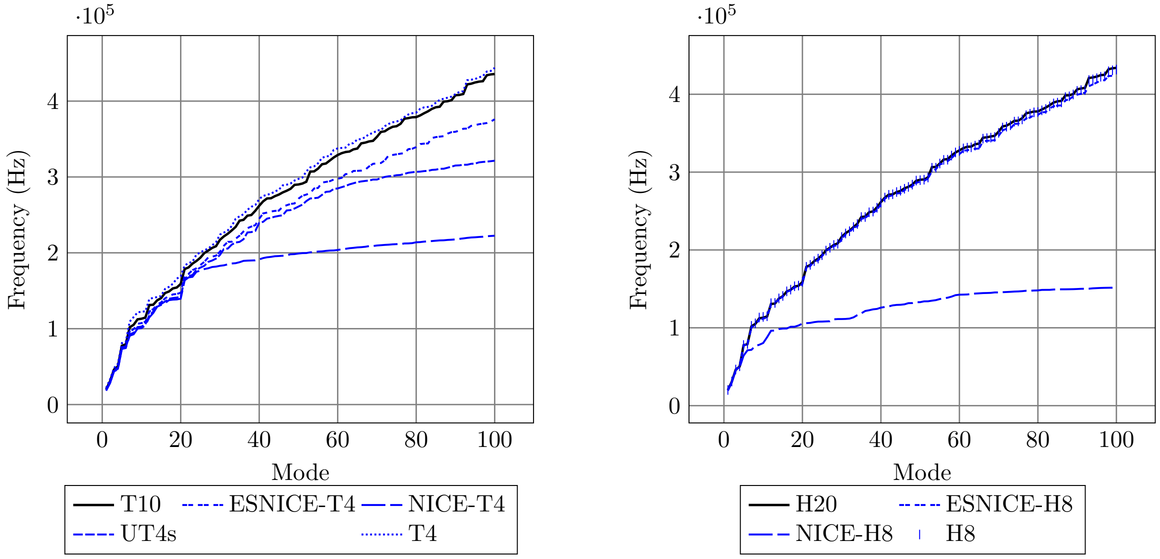

(a) Tetrahedral elements

(b) Hexahedral elements

Figure 5.42: Axle Bracket - Frequency spectrum ($1-100$)

5.5 The infsup test

The NICE formulation was subject to the numerical infsup test [51]. The formulation was found free of volumetric locking, but contrary to the statement in the Reference [51], the formulation does not pass the test: there are pressure modes, which have been overlooked in the

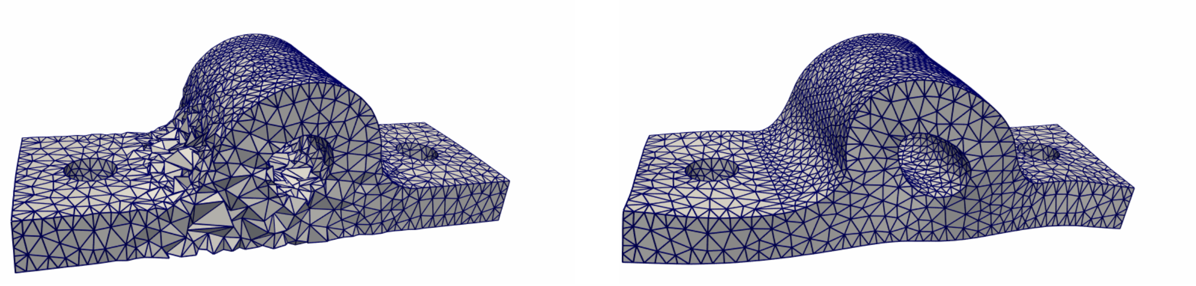

(a) NICE-T4

(b) ESNICE-T4

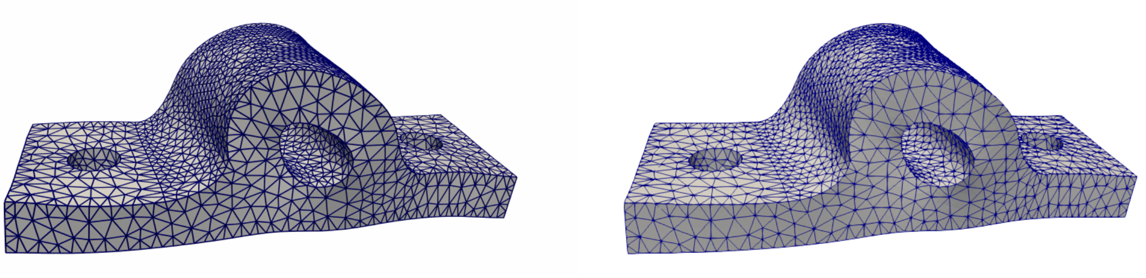

(c) UT4s

(d) T10

Figure 5.43: Axle Bracket (Tetrahedral mesh) - Mode 24

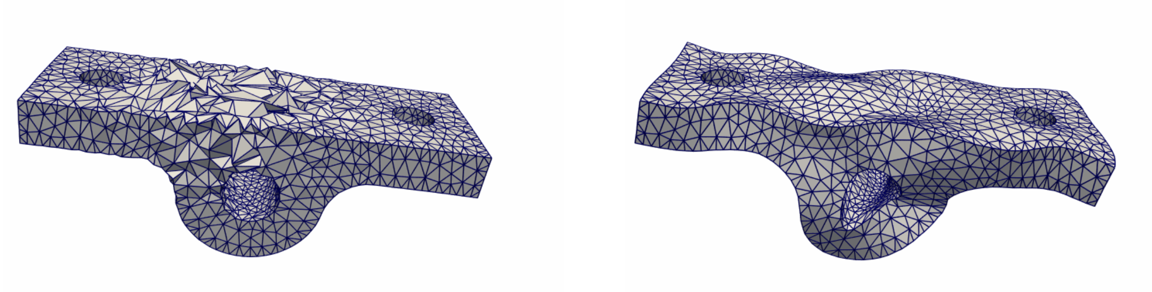

(a) NICE-T4

(b) ESNICE-T4

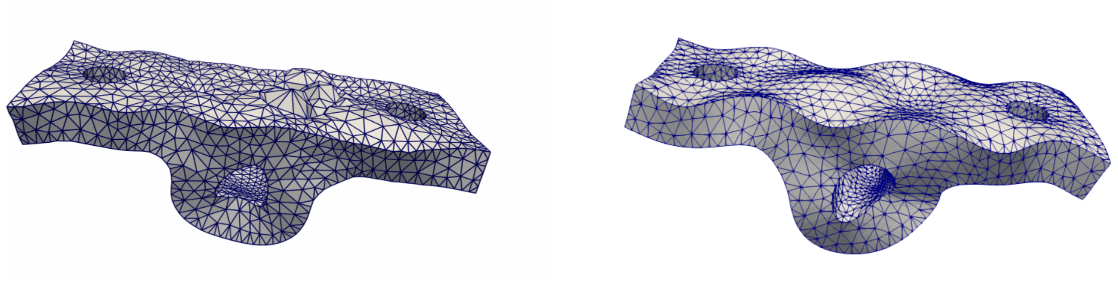

(c) UT4s

(d) T10

Figure 5.44: Axle Bracket (Tetrahedral mesh) - Mode 69

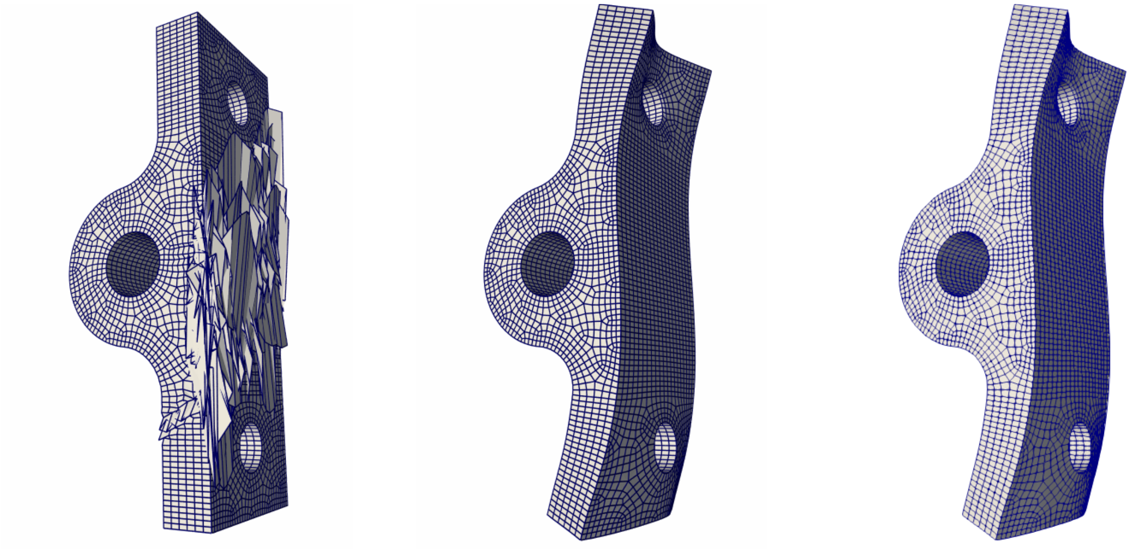
(a) NICE-H8 (b) ESNICE-H8 (c) H20

Figure 5.45: Axle Bracket (Hexahedral mesh) - Mode 10

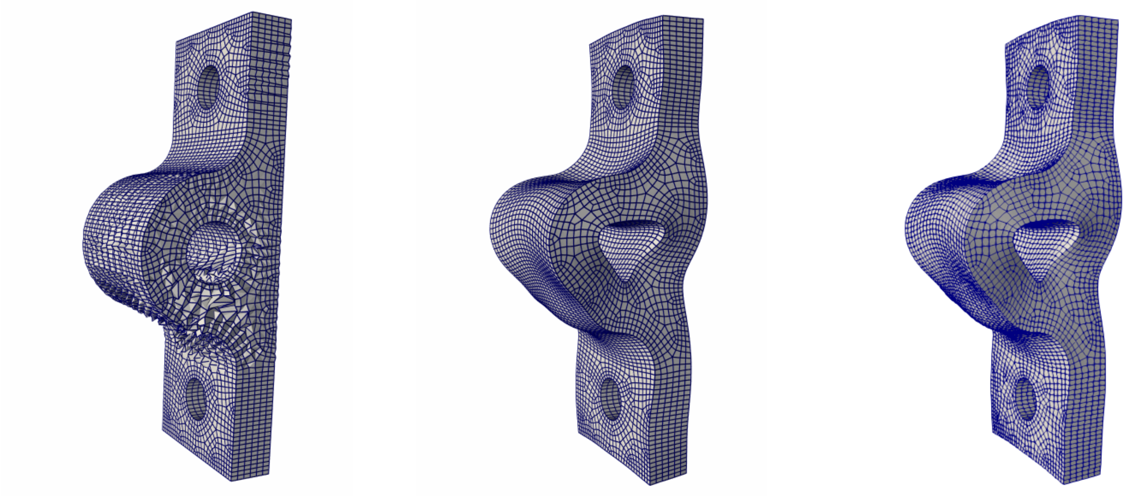
(a) NICE-H8 (b) ESNICE-H8 (c) H20

Figure 5.46: Axle Bracket (Hexahedral mesh) - Mode 50

cited paper. The number of pressure modes n_{pm} in the formulation is computed using

$$n_{pm} = k - (n_f - n_p + 1) \tag{5.20}$$

where n_f is the number of unconstrained displacements, n_p is the number of pressure degrees of freedom/integration points used in the formulation, and k is the index of the first positive eigenvalue of the eigenproblem

$$\boldsymbol{G}_h \phi_h = \lambda \boldsymbol{S}_h \phi_h \tag{5.21}$$

where $\boldsymbol{G}_h$ and $\boldsymbol{S}_h$ are computed using shape functions and their gradients [64]. These matrices do not include the stabilization material properties, however.

Here we subject the energy-sampling stabilized NICE formulation to a variant of the infsup test as described by Ko and Bathe [1]. The advantage of this alternative is that the material properties are part of the test, and, importantly, so is the stabilization. Therefore we strive to show that the stabilization still allows the formulation to be locking-free.

The goal is to show

$$\inf_{\boldsymbol{w}_h} \sup_{\boldsymbol{v}_h} \frac{\boldsymbol{w}_h^T \boldsymbol{K} \boldsymbol{v}_h}{\|\boldsymbol{w}_h\| \, \|\boldsymbol{v}_h\|} \geq \gamma_h \tag{5.22}$$

where γ_h is a constant independent of the element size, $\boldsymbol{w}_h$ and $\boldsymbol{v}_h$ belong to the solution space. Here, $\boldsymbol{K}$ is the stiffness matrix, which in the case of ESNICE includes the stabilization.

To evaluate (5.22) we solve the eigenvalue problem [1]

$$\boldsymbol{K} \phi_h = \lambda \boldsymbol{S} \phi_h \tag{5.23}$$

The matrix $\boldsymbol{S}$ is introduced to enable evaluation of the norm $\|\boldsymbol{v}_h\|^2 = \boldsymbol{v}_h^T \boldsymbol{S} \boldsymbol{v}_h$. The infsup constant follows as $\gamma_h = \sqrt{\lambda_1}$, where $\lambda_1 > 0$ is the smallest eigenvalue of (Equation 5.23).

In Figure 5.47 we show the performance of the ESNICE based on the four node tetrahedron, for a structured and an unstructured mesh of the same geometry as that described in Reference [51]. The Poisson ratio varies from 0.3 to 0.499999 to test the effect of near incompressibility. Importantly, the amount of stabilization is varied as well: The parameter b of (Equation 5.8) is artificially modified by four orders of magnitude to mb, where $m = 0.01, 1.0, 100.0$. Figure 5.47

demonstrates the nearly negligible influence of the stabilization on the locking-free response. In fact, the mechanically derived amount of stabilization with b given as below (Equation 5.8) produces neat convergence to a nonzero γ_h, whereas more ($m = 100.0$) or less ($m = 0.01$) stabilization has a bit more pronounced effect (although still indicating locking-free response).

By way of contrast, Figure 5.48 shows the results of the infsup test of [1] for the standard isoparametric four-node tetrahedron. The strong dependence on the Poisson's ratio as it approaches 0.5 indicates the strong volumetric locking of the standard tetrahedron.

5.6 Pressures in nearly-incompressible simulations

We consider a unit cube made of nearly incompressible material with Young's Modulus of 1 Pa and density of 1 kg/m^3, as originally used in [57], but the Poisson's ratio is taken as $\nu = 0.499999$ to approach nearly incompressible response. Of interest is the representation of the mechanical pressure. The NICE formulation (and hence the ESNICE formulation) cannot guarantee the absence of all pressure oscillations (as explained in the previous section).

The five sides of the cube are in frictionless contact with a rigid die, and only the top surface is free. It is known that the presence of such boundaries tends to amplify the potential for pressure oscillations to appear.

Figure 5.49 presents the mechanical pressure computed with an unstructured mesh of tetrahedra, with 15 element edges per side of the cube. The nodal pressures are linearly interpolated in between the nodes. Furthermore, we also present the mechanical pressures element-wise, i.e. uniform across each element, where the elemental pressures are obtained by averaging the pressures at the nodes. The nodal values of pressure do indeed show a tendency for oscillation. The element-wise pressures are a smoothed version of the nodal pressures, and hence better behaved. Note that these pressures are obtained by pure post-processing operation, all based on the computed vibration modes. Lamichhane [65] proposed to enrich the displacement

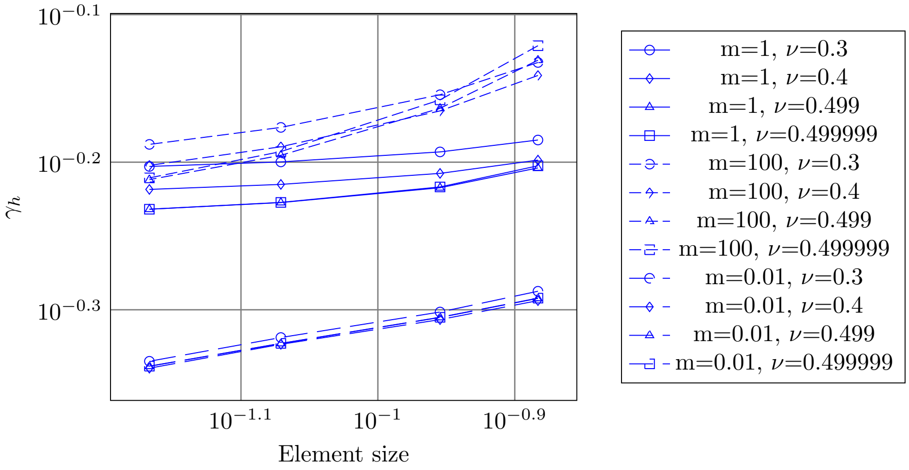

(a) Unstructured mesh

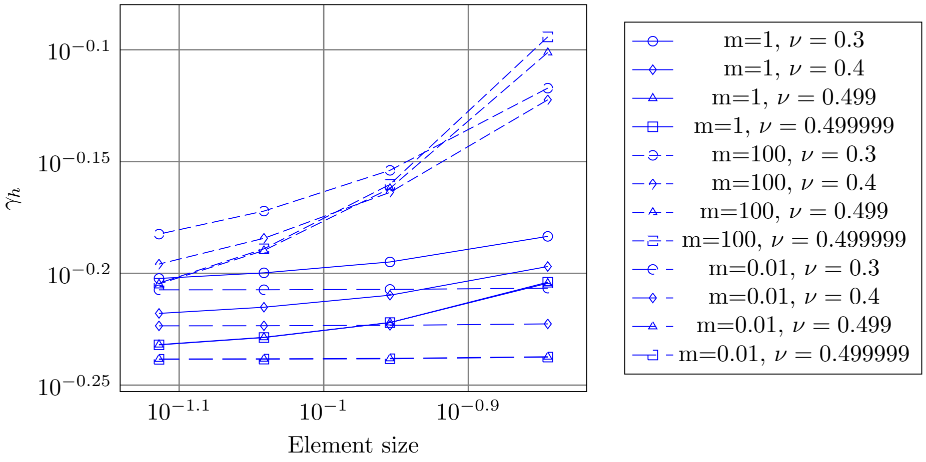

(b) Structured mesh

Figure 5.47: The infsup test of [1]. ESNICE four-node tetrahedron. The amount of stabilization is varied by two orders of magnitude up or down. Note the strongly compressed vertical axis: The small variation of the γ_h indicates the test is passed.

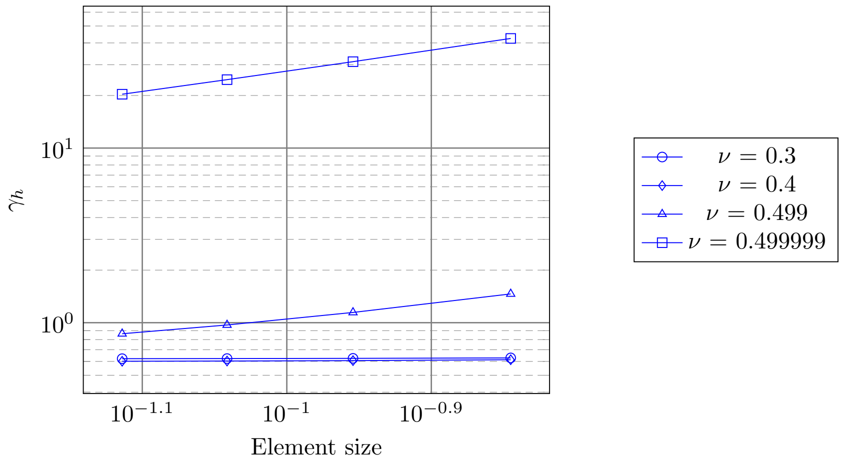

Figure 5.48: The infsup test of [1]. Isoparametric four-node tetrahedron (Structured Mesh). The large variation of the γ_h along the vertical axis indicates the test is *not* passed.

space with bubble basis function in nodally integrated formulations to achieve inf-sup stability. Ortiz-Bernardin et al [66] demonstrate that such enrichment of displacement space can help in eliminating pressure oscillations in volume-averaged nodal projection-based formulations.

These proposed improvements are certainly of interest, but we haven't addressed them in the context of the present work.

The ESNICE elements are implemented in an opensource Julia project called FineTools, and can be found at https://github.com/PetrKryslUCSD/FinEtools.jl.git.

Chapter 5 has many details taken from the manuscript, "Sivapuram R, Krysl P. On the Energy-Sampling Stabilization of Nodally Integrated Continuum Elements for Dynamic Analyses. *Finite Elements in Analysis and Design* 2019; **167**:103322, doi:10.1016/j.finel.2019.103322.", and the work is done in collaboration with Prof. Petr Krysl. The dissertation author is the primary investigator of the manuscript.

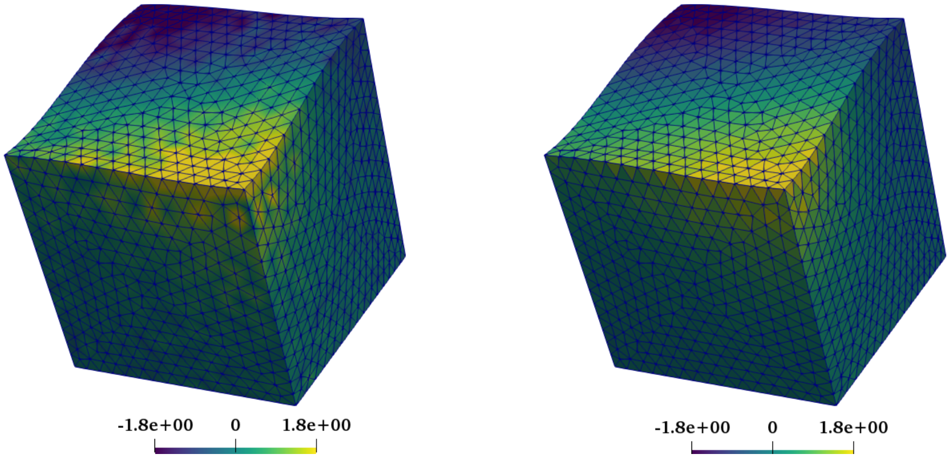

(a) Mode 1, Nodal Pressures (b) Mode 1, Element-wise Pressures

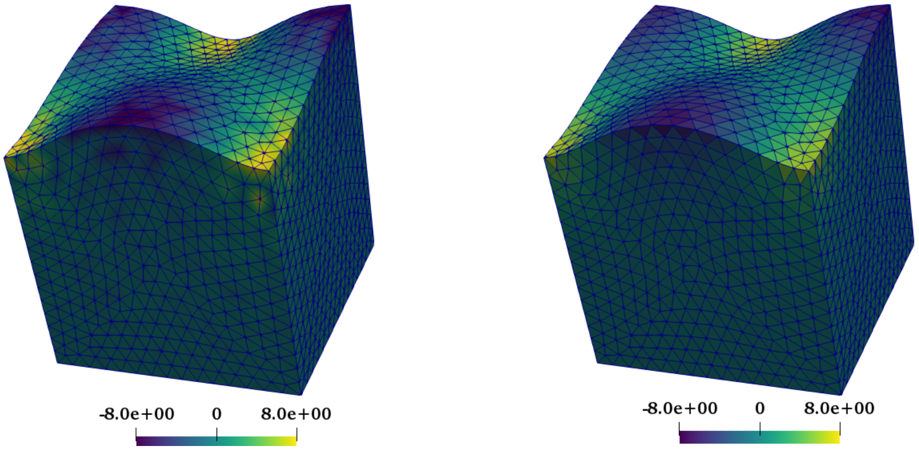

(c) Mode 11, Nodal Pressures (d) Mode 11, Element-wise Pressures

Figure 5.49: Confined block of nearly-incompressible material. Unstructured tetrahedral mesh with 15 element edges per side. Mechanical pressure is displayed, either as nodal values interpolated linearly in between, or values calculated by averaging the nodal values and displaying them as uniform element-wise.

Chapter 6

Conclusions

This thesis shows the development of a novel stress field for the stabilized mean-strain formulation which converges at an optimal rate. The mean-strain hexahedral and tetrahedral elements introduced by [23, 22, 24] are capable of handling constrained materials (e.g. nearly incompressible) and of performing well for thin, shell-like structures. These elements use suppression of hourglass modes based on the notion of stabilization energy sampled with two different quadrature rules.

One possible weakness of these mean-strain elements is the fact that each element only represents uniform stress. Hence the recovery of the nodal stresses is slightly more challenging. In this work, a method is proposed for the computation of the stresses for the mean-strain hexahedral and tetrahedral elements. The variational formulation of the mean-strain method is shown to result in an expression that mixes together the stresses in the real material with the stresses in the stabilization material. These mixed stresses are used as a basis for extrapolation of the stress to the nodes of the element. This information may subsequently be averaged at the nodes to produce continuous stress fields as usual in the post-processing of finite element results.

We compare the proposed method with direct computation of stresses at the nodes (such as for the improved-stress Abaqus elements), and with recovery of the stresses based on the mean stresses only (for the mean-strain elements as described in [23, 22, 24] and for the reduced-integration elements in Abaqus). We investigate the following benchmarks: stree-free hole in an infinite slab, thick plate under pressure (NAFEMS LE10), elliptic membrane (NAFEMS LE1), thin cantilever beam, and a fibrous-composite cube under general quadratic displacements. We show that the improved procedure for the recovery of nodal stresses (which we call trend-based here) is superior to the recovery based on the mean stress only: in all our examples the trend-based recovery was at least as good as the mean-stress-only recovery, and often significantly better. Importantly, the trend-based recovery for the quadratic mean-strain tetrahedron was able to realize (at least in some examples) the theoretical quadratic convergence rate (compared to linear for the mean-stress only recovery).

As noted earlier, this work investigates the stresses only in linear elasticity problems. Since the trend-based stress field is derived without any reference to the material law, we believe it is equally applicable in the nonlinear regime. This may be a topic for a future investigation.

We propose a stabilization for nodally integrated finite elements based on energy-sampling to address the drawback that these formulations yield spurious modes in eigenvalue problems such as in free vibration and buckling analysis.

The stabilization methods that have been proposed so far in the literature used a stabilization factor which needed to be chosen by trial-and-error and was uniformly used for all the finite elements in the mesh. In this work we eliminate both the need for user input and also make the stabilization tailored to the mesh.

We also develop a stabilization procedure for Nodally Integrated Continuum Elements (NICE) for dynamic analyses. We add two energy terms for stabilization: first to ensure full rank of the stiffness matrix through elementwise quadrature with a “full integration” rule and the second using nodal integration. These two terms mutually cancel when the mesh experiences uniform strains, and thereby ensure consistency of the scheme.

The stabilization energy is generated by employing an artificial “stabilization” material model. The stabilization material is constructed as compressible to avoid volumetric locking and also includes a shape-related stabilization factor. The stabilization factor is designed so as to soften the fully integrated stabilization material-based stiffness matrix to minimize shear locking and thereby improving the bending response. Elements with very bad aspect ratio typically exhibit a high amount of shear locking, and in those cases the corresponding stabilization factor is very small.

This work we address the stabilization for nodally-integrated schemes for linear tetrahedral and hexahedral elements. For tetrahedral elements, we use a fitting of the data obtained from numerical simulations of a rectangular beam (meshed using 6 tetrahedral elements) where the data is the aspect ratios of the finite elements and the ratios of the finite element-based and exact strain energies of the beam. The stabilization factor of a finite element is computed using the obtained data fit, and is optimal with respect to the collected data. The stabilization factor of hexahedral elements was analytically derived in [47, 30] and is based on the ratio of finite element-based and exact strain energies of a rectangular beam.

Several examples of free vibration analysis are presented to demonstrate the effectiveness of the proposed stabilization. The examples show convergence studies, frequency spectrum comparisons and qualitative comparison of mode shapes at both lower and higher ends of the spectrum. We demonstrate using different amounts of stabilization for the aluminum cylinder example that choosing appropriate amount of stabilization is nontrivial and that under-stabilization causes spurious modes whilst over-stabilization yields stiff modes due to the reintroduction of shear locking.

We show for some well-shaped elements that the stabilization factor chosen by energy-sampling technique satisfies the derived bounds which guarantees the elimination of spurious free vibration modes. We show on examples that the eigenmodes obtained using energy-sampling stabilization (ESNICE formulation) are physical even at higher end of the frequency spectrum unlike those obtained using methods proposed in the literature (we used UT4s [57] for comparison). The examples demonstrate that the energy sampling-based stabilization factor adds just sufficient stability to prevent unphysical modes whilst maintaining good performance. The hexahedral elements are observed to exhibit more spuriousness than the tetrahedral elements because the former use bilinear strains unlike the latter which use constant strains. The passing of the inf-sup test proposed by [1] demonstrates that the ESNICE formulation is coercive and locking-free. Developing a stabilization procedure for nodally integrated plate elements and eliminating pressure oscillations is an interesting future work.

Chapter 7

Original Contributions

This chapter describes in brief my contributions to literature made under the guidance of Prof. Krysl. The works broadly include developing a optimally convergent and improved stress field for stabilized mean-strain finite elements, energy-sampling stabilization for nodally integrated formulations in the context of dynamic analyses, and a Model-Order Reduction (MOR) procedure for rapid estimation of eigenvalues for 3D continua.

7.1 Improved Recovered Nodal Stress for Mean-Strain Finite Elements

This publication develops an improved stress field for stabilized mean-strain finite elements. The trilinear hexahedral elements undergo volumetric locking for nearly-incompressible problems. The quadratic tetrahedral elements yield displacement fields, devoid of volumetric locking, yet the stress fields are noisy. The stabilized mean-strain formulation is devoid of volumetric locking and yields an improved bending response. The mean stresses are noise-free even for nearly-incompressible problems. However, because of averaging the stresses element-wise, the quality of stress estimates is lower and the stress convergence is suboptimal, e.g. the mean stresses converge linearly for QT10MS elements. This work uses additional terms based on stabilization material in the stress field which improves the quality of stress estimates over the mean stresses. In order to obtain a nodal stress field, we use extrapolation of the stresses from the integration points of the finite element to the node. The stress at each node is obtained by averaging the extrapolated stresses from the integration points of the neighboring finite elements. Such an extrapolation helps in better stress estimation in curved elements, e.g. quadratic tetrahedral elements. We demonstrate through examples that the QT10MS stresses converge at optimal rate, i.e., 2 as compared to the linear order of the mean stresses. The examples demonstrate the optimal convergence of stresses and that the stresses are noise-free even in the presence of near-incompressibility. Examples also include the use of orthotropic materials and a sandwich composite (Meyer-Piening Plate). This work can be straightforwardly extended to nonlinear regime, since the stress field is derived independent of the material law. The results are published in the journal paper [30],

Sivapuram R, Krysl P. Improved Recovered Nodal Stress for Mean-Strain Finite Elements. *Finite Elements in Analysis and Design* 2018; **146**:70-83, doi:10.1016/j.finel.2018.04.005.

7.2 On the Energy – Sampling Stabilization of Nodally Integrated Continuum Elements for Dynamic Analyses

The Nodally Integrated Continuum Elements (NICE) are locking-free and give great displacement fields in static analyses [51]. This is extremely beneficial in the case of triangles/tetrahedra which do not have a reduced integration rule or a B-bar method for avoiding locking. The NICE formulation is also insensitive to distorted elements and slivers, needles, wedges, etc in a mesh [53]. However, the NICE formulation lacks coercivity which leads to spuriousness in dynamic analyses, e.g. free vibration, buckling, etc. Stabilization is required to add some coercivity to the formulation, and this work uses Energy-Sampling Stabilization to achieve that. This work considers linear tetrahedral and hexahedral elements for demonstration.

The stabilization procedures proposed in literature [57] use a fixed amount of stabilization based on numerical experience and a full integration term. We show that such a fixed value cannot be extended to all the problems, e.g. plate-like structures, and to higher eigen modes. A fixed value of stabilization can lead to

1. Overstabilization - This means more contribution to strain energy from the fully integrated term, which engenders shear locking.
2. Understabilization - This means less stabilization than required, which makes the formulation yield spurious higher eigenmodes.

We derive bounds which are required to be satisfied to sufficiently stabilize all the eigenmodes of a problem, whilst maintaining positive definiteness. The stabilization employed in this work uses aspect-ratio of the finite elements to define the stabilization amount with no user-interaction required. The aspect-ratio based stabilization is aimed at representing the bending response of linear finite elements more accurately. For tetrahedral elements, we use a least square fit to determine some parameters required for automatic stabilization where the data is collected from several numerical bending tests of beams meshed with six tetrahedral elements. For hexahedral elements, an aspect-ratio stabilization can be derived using a numerical bending test [47]. We also showed by means of hand calculations that the stabilization obtained using the element aspect ratios satisfy the mathematical bounds. Several examples for free vibration analyses are shown to demonstrate that the modes obtained using ESNICE formulation are devoid of spuriousness both at the low and high ends of the eigen spectrum unlike the NICE and UT4s [57] formulations. However, the ESNICE formulation possesses spurious pressure modes which lead to pressure oscillations and an example is shown for the same. The ESNICE formulation satisfies an inf-sup test [1] verifying that the formulation is locking-free. The results are published in the journal paper [59],

Sivapuram R, Krysl P. On the Energy-Sampling Stabilization of Nodally Integrated Continuum

Elements for Dynamic Analyses. *Finite Elements in Analysis and Design* 2019; **167**:103322, doi:10.1016/j.finel.2019.103322

7.3 Rapid Free – Vibration Analysis with Model Reduction based on Coherent Nodal Clusters

This work proposes a novel Model-Order Reduction (MOR) technique based on Reduced Bases (RB) approach for approximating the response of structures with many degrees of freedom in the context of free vibration analyses. The method takes advantage of the spatial coherence of the displacement degrees of freedom in a local region and a heuristic set of basis functions to compute the reduced bases. A graph partitioning algorithm (here, Recursive Intertial Bisection (RIB)) is employed to divide the structural nodes into several clusters based on their mutual Eulerian distances. Each of the nodal clusters is called a Coherent Nodal Cluster, and we assume the spatial coherence of displacements in the cluster. A set of polynomial basis functions are constructed for each cluster for model reduction, i.e. we assume the displacements of nodes in each cluster to be parametrized by a set of polynomial functions (of some chosen order). In this work, we use Legendre polynomials for this purpose because the transformation matrix constructed using the Legendre polynomial-based basis vectors have a better condition number. The transformation matrix is constructed by assembling the cluster-based transformation matrices so that basis vectors corresponding to different clusters are linearly independent, and in fact, orthogonal. The basis vectors corresponding to each cluster are already linearly independent, owing to the use of Legendre polynomials. However, the order of polynomial used should be chosen such that it does not overfit the number of nodes, i.e., polynomial order is selected subject to cluster size. The transformation matrix is thus very cheap to compute as compared to most MOR techniques in literature which use Singular Value Decomposition (SVD), LU factorization, solving Lyapunov equations, etc. The parameters that need to be selected are the number of nodal clusters and the polynomial orders used. In this work, we use an isotropic basis in all the coordinate directions and a uniform polynomial order across all the clusters. We provide guidelines based on shear wave velocity in a material medium to choose the number of nodal clusters and the polynomial order. We show by means of examples how the proposed MOR technique helps in rapid eigenvalue estimation, especially when one needs many eigenvalues for large (in terms of degrees of freedom) structures. To guarantee convergence, we use an adaptive procedure where we slowly increase the polynomial order used in the nodal clusters until change in eigenvalues between consecutive polynomial-order refinements reach a user-specified tolerance. The examples demonstrate good speedups and controllable accuracy of the estimated eigenvalues. The results are published in a journal paper [67],

Krysl P, Sivapuram R, Abawi AA. Rapid free-vibration analysis with model reduction based on coherent nodal clusters. *International Journal for Numerical Methods in Engineering* 2020; **Accepted**.

Chapter 8

Potential Future Work

1. The proposed stress field developed for mean-strain formulations can be extended to nonlinear applications to obtain improved and convergent nodal stress estimates.

2. The energy-sampling stabilization for assumed-strain formulations is explored for linear statics, dynamics and nonlinear applications, However, the stabilization of assumed-strain elements in plasticity applications is nontrivial. It would be interesting to develop a stabilization material for plasticity problems.

3. The nodally integrated formulations yield pressure oscillations in nearly-incompressible media. One way to avoid them is to use additional internal degrees of freedom [66]. Developing a formulation without spurious pressure modes by providing additional stabilization to the formulation would be an interesting future work. The extension of the ESNICE formulation [59] to nonlinear applications and buckling problems, and developing stabilization for higher-order nodally integrated formulations are some possible future works.

4. The Coherent Nodal Clusters-based Model Order Reduction procedure can be extended for the approximation of Frequency Response Function in Steady State Dynamics structural problems.

References

[1] Ko Y, Bathe KJ. Inf-sup testing of some three-dimensional low-order finite elements for the analysis of solids. *Computers & Structures* 2018; **209**:1–13, doi:https://doi.org/10.1016/j.compstruc.2018.07.006.

[2] Schöberl J. Netgen an advancing front 2d/3d-mesh generator based on abstract rules. *Computing and Visualization in Science* Jul 1997; **1**(1):41–52, doi:10.1007/s007910050004.

[3] Choi WY, Kwak DY, Son IH, Im YT. Tetrahedral mesh generation based on advancing front technique and optimization scheme. *International Journal for Numerical Methods in Engineering* 2003; **58**(12):1857–1872, doi:10.1002/nme.840.

[4] Ito Y, Shih AM, Soni BK. Reliable isotropic tetrahedral mesh generation based on an advancing front method. *In Proceedings 13th International Meshing Roundtable, Williamsburg, VA, Sandia National Laboratories*, 2004; 95–105.

[5] Labelle F, Shewchuk JR. Isosurface stuffing: Fast tetrahedral meshes with good dihedral angles 2007.

[6] Bronson J, Levine JA, Whitaker R. Lattice cleaving: A multimaterial tetrahedral meshing algorithm with guarantees 2014.

[7] Yu Z, Wang J, Gao Z, Xu M, Hoshijima M. New software developments for quality mesh generation and optimization from biomedical imaging data. *Computer Methods and Programs in Biomedicine* 2014; **113**(1):226 – 240, doi:https://doi.org/10.1016/j.cmpb.2013.08.009.

[8] Cheng SW, Dey TK, Shewchuk JR. *Delaunay Mesh Generation*. CRC Press, 2012.

[9] Schneiders R. Algorithms for quadrilateral and hexahedral mesh generation 1999.

[10] Owen SJ. A survey of unstructured mesh generation technology. *INTERNATIONAL MESHING ROUNDTABLE*, 1998; 239–267.

[11] Bern M, Plassmann P. *Mesh Generation*. Elsevier Science, 2000.

[12] Frey PJ, George PL. *Mesh Generation: Application to Finite Elements*. Hermes Science, 2001.

[13] Edelsbrunner H. *Geometry and Mesh Generation*. Cambridge University Press, 2001.

[14] Hughes TJR. *The finite element method. Linear static and dynamic finite element analysis*. Dover publications, New York, 2000.

[15] Reddy JN. *Introduction to Finite Element Method*. McGraw-Hill Education, 2005.

[16] Zienkiewicz OC, Taylor RL. *The Finite Element Method*. Butterworth-Heinemann, 2000.

[17] Bathe KJ. *Finite Element Procedures*. Prentice Hall, Pearson Education Inc, 2016.

[18] Hughes TJR. Generalization of selective integration procedures to anisotropic and nonlinear media. *International Journal for Numerical Methods in Engineering* 1980; **15**(9):1413–1418, doi:10.1002/nme.1620150914.

[19] Prathap G, Bhashyam GR. Reduced integration and the shear-flexible beam element. *International Journal for Numerical Methods in Engineering* 1982; **18**(2):195–210, doi: 10.1002/nme.1620180205.

[20] Krysl P. Mean-strain eight-node hexahedron with stabilization by energy sampling. *International Journal for Numerical Methods in Engineering* 2015; **102**(3-4):437–449, doi: 10.1002/nme.4721.

[21] Pakravan A, Krysl P. Mean-strain 10-node tetrahedron with energy-sampling stabilization. *International Journal for Numerical Methods in Engineering* 2017; **109**(10):1439–1460, doi:10.1002/nme.5335.

[22] Krysl P. Mean-strain eight-node hexahedron with stabilization by energy sampling. *International Journal for Numerical Methods in Engineering* 2014; **102**(3-4):437–449, doi: 10.1002/nme.4721.

[23] Krysl P. Mean-strain eight-node hexahedron with optimized energy-sampling stabilization. *Finite Elements in Analysis and Design* 2016; **108**:41–53, doi:10.1016/j.finel.2015.09.008.

[24] Nguyen P, Doskàr M, Pakravan A, Krysl P. Modification of the quadratic 10-node tetrahedron for thin structures and stiff materials under large-strain hyperelastic deformation. *International Journal for Numerical Methods in Engineering* 2018; **114**(6):619–636, doi: 10.1002/nme.5757.

[25] Felippa CA. On the original publication of the general canonical functional of linear elasticity. *Journal of Applied Mechanics* 2001; **67**(1):217–219, doi:10.1115/1.321170.

[26] Belytschko T, Bindeman LP. Assumed strain stabilization of the 8 node hexahedral element. *Computer Methods in Applied Mechanics and Engineering* 1993; **105**(2):225–260.

[27] Flanagan DP, Belytschko T. A uniform strain hexahedron and quadrilateral with orthogonal hourglass control. *International Journal for Numerical Methods in Engineering* 1981; **17**(5):679–706.

[28] Wriggers P. Mixed finite element methods - theory and discretization. *Mixed Finite Element Technlogies* 2009; **509**:131–177, doi:10.1002/nme.1620310311.

[29] Pakravan A, Krysl P. Mean-strain 10-node tetrahedron with energy-sampling stabilization for nonlinear deformation. *International Journal for Numerical Methods in Engineering* 2017; **111**(7):603–623, doi:10.1002/nme.5473.

[30] Sivapuram R, Krysl P. Improved recovered nodal stress for mean-strain finite elements. *Finite Elements in Analysis and Design* 2018; **146**:70 – 83, doi:10.1016/j.finel.2018.04.005.

[31] Krysl P. Mean-strain eight-node hexahedron with optimized energy-sampling stabilization for large-strain deformation. *International Journal for Numerical Methods in Engineering* 2015; **103**(9):650–670, doi:10.1002/nme.4907.

[32] Pakravan A, Krysl P. Mean-strain 10ÿnode tetrahedron with energy-sampling stabilization. *International Journal for Numerical Methods in Engineering* 2017; **109**:1439–1460.

[33] Pakravan P, Krysl P. Mean-strain 10-node tetrahedron with energy-sampling stabilization for nonlinear deformation. *International Journal for Numerical Methods in Engineering* 2017; doi:10.1002/nme.5473.

[34] Dassault Systèmes, Providence, RI, USA.. *ABAQUS Documentation* 2016.

[35] Zienkiewicz O, Zhu J. The superconvergent patch recovery (spr) and adaptive finite element refinement. *Computer Methods in Applied Mechanics and Engineering* 1992; **101**(1):207–224, doi:http://dx.doi.org/10.1016/0045-7825(92)90023-D.

[36] Payen DJ, Bathe KJ. Improved stresses for the 4-node tetrahedral element. *Computers & Structures* 2011; **89**(13):1265 – 1273, doi:http://dx.doi.org/10.1016/j.compstruc.2011.02.009.

[37] Payen DJ, Bathe KJ. The use of nodal point forces to improve element stresses. *Computers & Structures* 2011; **89**(5):485 – 495, doi:http://dx.doi.org/10.1016/j.compstruc.2010.12.002.

[38] Payen DJ, Bathe KJ. A stress improvement procedure. *Computers & Structures* 2012; **112-113**:311–326, doi:http://dx.doi.org/10.1016/j.compstruc.2012.07.006.

[39] National Agency for Finite Element Methods and Standards, U.K.. *The Standard NAFEMS Benchmarks*. Revision 3 edn. October 1990.

[40] Dassault Systemés Simulia Corp.. *Abaqus Benchmarks Manual*. 6.12 edn. 2012.

[41] Sadd MH. Chapter 8 - two-dimensional problem solution. *Elasticity (Third Edition)*, Sadd MH (ed.). Third edition edn., Academic Press: Boston, 2014; 159 – 234, doi:https://doi.org/10.1016/B978-0-12-408136-9.00008-8.

[42] Dassault Systemés Simulia Corp.. *ABAQUS/CAE User's Guide*. 6.14 edn. 2014.

[43] Meyer-Piening HR. Analysis of the elasticity solution to linear sandwich beam, plate and shell analyses. *Journal of Sandwich Structures and Materials* 2004; **6**:295–12, doi: http://dx.doi.org/10.1177/1099636204035395.

[44] Vidal P, Polit O, D'Ottavio M, Valot E. Assessment of the refined sinus plate finite element: Free edge effect and meyer-piening sandwich test. *Finite Elements in Analysis and Design* 2014; **92**:60–71, doi:https://doi.org/10.1016/j.finel.2014.08.004.

[45] de Souza Neto E, Perić D, Dutko M, Owen D. Design of simple low order finite elements for large strain analysis of nearly incompressible solids. *International Journal of Solids and Structures* 1996; **33**(20):3277 – 3296, doi:10.1016/0020-7683(95)00259-6.

[46] Simo JC, Rifai MS. A class of mixed assumed strain methods and the method of incompatible modes. *International Journal for Numerical Methods in Engineering* 1990; **29**(8):1595–1638, doi:10.1002/nme.1620290802.

[47] Krysl P. Mean-strain 8-node hexahedron with optimized energy-sampling stabilization. *Finite Elements in Analysis and Design* 2016; **108**:41 – 53, doi:10.1016/j.finel.2015.09.008.

[48] Krysl P. Mean-strain eight-node hexahedron with optimized energy-sampling stabilization for large-strain deformation. *International Journal for Numerical Methods in Engineering* 2015; **103**(9):650–670, doi:10.1002/nme.4907.

[49] Dohrmann C, Heinstein MW, Jung J, Key SW, Witkowski WR. Node-based uniform strain elements for three-node triangular and four-node tetrahedral meshes. *International Journal for Numerical Methods in Engineering* 2000; **47**(9):1549–1568, doi: 10.1002/(SICI)1097-0207(20000330)47:9⟨1549::AID-NME842⟩3.0.CO;2-K.

[50] Bonet J, Marriott H, Hassan O. An averaged nodal deformation gradient linear tetrahedral element for large strain explicit dynamic applications. *Communications in Numerical Methods in Engineering* 2001; **17**(8):551–561, doi:10.1002/cnm.429.

[51] Krysl P, Zhu B. Locking-free continuum displacement finite elements with nodal integration. *International Journal for Numerical Methods in Engineering* 2008; **76**(7):1020–1043, doi: 10.1002/nme.2354.

[52] Castellazzi G, Krysl P. Displacement-based finite elements with nodal integration for reissner–mindlin plates. *International Journal for Numerical Methods in Engineering* 2009; **80**(2):135–162, doi:10.1002/nme.2622.

[53] Krysl P, Kagey H. Reformulation of nodally integrated continuum elements to attain insensitivity to distortion. *International Journal for Numerical Methods in Engineering* 2012; **90**(7):805–818, doi:10.1002/nme.3342.

[54] Castellazzi G, Krysl P. A nine-node displacement-based finite element for reissner–mindlin plates based on an improved formulation of the nipe approach. *Finite Elements in Analysis and Design* 2012; **58**:31 – 43, doi:10.1016/j.finel.2012.04.004.

[55] Castellazzi G, Gentilini C, Krysl P, Elishakoff I. Static analysis of functionally graded plates using a nodal integrated finite element approach. *Composite Structures* 2013; **103**:197 – 200, doi:10.1016/j.compstruct.2013.04.013.

[56] Artioli E, Castellazzi G, Krysl P. Assumed strain nodally integrated hexahedral finite element formulation for elastoplastic applications. *International Journal for Numerical Methods in Engineering* 2014; **99**(11):844–866, doi:10.1002/nme.4723.

[57] Puso MA, Solberg J. A stabilized nodally integrated tetrahedral. *International Journal for Numerical Methods in Engineering* 2006; **67**(6):841–867, doi:10.1002/nme.1651.

[58] Broccardo M, Micheloni M, Krysl P. Assumed-deformation gradient finite elements with nodal integration for nearly incompressible large deformation analysis. *International Journal for Numerical Methods in Engineering* 2009; **78**(9):1113–1134, doi:10.1002/nme.2521.

[59] Sivapuram R, Krysl P. On the energy-sampling stabilization of nodally integrated continuum elements for dynamic analyses. *Finite Elements in Analysis and Design* 2019; **167**:103 322, doi:https://doi.org/10.1016/j.finel.2019.103322.

[60] Gee MW, Dohrmann CR, Key SW, Wall WA. A uniform nodal strain tetrahedron with isochoric stabilization. *International Journal for Numerical Methods in Engineering* 2008; **78**(4):429–443, doi:10.1002/nme.2493.

[61] Hillman M, Chen JS. An accelerated, convergent, and stable nodal integration in galerkin meshfree methods for linear and nonlinear mechanics. *International Journal for Numerical Methods in Engineering* 2016; **107**(7):603–630, doi:10.1002/nme.5183.

[62] Wu CT, Chi SW, Koishi M, Wu Y. Strain gradient stabilization with dual stress points for the meshfree nodal integration method in inelastic analyses. *International Journal for Numerical Methods in Engineering* 2016; **107**(1):3–30, doi:10.1002/nme.5147.

[63] National Agency for Finite Element Methods and Standards, U.K.. *Test FV12, The Standard NAFEMS Benchmarks*. Revision 3 edn. October 1990.

[64] Chapelle D, Bathe KJ. The inf-sup test. *Computers & Structures* 1993; **47**(4-5):537–545, doi:10.1016/0045-7949(93)90340-j.

[65] Lamichhane BP. From the hu—washizu formulation to the average nodal strain formulation. *Computer Methods in Applied Mechanics and Engineering* 2009; **198**(49):3957 – 3961, doi:https://doi.org/10.1016/j.cma.2009.09.008.

[66] Ortiz-Bernardin A, Hale J, Cyron C. Volume-averaged nodal projection method for nearly-incompressible elasticity using meshfree and bubble basis functions. *Computer Methods in Applied Mechanics and Engineering* 2015; **285**:427 – 451, doi:https://doi.org/10.1016/j.cma.2014.11.018.

[67] Krysl P, Sivapuram R, Abawi AA. Rapid free-vibration analysis with model reduction based on coherent nodal clusters. *International Journal for Numerical Methods in Engineering* 2020; **Accepted**.